



**HAL**  
open science

# HVPE-Grown GaAs Nanowires: Growth Modeling, Passivation and Transport Properties

Hadi Hijazi

► **To cite this version:**

Hadi Hijazi. HVPE-Grown GaAs Nanowires: Growth Modeling, Passivation and Transport Properties. Micro and nanotechnologies/Microelectronics. Université Clermont Auvergne [2017-2020], 2019. English. NNT: 2019CLFAC059 . tel-02515900

**HAL Id: tel-02515900**

**<https://theses.hal.science/tel-02515900v1>**

Submitted on 23 Mar 2020

**HAL** is a multi-disciplinary open access archive for the deposit and dissemination of scientific research documents, whether they are published or not. The documents may come from teaching and research institutions in France or abroad, or from public or private research centers.

L'archive ouverte pluridisciplinaire **HAL**, est destinée au dépôt et à la diffusion de documents scientifiques de niveau recherche, publiés ou non, émanant des établissements d'enseignement et de recherche français ou étrangers, des laboratoires publics ou privés.

**UNIVERSITE CLERMONT AUVERGNE**

**ECOLE DOCTORALE DES SCIENCES FONDAMENTALES**

**THESIS**

By

**Hadi HIJAZI**

To obtain the grade of

**Doctorate of University**

*Specialty: Dense Environments and Materials*

**HVPE-Grown GaAs Nanowires: Growth Modeling,  
Passivation and Transport Properties.**

Public oral defense on October 25, 2019, with the following commission

Frank Glas	Research Director, C2N, France	Reporting judge
Jonas Johansson	Associate Professor, Lund University, Sweden	Reporting judge
Vladimir G. Dubrovskii	Professor, ITMO University, Russia	Examiner
Daniel Paget	Research Director, Ecole Polytechnique, France	Examiner
Frédéric Leroy	Professor, CiNaM, France	Examiner (president)
Yamina André	Assistant Professor, HDR, Institut Pascal, France	Thesis director
Christine Robert-Goumet	Assistant Professor, HDR, Institut Pascal, France	Thesis director
Guillaume Monier	Research Engineer, HDR, Institut Pascal, France	Supervisor
Evelyne Gil	Professor, Institut Pascal, France	Invited
Joel Leymarie	Professor, Institut Pascal, France	Invited
Georges Cirlin	Professor, ITMO University, Russia	Invited
Ray LaPierre	Professor, McMaster University, Canada	Invited







# Table of Contents

<b>Abstract</b>	<b>i</b>
<b>Acknowledgments</b>	<b>ii</b>
<b>Dedications</b>	<b>v</b>
<b>General introduction</b>	<b>1</b>
<b>I Surface preparation of Si(111) substrates and Gallium Arsenide nanowires growth by Hydride Vapor Phase Epitaxy (HVPE)</b>	<b>5</b>
I.1 Hydride Vapor Phase Epitaxy for GaAs Nanowires . . . . .	5
I.1.1 Introduction . . . . .	5
I.1.2 III-V semiconductor NWs . . . . .	6
I.1.3 Gallium Arsenide NWs: crystallographic properties . . . . .	7
I.1.4 Nanowires growth by different epitaxial techniques: state of the art . . . . .	9
I.1.5 HVPE experimental setup at Institut Pascal . . . . .	13
I.1.6 HVPE process: thermodynamics and kinetics of growth . . . . .	15
I.2 Surface preparation: dewetting of gold film on Si(111) substrates . . . . .	21
I.2.1 Introduction . . . . .	21
I.2.2 Effect of the SiO <sub>2</sub> film and substrate's temperature T <sub>s</sub> . . . . .	22
I.2.3 Different amounts of gold deposited . . . . .	24
I.2.4 Influence of the annealing time t <sub>a</sub> . . . . .	25
I.2.5 Dynamics of Au clusters and decomposition of SiO <sub>2</sub> . . . . .	26

I.3	Experimental results on the growth of GaAs NWs on Si(111) by HVPE . . . . .	30
I.4	Conclusion . . . . .	37
<b>II</b>	<b>Thermodynamics of GaAs nanowires growth in presence of Si</b>	<b>39</b>
II.1	Introduction . . . . .	39
II.2	Influence of Si on the nucleation rate of GaAs NWs grown on Si substrates. . . . .	40
II.2.1	Thermodynamic model . . . . .	41
II.2.2	Results and discussion . . . . .	44
II.3	Si doping of vapor-liquid-solid GaAs NWs: n-type or p-type? . . . . .	48
II.3.1	Thermodynamic model . . . . .	49
II.3.2	Results and discussions . . . . .	53
II.4	Conclusion . . . . .	58
<b>III</b>	<b>Charge and spin transport in GaAs NWs grown by HVPE</b>	<b>61</b>
III.1	Introduction . . . . .	61
III.2	Optical spin orientation in GaAs . . . . .	62
III.3	Polarization resolved $\mu$ -Photoluminescence $\mu$ -PL . . . . .	64
III.3.1	Principle of the method . . . . .	64
III.3.2	Experimental setup . . . . .	65
III.4	Background on spin and charge transport in GaAs . . . . .	68
III.4.1	The diffusion equation . . . . .	68
III.4.2	Other contributions to the charge and spin transport . . . . .	70
III.4.2.1	Ambipolar coupling . . . . .	70
III.4.2.2	The nature of recombination . . . . .	70
III.4.2.3	Self-trapping effect of the photovoltage . . . . .	71
III.5	Spin and charge diffusion in HVPE-grown GaAs NWs: introduction . . . . .	72
III.5.1	Determination of the doping levels . . . . .	73
III.5.2	Expected specificities of NWs on Si substrates . . . . .	74
III.6	Unpassivated NWs . . . . .	76
III.6.1	Unpassivated NW on GaAs (100) substrate (NW1) . . . . .	76
III.6.2	Unpassivated NW on Si(111) substrate (NW2) . . . . .	77

III.7 Hydrazine passivated NWs . . . . .	78
III.7.1 Principle of hydrazine passivation . . . . .	78
III.7.2 Hydrazine passivated NW on GaAs (100) substrate (NW3) . . . . .	78
III.7.3 Hydrazine passivated NW on Si(111) substrate (NW4) . . . . .	79
III.8 N <sub>2</sub> Plasma passivated NWs on Si(111) substrate (NW5) . . . . .	83
III.8.1 N <sub>2</sub> Plasma passivation process . . . . .	83
III.8.2 Plasma passivated NWs . . . . .	84
III.9 The nature of charge and spin transport in NWs grown on Si(111) . . . . .	86
III.10 Conclusion . . . . .	90
<b>General conclusion</b>	<b>93</b>
<b>Appendix A</b>	<b>99</b>
A.1 Calculation of the $f$ function . . . . .	99
A.2 Estimation of Ga and Si concentrations in the droplet during growth . . . . .	100
A.3 DFT input data and relaxed geometry . . . . .	103
<b>Appendix B</b>	<b>105</b>
B.1 Resolution of the diffusion equation in a NW . . . . .	105
B.2 Poisson's equation in NWs . . . . .	111
B.3 Surface photovoltage . . . . .	113
<b>Bibliography</b>	<b>115</b>
Bibliography . . . . .	115







## Résumé

Alors que la croissance par HVPE de nanofils GaAs est bien maîtrisée à l'Institut Pascal sur substrat de GaAs, quand à elle, la croissance sur substrats de silicium reste un sujet à développer. Dans ce travail, nous proposons dans le chapitre I un procédé expérimental permettant d'obtenir des nanofils de GaAs sur substrat de Si(111) par la voie VLS catalysée Au, accompagnés de structures larges appelées écailles. Ce procédé doit être optimiser si un rapport nanofils/écailles plus élevé est souhaité. Nous avons démontré par in-situ LEEM et LEED que les gouttelles catalyseurs d'Au désoxydent la surface du substrat de Si(111) à haute températures (700 °C) et pompent des atomes de silicium du substrat. L'influence de ces atomes sur la nucléation des nanofils GaAs est étudiée par un modèle thermodynamique présenté dans le chapitre II. Aussi dans le même chapitre, nous présentons une étude de l'incorporation de ces atomes amphotériques de silicium dans le solide GaAs en fonction des paramètres de croissance. Le chapitre III consiste en une investigation du transport de charge et de spin par  $\mu$ PL polarisée dans les nanofils obtenus. Nous avons trouvé des longueurs de diffusion record à basse température dans des nanofils passivés à l'hydrazine et par N<sub>2</sub>-plasma.

**Mots clés:** HVPE, nanofils GaAs, silicium, dopage, transport de charge et de spin,  $\mu$ PL.

## Abstract

Au-catalyzed growth of GaAs nanowires by HVPE technique has been demonstrated in Institut Pascal many years ago on GaAs substrates. However, the current trend is to integrate these nanowires on silicon substrates, which appears to be very useful for some applications. It is the subject of the present work to develop such process using HVPE which an exceptional length along with very good crystalline quality of nanowires. This manuscript is organized into three chapters. Chapter I is devoted to present the experimental process allowing to obtain such nanowires on Si(111) substrates by Au-catalyzed. It contains also a study of the dewetting of ultra-thin gold films on oxidized Si(111) substrates as function of different parameters, in which we show also by in-situ LEEM and LEED experiments how these droplets remove the SiO<sub>2</sub> from the surface and pump silicon atoms from the substrate. The influence of these silicon atoms on the nucleation of GaAs nanowires is presented in chapter II through a thermodynamic model. Another model is also presented in the same chapter in which we study the incorporation of the amphoteric silicon atoms in the solid phase as function of different growth parameters. Chapter III consists in an investigation of charge and spin transport using a polarized  $\mu$ PL experiment on ultra-long GaAs nanowires produced by HVPE. We study the effect of the surface passivation of these nanowires by hydrazine solution and N<sub>2</sub>-plasma. We report record diffusion lengths for both charge and spin.

**Key words:** HVPE, GaAs nanowires, silicon, doping, charge and spin transport,  $\mu$ PL.

# Acknowledgments

As Jean de La Fontaine said: "In every thing, the end should be considered".

Here it is, the end of my PhD at Institut Pascal. Three years of my youth were spent to achieve this work. Three years full of work, patient, stress and fatigue. This is not a complaint, because I know that I (and no one) wouldn't do better than what I have done. I am not at all talking about the scientific level of my work! It is simply about the good relations with "great" people that I have met during these years.

Foremost, I would like to express my sincere gratitude to my advisors Christine Robert-Goumet and Yamina André for giving me the opportunity to do research and providing invaluable encouragement and continuous support during my PhD. A big thank also to Guillaume Monier and Evelyne Gil for their help all along my thesis. Your intelligent ideas were always very relevant and brought valuable results to my thesis. Beside science, a deep thank for all of you for your friendship, empathy, and great sense of humor. Frankly speaking, I was really lucky to work with people like you. *Je vous remercie de tout mon cœur.*

My thanks and appreciations go also the committee members for accepting our invitation to participate to my PhD defense. A special thank is dedicated to the reporters, D.R. Frank Glas and Associate Pr. Jonas Johansson, for the time they have devoted to read and review my manuscript.

A very big part of my gratitude goes to Pr. Vladimir Dubrovskii who helped me a lot doing the work presented in the second chapter of this manuscript. Without your help, and the stimulating discussions with Frank Glas, this work would have been a little success. I am very happy to have my name appearing with yours on my first two papers. Thank you as well for inviting me during Christmas vacation to your houses in Saint Petersburg and Peski where I met your lovely mother. It was a wonderful experience that will never forget.

This manuscript would have been without the third chapter if D.R. Daniel Paget didn't give me the opportunity to work with him in his laboratory Physique de la Matière Condensée of Ecole Polytechnique in Paris. I owe a huge thank to you for that, as well as for teaching me a lot of things in spectroscopy and helping me to write the third chapter. I will never forget the hours we have spent together doing experiments.

I would like to thank also Pr. Frédéric Leroy for inviting me to do experiments in his laboratory CiNaM, Marseille.

Locally, I am grateful to my friends Mohammed, Geoffrey, Gabin, Jihen, with whom I spent wonderful moments in and out the work place, and to all the Lebanese community in Clermont-Ferrand.

Finally, the greatest event of these three years is my meeting with my love *DANA* to whom I owe a lot of gratitude for support and encouragement.



*To my parents, sister, brothers  
and my beloved Dana,*



# General introduction

**I**N recent years, the scientific community has been showing a huge interest in semiconductor nanowires (NWs). The very high surface to volume ratio of such structures as well as the high sensitivity of their properties to the surface phenomena make them very potential candidates for the fabrication of devices. As an example, due to their unique physical light absorption properties, the limit of how much energy we can utilize from the sun's rays is higher than previous believed [1, 2]. Another powerful application for NWs is for light emitting. Flexible NW-based LEDs are under development and expected to be commercialized in the not too far future [3].

Many techniques have been developed to fabricate these structures, the most important of which are the molecular beam epitaxy (MBE), the organometallic vapor phase epitaxy (OMVPE) and the lesser extent one the hydride vapor phase epitaxy (HVPE). In the present work, only the later will be studied. It has been developed in the group *3VAH* of Institut Pascal since the 1970s for the growth of III-V planar layers. In the last decade, Institut Pascal has demonstrated the successful growth of GaAs nano-objects by SAG-HVPE (selective area growth-HVPE) [4] and GaAs nanowires by Au catalyst-assisted-HVPE [5, 6] on GaAs substrate. GaAs nanowires will be the kernel of this manuscript from their growth mechanism and modeling, to their surface passivation and transport properties.

The HVPE technique benefits from the high material input and high dechlorination rate of the element III precursors to grow gallium arsenide (GaAs) NWs of exceptional lengths with an extremely high growth rate that can reach  $170 \mu\text{m}\cdot\text{h}^{-1}$  along with a pure crystalline quality. These results have been obtained for gold-catalyzed vapor liquid solid (VLS) growth on GaAs substrates during previous thesis works in Institut Pascal [4, 7]. However, the current trend is to replace GaAs by silicon (Si) substrates, which are known to have reduced cost and suitable properties for some applications. It is therefore the first purpose of the present work to grow GaAs NWs on Si(111) substrates using the HVPE technique, in the hope of combining the exceptional properties of ultra-long GaAs NWs with those of Si substrates.

However, as shown in Chapter I of this manuscript, replacing a substrate by another can be responsible for changing the whole growth process. First of all, we start with a presentation of the thermodynamics and kinetics of the HVPE process. Then, since the formation and composition of catalyst droplets are very sensitive to the type of the substrate used, we also present a study on the

dewetting of ultra-thin gold films on Si(111) substrates. We show how Au droplets pump Si atoms from the substrate when heated at high temperature (700 °C). It is shown as well the role of the native oxide (SiO<sub>2</sub>) layer and its substantial influence on the growth of NWs. In a next step, we present the most important results obtained for Au-catalyzed NWs growth on Si(111) substrates.

Chapter II is devoted firstly, to the study of the influence of the Si atoms present in the catalyst droplets on the nucleation of GaAs NWs. A thermodynamic model is developed based on the calculation of the chemical potential required to transform a GaAs pair to solid phase from a liquid containing Si atoms. A comparison of this energy with a reference state, where no Si atoms are present in the process (case of undoped NWs on GaAs substrates), allows us to figure out if the presence of Si atoms enhances or reduces the nucleation rate of GaAs NWs. The results are compared with some experimental data that show a good consistency with the model. In the second section, we present another thermodynamic model to study the incorporation of these atoms in the GaAs solid phase. More precisely, we study the behavior of the *amphoteric* Si dopant in GaAs NWs as a function of various parameters corresponding to different growth techniques. Our theoretical predictions are then compared with experimental measurements and results obtained in the literature to test the validity of our model. The models of Chapter II were obtained in collaboration with Pr. Vladimir Dubrovskii from ITMO University in Saint Petersburg, Russia.

Chapter III consists in an investigation of the charge and spin transport in GaAs NWs grown by HVPE on Si(111) substrates. To do so, we use a  $\mu$ -polarized Photoluminescence ( $\mu$ PL) technique that gives a direct imaging of the charge and spin densities simultaneously. Different types of NWs have been studied, exhibiting different characteristics in terms of doping, diameter, surface passivation, etc. We will show that the transport properties are largely enhanced after surface passivation either by chemical hydrazine solution or by N<sub>2</sub> plasma treatment. The later passivation method has been developed in the *Surfaces et Interfaces* group of Institut Pascal, where very good results in terms of PL intensity enhancement have been obtained for GaAs(100) planar layers [8, 9]. We will explain, through a qualitative description, how charge and spin are transported in such NWs. Unpredictable results with record diffusion lengths will be reported. This study has been developed in collaboration with the research director Daniel Paget who gave me the opportunity to work with him over several stays in his laboratory Physique de la Matière Condensée (PMC) at Ecole Polytechnique in Palaiseau.





# Surface preparation of Si(111) substrates and Gallium Arsenide nanowires growth by Hydride Vapor Phase Epitaxy (HVPE)

## I.1 Hydride Vapor Phase Epitaxy for GaAs Nanowires

### I.1.1 Introduction

**O**VER the last decades, the fabrication of III-V (Ga,In)-(As-P) semiconductor structures has attracted attention given their importance in many industrial fields. In order to ensure this tremendous demand, different epitaxial growth processes have been developed, each providing structures and compounds with specific properties. Today, the largest volume process for the industrial production is Vapor Phase Epitaxy (VPE), which dates back to the 1960s. A number of epitaxial growth techniques based on the use of a gaseous mother phase have been developed. The earliest ones are the halide or chloride VPE in which both growth materials were supplied by chlorides, such as  $\text{AsCl}_3$  or  $\text{PCl}_3$  and  $\text{GaCl}$  or  $\text{InCl}$ . Another powerful technique is hydride VPE (HVPE). In this technique, the elements V are supplied as hydride ( $\text{AsH}_3$ ,  $\text{PH}_3$  or  $\text{NH}_3$ ) and the elements III are supplied as III-Cl ( $\text{InCl}$  and  $\text{GaCl}$ ) by flowing separate HCl gaseous flux over in-situ element III liquid sources at high temperature. The main advantages of the HVPE technique are the ability to grow materials of high quality, with a high growth rate. Its principle is relatively simple and allows a good flexibility in terms of doping, shaping and compositional tailoring of compounds such as  $\text{Ga}_x\text{In}_{1-x}\text{As}_y\text{P}_{1-y}$ . However, as the elements III are produced inside the growth reactor, some technological limitations encountered indeed in the HVPE process. As a matter of fact, abrupt composition variations in multijunctions are difficult to manage since the response time to gas switching is relatively high. Furthermore, the growth of alloys containing aluminum is almost impossible in HVPE. The use of Cl-based precursors needs a severe control of the overall pressure, the temperature profile along the reactor and the Cl composition in the vapor phase in order to avoid parasitic deposition on

the reactor's hot wall, especially with Al-chloride growth precursors. Consequently, HVPE has been almost completely replaced by more flexible techniques for the growth of heterostructures, such as Molecular Beam Epitaxy (MBE), MetalOrganic VPE (MOVPE), nay Chemical Beam Epitaxy (CBE).

Unlike VPE growth techniques mentioned above, MBE consists of growing materials under Ultra High Vacuum (UHV) by injecting atoms or molecules on the surface of a substrate handled at high temperature. It allows the growth of epilayers with a growth rate of about 1 atomic monolayer per second. A very powerful feature of the MBE is the possibility to integrate characterization techniques to the growth chamber, which allows to observe in-situ the growth process. Because of that, this technique has been for decades the leader for the fabrication of low-scale structures. The first layers showing a quantum confinement were grown by MBE. Moreover, MBE has been the most used technique for the development of band-gap engineering.

MOVPE has long been considered as the leading technique for the production of III-V materials, especially for Light Emitting Diodes (LEDs) and solar cells. The ability to produce large wafers makes this technique the best one for the commercial scale production of, for example, AlGaInN for solar cells, AlGaInP for visible LEDs, injection lasers, etc. Today, commercially available reactors can be found in the market both for research and production-scale applications.

CBE refers to the technique in which the growth of III-V semiconductors is performed, as for MBE, under UHV using organometallic and hydride precursors to supply the elements III and V, respectively. This gives certain advantages over the other techniques, such as the instant flux response required for multijunctions heterostructures and the easy implementation of in-situ characterization instruments. Even though, it remains dedicated for research and is still less used for commercial production.

Currently, the industry of semiconductor devices moves continuously towards miniaturization of compounds while increasing their performance. This was the main impetus to develop some materials with certain geometries, allowing the improvement of both the size and the quality of structures. Hence, semiconductor nanowires (NWs) are particularly suited to these new requirements.

## **I.1.2 III-V semiconductor NWs**

The story began in 1964 with Wagner and Ellis who demonstrated that one-dimensional silicon structures, i.e. NWs, can be grown on silicon substrate by means of a pre-deposited gold catalyst seed [10]. Of course, the experiment was performed at sufficiently high temperature (950 °C) to make liquid the catalyst particle. This experiment was the key to a new concept of growth from the vapor phase, which they have called Vapor-Liquid-Solid (VLS) mechanism. By that time, the race was declared by the scientific community supported by the very promising properties of these 1D structures. Its end line was the possibility to integrate these latter in various devices such as electronic [11], optoelectronic [12, 13], photonic [14], photovoltaic [15], sensing [16] onces so on. Until now, this target is still not fully reached because of some processing issues. However, some groups have succeeded to overcome these difficulties and start to reap the benefits of long years of research.

From a technological point of view, NWs can be defined as nanostructures having a very high surface to volume ratio and exhibiting a high crystalline quality, without dislocations caused by lattice mismatch with the substrates, which is valid also even if the difference of thermal expansion between the structure and the substrate is high. This helped the NWs to find their rightful place at the heart of devices manufacturing where the attempts of other structures have failed. On the other hand, ecologically speaking, this kind of structures could reduce materials consumption compared to planar devices.

Currently, NWs are being investigated and integrated in photovoltaic applications. Wallentin et al. have demonstrated that an efficiency of 13.8 % could be obtained with InP NWs, along with a higher open-circuit voltage compared to the planar counterpart. They have shown as well that the performance of solar cells can be modulated by engineering the shapes of NWs [15]. Another powerful application of NWs is for sensing devices, relying on their high surface for enhanced chemical interaction with the desired molecules. NWs can be implemented as single, multiple or network in gas sensor devices [17]. In terms of electronic devices, Mongillo et al. have shown that silicon NWs could be good candidates for multiple-gate devices. In their pioneering work, they have demonstrated that, by tuning the effective Schottky-barrier height, a single NW could be configured to work as a Schottky diode, a Schottky barrier transistor, or a p-n junction with tunable polarities [18]. Another leading work is done by Cui et al. in 2002 with the realization of field effect transistor (FET) based on Si NWs. They have reported substantial advantages for those building blocks compared to planar layers. They have found a hole mobility that was one order of magnitude higher than that of planar layers ( $560 \text{ cm}^2/\text{V.s}$  compared to  $40 \text{ cm}^2/\text{V.s}$  for bulk Si), along with higher transconductance [19]. Moreover, nitride NWs (III-N) are actively developed for LED applications. Indeed, it seems that the relaxation of stress at the interface with the substrate could hinder the separation of phases of InGaN alloys at high In concentration, allowing therefore a better incorporation of In in GaN NWs with respect to 2D layers. This offers the possibility to circumvent the absence of efficient green LEDs [20]. Furthermore, we will discuss in the last chapter the investigation of charge and spin transport in GaAs NWs as a first attempt to develop quantum memories.

After this brief list of possible applications based on NWs, the first question that comes to mind is: how to fabricate them? If we go through the literature we figure out that the most used techniques are MBE [21, 22, 23], MOVPE [11, 15] and HVPE [24, 25, 6, 5] for many III-V and III-N semiconductors, each of them ensuring properties suitable for dedicated applications. What we are concerned with in this manuscript is the growth of GaAs NWs by HVPE. Thus, in what follows, we will present the leading studies for all growth techniques in order to situate the present work. Just before, the structural properties of GaAs NWs are discussed.

### **I.1.3 Gallium Arsenide NWs: crystallographic properties**

GaAs NWs usually exhibit two common phases: the zinc-blende (ZB) as the GaAs in bulk phase, and the metastable wurtzite (WZ) phase which can be found in unstable bulk crystal [26]. The occurrence

of one or the other depends on the growth circumstances like temperature, mass input of precursors and preferential nucleation sites as will be discussed below. Since both phases can appear in NWs, it is essential to start with the difference between them at the atomic scale.

It is commonly known that the crystal phase of bulk GaAs is zinc-blende. The name often refers to  $\alpha$ -ZnS from the German Zinblende. As shown in Fig. I.1-a, it is a face centered cubic (fcc) structure having a lattice constant of  $a_{ZB} = 5.65 \text{ \AA}$ , and containing two sub-lattices at  $(0, 0, 0)$  and  $(1/4, 1/4, 1/4)a_{ZB}$ , filled with Ga and As atoms, respectively. Seen along the  $[111]$  direction, the ZB structure shows planes of the same kind of atoms. In other words, a GaAs grown along the  $[111]$  direction can be terminated either with a plane of Ga atoms, which is called in this case GaAs(111)A, or with As atoms for GaAs(111)B otherwise. In order to enhance the stacking inside the structure, subsequent bilayers of GaAs(111)A and GaAs(111)B change orientations with respect to the first bilayer. In ZB crystal structure, the stacking sequence reoccurs after the third bilayer, which is represented as “ABCABC” sequence (see Fig. I.1-c). The distance between two subsequent planes GaAs(111)A and GaAs(111)B is  $\frac{1}{\sqrt{3}} a_{ZB} = 3.26 \text{ \AA}$ , while the distance between two neighboring atoms in a (111) plane is  $\frac{1}{\sqrt{2}} a_{ZB} = 4.00 \text{ \AA}$ .

On the other hand, ZB phase is not the only existing packed structure for GaAs. Another one is the hexagonal close packed (hcp), known as wurtzite phase for binary compounds (see Fig. I.1-b). Unlike ZB, WZ has a “ABABAB” stacking sequence and shows a hexagonal lattice. In Fig. I.1-b, this lattice is reported for GaAs, with a hexagonal lattice constant  $a_{WZ} = 3.99 \text{ \AA}$  along the  $[11\bar{0}0]$  direction and  $c_{WZ} = 6.56 \text{ \AA}$  along the  $[0001]$  direction [27].

In NWs, both of the phases presented above can be obtained. Again, the surface to volume ratio in these structures is very high compared to bulk materials, thus the surface energy plays a more important role. In one hand, the WZ phase has a lower number of dangling bonds on the NW side facets, which manifests as a lower surface energy for this phase. On the other hand, the ZB phase possesses a cohesive energy, between an atomic pair, about 24 meV lower than in WZ [26]. Given that, it can be easily imagined that the growth of NWs is a competition between the two phases. In 2007, Glas et al. compared the total energy that has to be raised when precipitating a WZ or a ZB nucleus at different nucleation sites. According to their paper, the wetting of the catalyst droplet, and therefore the favored nucleation site, has a key role in the interplay of the two phases [28]. One year later, Dubrovskii et al. reported the dependence of the chemical potential for ZB and WZ phases on the supersaturation of the catalyst droplet and its radius [29].

Since the growth of GaAs NWs occurs layer-by-layer, stacking faults and rotational twins are usually detected along the growth direction. As revealed from the name, a rotational twin is defined as an inversion of “ABC” into “CBA” sequence, which corresponds to the rotation of the “ABC” sequence of the ZB by  $180^\circ$  around the growth axis (see Fig. I.1-d). This results in the formation of a WZ monolayer with an “ABA” stacking sequence. Therefore, a ZB lattice can be fully transformed into WZ if rotational twins occur every second monolayer. This is represented by the thin dashed line on the Fig. I.1-e.

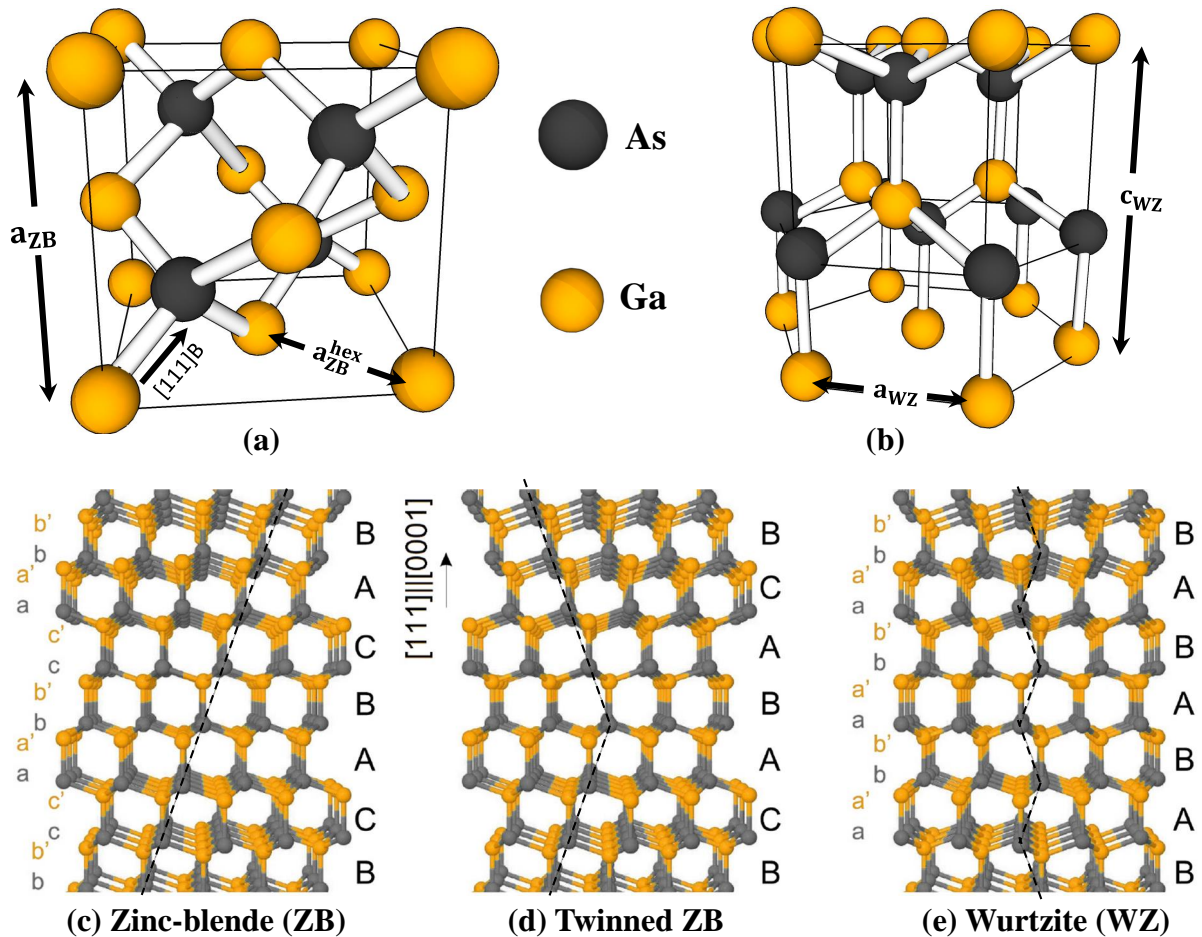


Figure I.1: (a) The zinc-blende (ZB) lattice consists of two fcc lattices displaced by  $(1/4, 1/4, 1/4) a_{zB}$ . These lattices are either occupied by Ga or As atoms. Along the  $[111]$  direction, subsequent bilayers are stacked in an ABCABC sequence. (b) The wurtzite (WZ) phase is a hexagonal close packed crystal with a stacking sequence of ABABAB. (c) Zinc-blende (ZB), (d) twinned ZB and (e) wurtzite (WZ) crystal structure along  $\langle 1\bar{1}1 \rangle \parallel \langle 11\bar{2}0 \rangle$  viewing directions. The corresponding stacking sequences are marked with capital letters.

#### I.1.4 Nanowires growth by different epitaxial techniques: state of the art

Growth of GaAs NWs has long been an active subject for research. Without competition, the first growth technique that comes to mind while speaking about NWs growth is MBE. This technique is considered as the most controlled one since all the growth parameters can be tuned accurately, such as growth temperature and precursor fluxes, with in addition, integrated in-situ characterization techniques to follow the growth mechanism step-by-step [30].

For more than ten years, growth of Au-catalyzed GaAs NWs by MBE has been reported on GaAs substrates. In 2005, Dubrovskii et al. studied the dependence of NWs lengths on the size of gold catalyst particles. Moreover, they have shown that the growth of NWs exhibiting diameters lower than 100 nm involves mainly the diffusion-induced growth. In other terms, the diffusion of ad-atoms from the substrate to the top of NWs during MBE growth of GaAs NWs on GaAs(111)B activated

by Au considerably increases the length of NWs, especially for low diameters ( $<100$  nm) [21]. In the same year, Harmand et al. analyzed the composition and the crystal structure of the catalyst Au particle after different configurations of NW growth [22] (see Fig. I.2). Their main conclusion was the confirmation that the catalyst droplet is liquid during growth at  $590$  °C, which is far below the melting point of Au. Two years later, they confirmed that by in-situ RHEED measurements and studied the effect of growth temperature, which shows optimal results at around  $580$  °C [23].

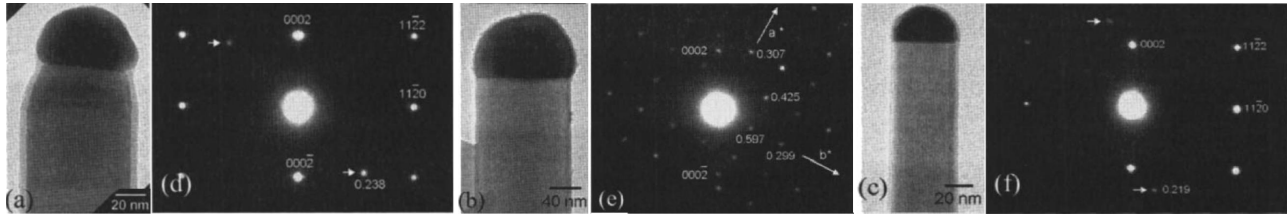


Figure I.2: *HR-TEM views showing the ends of three types of NWs after growth at  $630$  °C: (a) NW A: 45 min of growth, the Ga flux was stopped at the end of growth while  $As_2$  was maintained for 2 min at  $590$  °C; (b) NW B: 45 min of growth, the Ga and  $As_2$  were stopped simultaneously before cooling down the substrate; and (c) NW C: the same termination of B except the growth time was 160 min. (d), (e) and (f) are the corresponding electron diffraction patterns of droplets A, B and C, respectively. [22]*

In 2008, a new concept of catalysis was introduced by the outstanding studies published nearly simultaneously of Colombo et al. [31] and Jabeen et al. [32] who showed that GaAs NWs can be grown by self-assisted process in MBE, i.e. with gallium droplet instead of gold (see Fig. I.3). For instance, in the first work the growth temperature was  $630$  °C with an arsenic partial pressure of  $7.9 \cdot 10^{-6}$  Pa and a gallium rate of  $0.25$  Å/s. The authors made use of a  $10$  nm  $SiO_2$  buffer layer deposited on (111)B and (100) GaAs substrates in order to form gallium droplets in preferential defect sites. These works have opened the way towards further development of this approach for NW growth. Since then, engineering and control of self-assisted GaAs NWs have never stopped evolving and progressing.

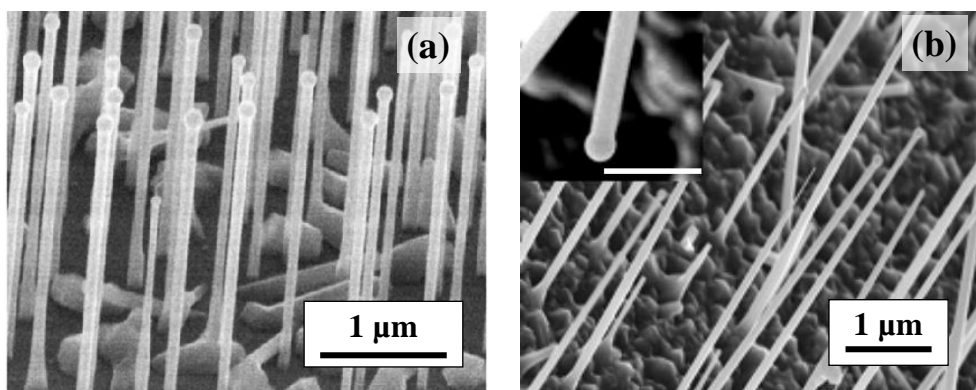


Figure I.3: *Scanning electron micrographs of MBE grown GaAs NWs obtained by (a) Colombo et al. on a (111)B GaAs substrate sputtered with a  $10$  nm  $SiO_2$  layer [31], and (b) Jabeen et al. on Si(100) cleaved wafers [32]. The inset (scale bar  $200$  nm) shows a detail on the final end of a selected NW.*

Very recently, Harmand et al. have published an impressive experimental work showing, in-situ, the layer-by-layer growth of self-catalyzed GaAs NWs by MBE [30]. Their observations were in a full agreement with the predictive models reported some years earlier by Glas and Dubrovskii [33, 34].

Besides MBE, another existing powerful technique to grow GaAs NWs on GaAs substrates is MOVPE. This technique had been developed many years before MBE and has shown very good results in both Selective Area Growth (SAG) and VLS growth processes. Even though the fundamental concept of the two processes is different, with both of them, GaAs NWs with controllable diameter and growth rate can be obtained. In terms of SAG, the first study was published in 1991 by Hiruma et al. who obtained GaAs NWs as thin as 100 nm in a SiO<sub>2</sub> mask deposited on (111) GaAs substrates [35]. Some years after, Hamano et al. have shown that the growth rate ( $R_g$ ) of micropillars grown on (111) GaAs substrates with a silicon oxide mask is higher than conventional MOVPE epitaxy, although a lower partial pressure of trimethylgallium (TMG) was maintained [36]. Also, they found that  $R_g$  is function of  $1/r$ , where  $r$  is the radius of the structures. Since then, several years of optimization have led to a very good understanding and control of the growth of GaAs NWs by SAG-MOVPE [37, 38].

Concerning VLS process, in 1995 Hiruma et al. were the first to report the feasibility of Au-assisted quantum GaAs NWs of diameters between 15 and 40 nm on (100) GaAs substrates. They found that the growth direction was [111], and the NWs exhibited the WZ phase with some rotational twins that separate ZB sections [39]. In 2007, another group have investigated the effect of growth temperature on the growth rate of Au-catalyzed  $\langle \bar{1}\bar{1}\bar{1} \rangle$  GaAs nanowhiskers on (111)B GaAs substrate, and found an optimum between 450 and 475 °C [40]. A very relevant work comparing VLS and SAG MOVPE growth was published in 2010, in which the optimal growth conditions have been reported with a fine description of the structural quality [38]. However, this technique has shown its inability to grow self-assisted NWs as controlled as in MBE, despite some attempts in this way [41]. The main problem is that depositing Ga liquid droplets from element III gaseous precursors (Trimethylgallium TMGa) is not favorable thermodynamically, unless working at very low temperature, namely 600°C.

For several years, the group 3VAH in Institut Pascal is being interested in GaAs NWs growth by HVPE. The first NWs were obtained accidentally during the thesis of Réda Ramdani (2005-2009) defining the starting point of the activities on NWs growth in Institut Pascal. He has demonstrated that very long NWs with exceptional lengths and pure ZB crystal structure can be obtained by HVPE [5]. The growth rate was 170  $\mu\text{m/h}$  for a growth temperature of 715 °C and a III/V ratio of 5. The very high value of elongation rate is exclusive for this technique and considered to be the main advantage to take up the challenges imposed by MOVPE and MBE, which do not exceed some  $\mu\text{m/h}$ . The reasons standing behind that are the high material input ( $3 \times 10^2$  and  $1.2 \times 10^2$  Pa for GaCl<sub>g</sub> and AsH<sub>3g</sub>, respectively) and the high dechlorination rate of the element III precursor (GaCl). In addition, the HVPE process is proven to be a cost-effective technique for Au-assisted GaAs NWs [6, 5, 42].

However, the current trend is to integrate III-V NWs on silicon substrates given the very promising applications in optoelectronics [43]. Indeed, silicon is the most widely used material in semicon-

ductor industry [44], and this is for many reasons: the existence of abundant reserves in our planet which makes it a low-cost semiconductor compared to others (i.e. Ge, GaAs, . . . ); no complex processing between the extraction and getting substrates ready for use; its mechanical strength allows the fabrication of 300 mm platforms; the high hole mobility which is important for high-speed field effect transistor (FET); etc. However, its indirect band gap and the low electron mobility are major drawbacks preventing its implementation in active optical devices applications and some electronic devices.

Therefore, combining silicon with III-V semiconductors to make profit from the properties of both materials is at the center of interest nowadays. However, this way is full of difficulties that should be encountered when we deal with 2D epitaxial layers. Here again is the importance of the NW shape. First, given the low lateral dimensions of NWs, these latter can be grown without strain, and therefore, without dislocations inside the structures due to the lattice mismatch between the two materials which is reported to be about 4% [45]. Another issue that we can get rid of when using NWs is the difference of thermal expansion coefficients ( $6.6 \times 10^{-6} \text{ K}^{-1}$  for GaAs and  $2.3 \times 10^{-6} \text{ K}^{-1}$  for Si) and the related induced dislocations [46].

However, there is still one difficulty standing behind the inability of growing GaAs NWs on silicon substrate by HVPE, which is the low interface energy between the Au droplet and the substrate compared to the one between Au and GaAs. As we will see in the next section, this leads to the formation of a parasitic buffer layer that considered annoying for some applications.

While the growth of GaAs NWs on silicon substrates was performed (both by Au- and self-catalyzed processes) successfully by MBE, MOVPE and HVPE have shown limited progress, despite the serious attempts reported in the last few years. Indeed, Breuer et al. have studied the self-catalyzed growth of GaAs NWs by MOVPE on Si(111) substrates and shown that the nucleation can occur at  $600^\circ\text{C}$  using low III/V ratio ( $\sim 1$ ) [47]. However the density and the randomness of the structures are still far from being controlled. The same observations were found by Dong et al. using HVPE [48] (see Fig. I.4 ). This may due to some thermodynamic issues which are the subject of the second chapter of this manuscript.

After several unsuccessful attempts to optimize self-assisted HVPE growth, getting organized NWs with controlled density and shapes seems to be more challenging than expected. This is why we have decided to focus on the Au-catalyzed growth process.

The aim of my work is absolutely not to compete with MBE or MOVPE techniques, it is simply to provide structures that cannot be obtained elsewhere. The exceptional lengths of HVPE NWs could be very useful for many applications, such as thermoelectric, electronic applications and, as we will present in the last chapter of this manuscript, the development of quantum memories. As a matter of fact, these NWs are excellent objects to be studied fundamentally (optical, electronic properties), paving the way for further integration in devices once controllable NWs will be achievable by other techniques.

In the next section, I will present a brief description of the HVPE reactor used during my PhD

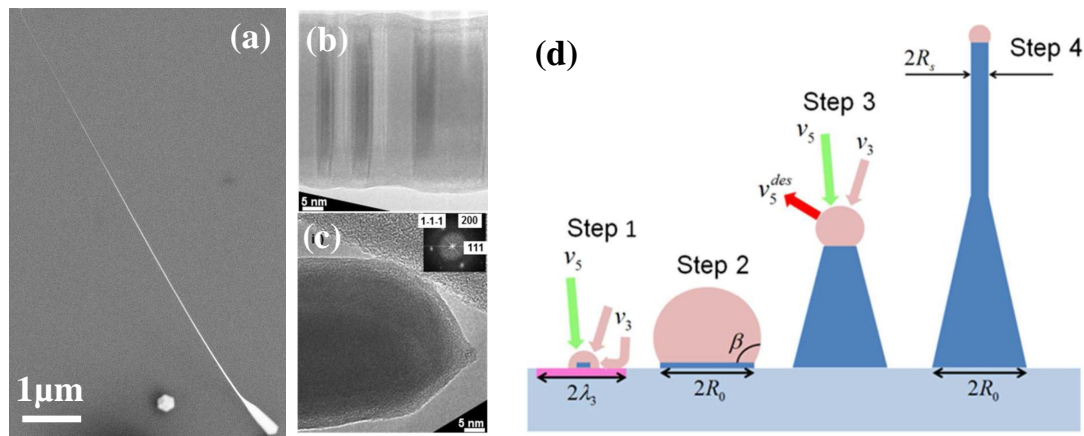


Figure I.4: (a) SEM image showing the existence of GaAs NWs on Si(111) substrate. (b) HRTEM image showing twin defects in the middle part of the NW. (c) HRTEM image of the NW's top with the insert evidencing the pure ZB structure. (d) Schematics of the GaAs NW growth: Step 1 – initial nucleation of the gallium droplet; Step 2 – rapid surface growth of this droplet assisted by the gallium diffusion from the substrate surface, the droplet reaches the size  $R_0$  at which the very first NW ML is completed; Step 3 – growth of a tapered NW base with diminishing the droplet size under excessive arsenic flux, shrinking the droplet increases the arsenic desorption rate due to the Gibbs-Thomson effect; Step 4 – the droplet reaches its stationary size and the NW top becomes straight. [48]

work, as well as the thermodynamics and kinetics processes governing growth in this technique. After that, we will move to the main results obtained for Au-catalyzed NWs.

### I.1.5 HVPE experimental setup at Institut Pascal

Given all the preceding arguments, it can be clearly understood why it is irrelevant to compete MBE and MOVPE with HVPE. However, there are many reasons standing behind the attention paid to this technique. Indeed, high partial pressures together with high dechlorination rate of the chloride precursors used in HVPE ensure a high supersaturated vapor phase during growth and fast surface kinetics (including decomposition of growth precursors), yielding a modular growth rate going from some to several tens of  $\mu\text{m/h}$ . This offers the possibility to grow very thick epilayers that can be used as quasi-substrates (e.g. GaN). Another advantage is the ability for localized growth on patterned substrates due to perfect selectivity. Moreover, HVPE is known to be one of the best techniques to manage growth anisotropy and the shaping of 3D structures with unusual aspect ratios. A very important point that counts also is that HVPE is a very low cost and low polluting mass production process compared to other techniques.

Even though the various VPE techniques share almost the same foundations of thermodynamics, each of them is very complex when viewed in detail for kinetics at the atomic level. Consequently, until today we still have gaps to fill in order to perfectly understand the mechanisms that govern the growth. However, some models were made and found to be very consistent with the empirical data. As mentioned above, in this manuscript we will be interested only in the HVPE process. This is why

I consider essential to present a brief description of, first, the HVPE reactor of Institut Pascal, and then the thermodynamic and kinetic mechanisms involved in the growth of III-V materials by this technique.

We give here a description of the home-made reactor used in our laboratory. Fig. I.5 depicts a schematic plan of this latter with all the arrival gas lines. It is made entirely of quartz that can hold at very high temperatures (up to 1000 °C) required for growth of some materials without being attacked by corrosive gases involved in the growth processes. As can be seen, this reactor is divided into three zones. The first one (shown in yellow) is where the gases are prepared especially element III precursors. It contains the element III liquid sources (Ga and In), and arrival lines of  $H_2/N_2$  as well as additional HCl flow that is used to control the supersaturation of the vapor phase during growth. The second zone (shown in red) is the mixing zone. It serves to mix precursors of element III prepared in Zone 1 with precursors of elements V introduced directly in this zone. The precursors used for doping (such as  $SiH_4$  and diethylzinc DEZ) can be introduced in this zone as well if needed. The last one called the deposition zone (shown in grey) is where the substrates are placed and where growth takes place. The mixing and the deposition zones are connected with the preparation zone through a manual-controlled drawer-valve. This latter is essential to separate and prevent any early exposure of the substrate to the unstable gases and unprepared precursors. The total gaseous flow is adjusted to be compatible with the geometry of the reactor and ensure a homogeneous mixture of the vapor phase in order to obtain a laminar flow over the substrates.

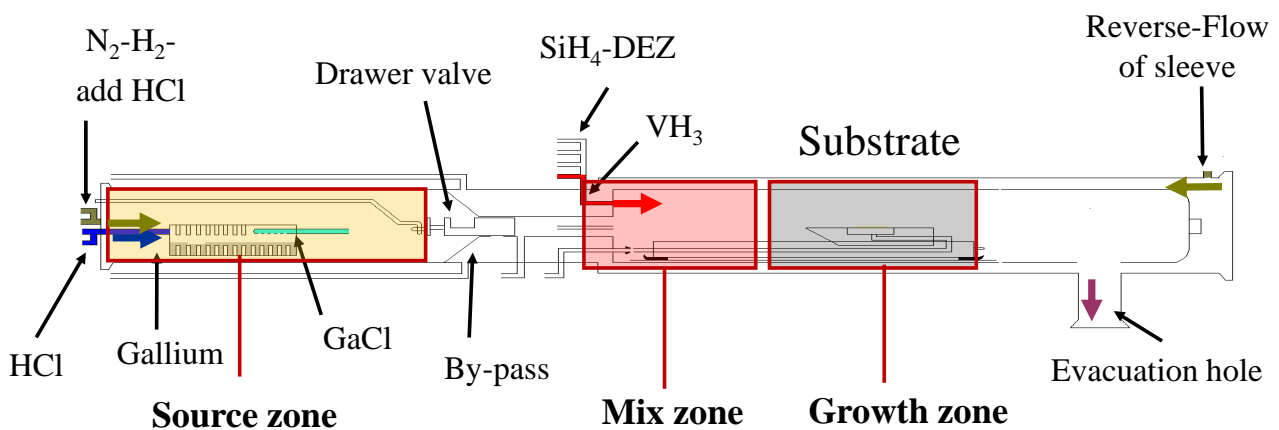


Figure I.5: Schematic representation of the HVPE home-made hot-wall reactor used for the growth of GaAs at Institut Pascal.

The temperature can be regulated by means of an external furnace that encompasses the whole quartz-tube. It is composed of six zones that can be regulated separately in order to control the axial inhomogeneous temperature's profile along the reactor. The deposition zone is maintained at the lowest temperature so that the deposition of materials governed by exothermic reactions (as described later) is favored only on the substrates. Obviously, and for the same reason, the deposition on the hot walls of the reactor in contact with the furnace is hindered, hence the name "hot wall-reactor"

associated to HVPE.

### I.1.6 HVPE process: thermodynamics and kinetics of growth

The synthesis of GaAs by HVPE is a *near equilibrium process*. It involves  $\text{GaCl}_g$  for element III, produced inside the reactor by reacting  $\text{HCl}_g$  with a liquid gallium source at high temperature ( $> 700^\circ\text{C}$ ) according to the following reaction:



Concerning the element V, it is supplied by injecting hydride gaseous precursor ( $\text{AsH}_{3g}$ ) that decomposes immediately when introduced into the hot reactor and transforms into  $\text{As}_{2g}$  or  $\text{As}_{4g}$  [49]:



The global growth reaction governing the formation of solid GaAs in  $\text{H}_2$  atmosphere is given by:



This equilibrium can be determined from the Gibbs free energy of the reaction  $\Delta G(T)$  at the growth temperature  $T$ .  $\Delta G(T)$  is calculated from tables of thermodynamic data relative to the species involved in the reaction. The supersaturation  $\gamma$  of the vapor phase determines whether the formation or the etching of the solid GaAs is favored. In other words, whether the reaction I.3 is driven towards the right or the left side, respectively. This  $\gamma$  depends on the equilibrium constant  $K_i^{eq}(T)$  and the ratio of the partial pressures of the species involved in the reaction [50, 51]:

$$K_i^{eq}(T) = \exp\left(-\frac{\Delta G(T)}{RT}\right) = \left(\frac{[\text{As}_{4g}]_{eq}^{1/4} \cdot [\text{H}_{2g}]_{eq}^{1/2} \cdot [\text{GaCl}_g]_{eq}}{[\text{HCl}_g]_{eq}}\right) \quad (\text{I.4})$$

$$\gamma = \frac{[\text{As}_{4g}]^{1/4} \cdot [\text{H}_{2g}]^{1/2} \cdot [\text{GaCl}_g]}{[\text{HCl}_g] \cdot K_i^{eq}(T)} - 1 \quad (\text{I.5})$$

where  $[i]$  is the partial pressure of the species  $i$ . Thus,  $\gamma$  is the parameter used to measure the deviation of the reaction from its equilibrium. Depending on its sign, we can predict if the growth is favored or not:

$\gamma = 0$  refers to equilibrium between reactants and products,

$\gamma > 0$  corresponds to the formation of solid GaAs,

$\gamma < 0$  corresponds to a forced etching of the existing solid GaAs.

According to Eq. I.5, this supersaturation can be varied by controlling the amount of  $\text{HCl}_g$ ,  $\text{GaCl}_g$  or  $\text{H}_{2g}$  introduced in the reactor. This is why HVPE reactors are often equipped with an independent line of HCl flow. Apart from the temperature profile, this flow is the most used experimental

parameter to control growth in HVPE. The partial pressures of the gaseous species are obtained from the resolution of the equation of the equilibrium constants, the conservation of mass and total pressure inside the reactor during growth (1 atm).

We mentioned above, without giving any explanation, that the growth by HVPE is a near equilibrium process. Actually, according to Stringfellow's calculations, HVPE exhibits a free enthalpy of the deposit reaction that is eight times lower than for far from equilibrium techniques like MBE and MOVPE at 1000 K (see Fig. I.6) [52].

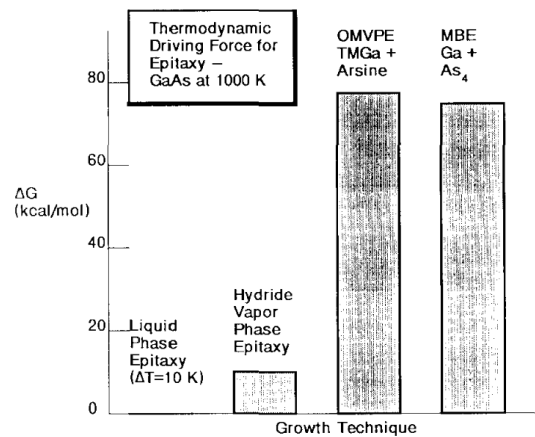


Figure I.6: Estimated thermodynamic driving force, Gibbs free energy difference between reactants and products, for several epitaxial growth processes. All calculations are for the growth of GaAs at 1000 K. [52]

This offers to our technique a wider range of chemical potential difference to set (i.e. much higher driving force is indeed involved) between gaseous and solid phase. Therefore, it is true to say that when the driving force is small, the growth process operates at near-equilibrium conditions. Experimental results showed that a wide range of growth rates, going from 3 to more than 100  $\mu\text{m/h}$ , can be obtained only by controlling the supersaturation of the vapor phase [5]. This is due to the high dechlorination frequency of element III precursors that allows the system to return quickly to its equilibrium state without any kinetic limitations. That is true whether the supersaturation has a low or high value.

Until now, we have provided a description of the thermodynamics governing the growth by HVPE. This gives us a macroscopic view that allows the identification of the existing species and determines the evolution of the reaction. Along with thermodynamics, a kinetic study is essential in order to model the mechanisms involved in the growth. This includes the evaluation of the adsorption-desorption rates of the ad-atoms at the surface of the substrate, the decomposition of ad-molecules as well as the diffusion of the corresponding atoms to the semi-crystal sites, which finally give an equation of the global growth rate that can be compared to experimental observations.

In what follows, we discuss the kinetic model developed in our laboratory by R. Cadoret, E. Gil and A. Pimpinelli describing homoepitaxial growth of GaAs, here applied to the (100) surface [53, 50, 51]. It is based on the near-field approximation of Eyring's theory that allows the calculation

of the adsorption-desorption fluxes of molecules at the surface as function of the activation energies and partial pressures of gaseous species at given pressure and growth temperature. This model is decomposed into three main steps: (i) the adsorption of elements III and V on the surface, (ii) the dechlorination III-Cl ad-molecules and (iii) the diffusion of the ad-atoms (III and V) to the nucleation sites in the semi-crystal. The starting point is the adsorption of arsenic atoms on the vacant sites of the surface. According to reaction I.2, these atoms are obtained in the gas phase instantly after the injection of  $\text{AsH}_3$  at high temperature inside the hot wall reactor. Once localized, a stable chemisorbed complex ( $\text{As-GaCl}$ ) is formed by adsorption of  $\text{GaCl}$  molecules on the surface. In order to continue the growth, the Cl atoms have to be removed from these complex so that As can be adsorbed again. For (100) orientation, this dechlorination represents the limiting step since it is the slowest one in the whole growth process. Two different types of dechlorination mechanisms have been proposed. The first one is the  $\text{H}_2$  mechanism, in which the Cl atoms are removed as  $\text{HCl}_g$  in presence of  $\text{H}_2$  during growth. The second one is more complicated, it consists on the adsorption of a second layer of  $\text{GaCl}$  before the desorption of  $\text{GaCl}_{3g}$ . This mechanism takes place at relative low growth temperatures or at high  $\text{GaCl}$  partial pressure during growth. The growth conditions and the temperature range that I used during this work correspond to the dechlorination by  $\text{H}_2$  mechanism, which is represented schematically in Fig. I.7-a.

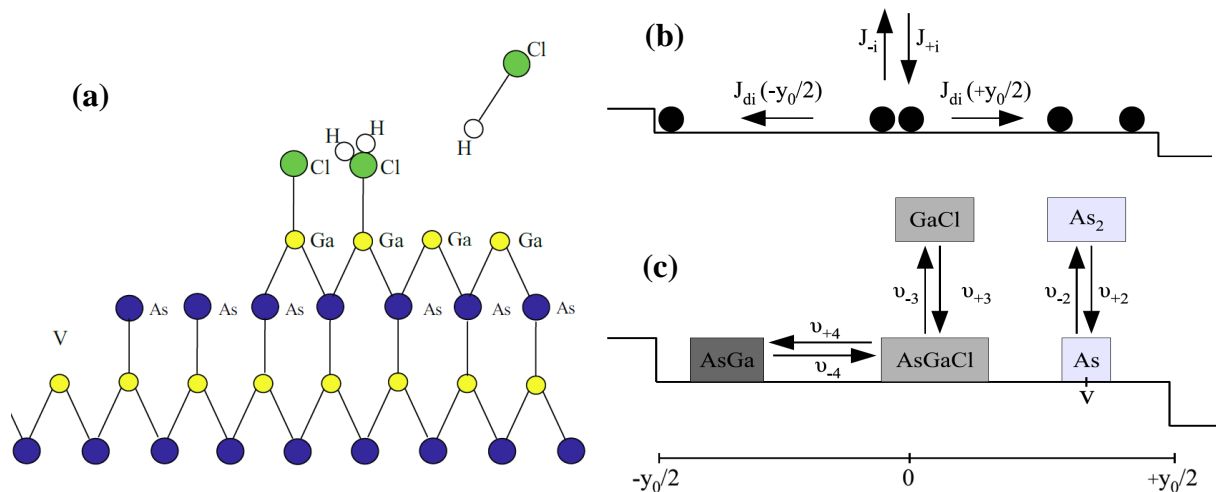
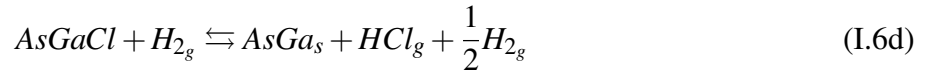


Figure I.7: Schematic representation of (a) the  $\text{H}_2$  dechlorination mechanism of the ad-species  $\text{As-GaCl}$ , (b) the surface processes (adsorption, desorption and diffusion) on a vicinal substrate presenting terraces of width equal to  $y_0$ , and (c) the growth steps of  $\text{GaAs}$  from  $\text{As}_{2g}$  and  $\text{GaCl}_g$ , the adsorption and desorption frequencies of ad-species are represented by  $v_{+i}$  and  $v_{-i}$ , respectively. The dechlorination and chlorination frequencies of  $\text{AsGaCl}$  are represented by  $v_{+4}$  and  $v_{-4}$ , respectively. [53]

To summarize, the elementary reactions governing the growth can be written as follows:





where V is a vacant arsenic site on the surface, the index g and s represent gaseous and solid phases, respectively.

As mentioned before, the kinetic model is based on the calculation of the global fluxes of adsorption  $J_{+i}$  and desorption  $J_{-i}$  of the element i, and the calculation of the surface diffusion fluxes  $J_{d_i}$  of the ad-atoms i until crystal incorporation [see Fig. I.7-b].

Without going into details reported elsewhere, below is a summary of the main equations governing the various mechanisms in our system:

- the adsorption flux :  $J_{+i} = k_{+i}F_{+i}\theta_{vacant}$

where  $F_{+i}$  is the mass input (or the partial pressure of the element i),  $\theta_{vacant}$  is the surface covering ratio in vacant sites, and  $k_{+i}$  is a kinetic constant defined as:

$k_{+i} = C_{+i}(T)e^{\left(-\frac{E_{+i}}{k_B T}\right)}$ , with the pre-exponential coefficient  $C_{+i} = \frac{1}{\sqrt{2\pi m_i k_B T}}$  corresponding to the Ernst-Knudsen classic term, and  $E_{+i}$  the activation energy.  $k_B$  is the Boltzmann constant.

- The desorption flux:  $J_{-i} = k_{-i}\theta_i$

where  $\theta_i$  is the surface coverage of occupied sites with i-type ad-species and  $k_{-i} = C_{-i}(T)e^{\left(-\frac{E_{-i}}{k_B T}\right)}$  is the kinetic constant with  $C_{-i}(T) \propto \prod z$  expressed from the partition functions z of the species involved in the desorption process.

Obviously, the net adsorption flux of species i is the amount of atoms that stays on the surface. In other words, it is the difference between the adsorbed and the desorbed corresponding fluxes [see Fig. I.7-b]:  $J_i = J_{+i} - J_{-i}$ .

On the other hand, it is essential to consider the surface diffusion of species from the adsorption to the incorporation sites, especially for (100) orientation. From the energetic point of view, the stability of an ad-atom on the surface is proportional to the number of bonds that it creates with the atoms on the surface of crystal. Therefore, it can be easily understood why, in what follows, we consider only the growing steps of the crystal as incorporation sites for ad-atoms.

If we assume that the distance between two steps exceeds widely the diffusion lengths, and the ad-atoms diffuse faster than the growth rate of these steps, we will be able to calculate the diffusion fluxes of different species involved in the growth. Considering the conservation of matter on the surface, the diffusion flux  $J_{d_i}$  of species i diffusing towards incorporation sites can be expressed as function of the net fluxes i and i+1:

$$div(J_{d_i}) = J_i - J_{i+1} \quad (I.7)$$

$J_i$  and  $J_{(i+1)}$  are the fluxes of elements as involved in reactions (I.6b to I.6d). This equation means that only the atoms of species i present on the surface according to equation i (for instance I.6b for As) can diffuse before disappearance according to equation i+1 (I.6c for As). That is, for the different

species involved:

$$\text{div}(J_{d_{As}}) = J_{As} - J_{As+1} = (J_{+As} - J_{-As}) - (J_{AsGaCl} - J_{-AsGaCl}) \quad (\text{I.8a})$$

$$\text{div}(J_{d_{AsGaCl}}) = J_{AsGaCl} - J_{GaAs} = (J_{+AsGaCl} - J_{-AsGaCl}) - (J_{+GaAs} - J_{-GaAs}) \quad (\text{I.8b})$$

Concerning GaAs, there is only one equation involved:

$$\text{div}(J_{d_{GaAs}}) = J_{GaAs} = J_{+GaAs} - J_{-GaAs} \quad (\text{I.9})$$

$J_{d_i}$  can be otherwise expressed, according to the Fick's law, as function of the concentration of species  $c_i$  (with  $c_i = N_s \theta_i$ ,  $N_s$  is the number of sites per surface unit) on the surface and the surface diffusion coefficient  $D_i$ :

$$J_{d_i} = -D_i \frac{\partial c_i}{\partial y} \quad (\text{I.10})$$

Now, we need to introduce the adsorption (desorption) frequencies  $\nu_{+i}$  ( $\nu_{-i}$ ) illustrated in Fig. I.7-c:

$$\nu_{\pm i} = \frac{J_{\pm i}}{c_i} \quad (\text{I.11})$$

This allows us to write the following system of coupled equations:

$$\nu_{+3} c_{As} - \nu_{-3} c_{AsGaCl} - (\nu_{+4} c_{AsGaCl} - \nu_{-4} c_{GaAs}) = -D_{AsGaCl} \frac{\partial^2 c_{AsGaCl}}{\partial y^2} \quad (\text{I.12a})$$

$$\nu_{+4} c_{AsGaCl} - \nu_{-4} c_{GaAs} = -D_{GaAs} \frac{\partial^2 c_{GaAs}}{\partial y^2} \quad (\text{I.12b})$$

Gathering all together, we are able to determine the growth rate  $V_g$  of GaAs by considering the time needed to cover the terraces (between two growing steps), that is:

$$V_g = \frac{h}{t} = h \frac{\dot{y}}{y_0} = \frac{\Omega}{y_0} \cdot \left[ -J_{GaAs} \left( -\frac{y_0}{2} \right) + J_{GaAs} \left( +\frac{y_0}{2} \right) \right] \quad (\text{I.13})$$

with  $h$  is the step height,  $t = \frac{y}{\dot{y}}$  the time for covering one terrace,  $\Omega$  is the elementary volume of GaAs, and  $J_{GaAs}$  the diffusion flux of Ga-As ad-species to the step. For the sake of simplicity, this expression can be written as function of the concentration of GaAs:

$$V_g = \frac{\Omega}{y_0} \cdot \left[ D_{GaAs} \cdot \left. \frac{\partial c_{GaAs}}{\partial y} \right|_{-\frac{y_0}{2}} - D_{GaAs} \cdot \left. \frac{\partial c_{GaAs}}{\partial y} \right|_{+\frac{y_0}{2}} \right] \quad (\text{I.14})$$

Resolving eqs. I.12 allows us to calculate the concentration of solid GaAs ( $c_{GaAs}$ ) that can be introduced in eq. I.14 in order to calculate the growth rate. The final numerical expression for the growth of GaAs by the H<sub>2</sub> mechanism on (100) GaAs substrate is given in Ref. [50].

Figure I.8-a shows the variation of the growth rate of GaAs as a function of the temperature: it follows a typical bell curve. Also represented in Fig. I.8-b are the kinetic constant ratio  $k_{+i}$  and  $k_{-i}$  for GaCl and As as a function of T.

The model presented in this section can be extended to other surface orientations, and therefore can describe the lateral growth on the side facets of the NWs growing by VLS process. Moreover,

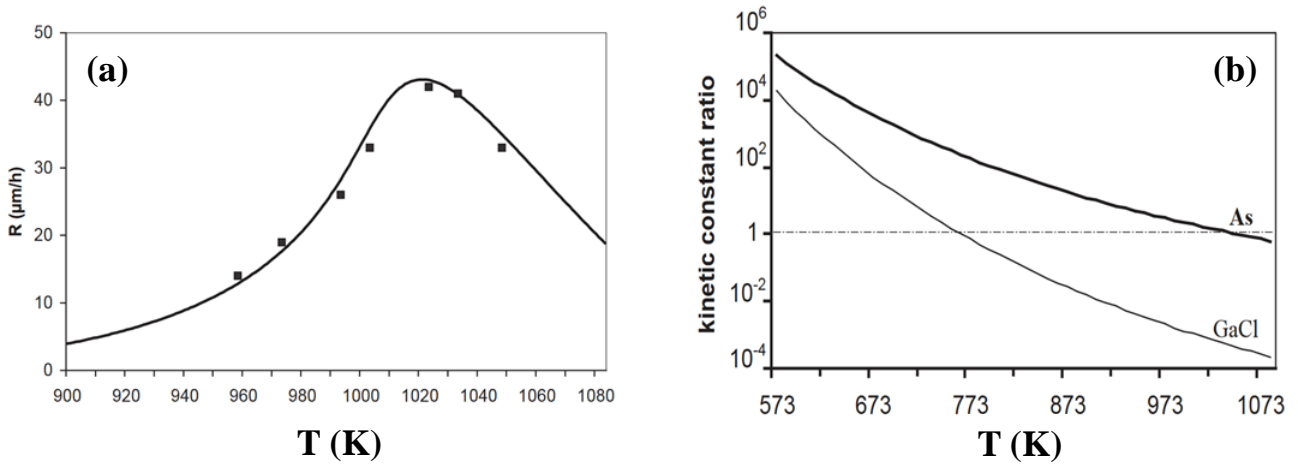


Figure I.8: (a) (001) GaAs growth rate  $R$  in  $\mu\text{m/h}$  as a function of the temperature  $T$  for standard experimental conditions ( $\text{III/V} = 4.5$ ,  $\gamma = 4$ ). The squares are the experimental points; the full line is the computed theoretical curve according to the modeling described in Ref. [50]. (b) Variations of the adsorption/desorption kinetic constant ratio  $k_{+i}/k_{-i}$  for GaCl (thin solid line) and As (thick solid line) as a function of  $T$ . The kinetic constants are part of the adsorption  $J_{ads} = k_{+i}\theta_{vacant}$  and desorption  $J_{des} = k_{-i}[i]\theta_i$  fluxes of species  $i = \text{GaCl}$  or As, with  $[i]$  being the partial pressure of gaseous species  $i$ ,  $\theta_{vacant}$  the surface coverage ratio in vacant sites, and  $\theta_i$  the surface coverage ratio of ad-species  $i$ . The  $k_{+i}/k_{-i}$  ratio gives the contribution of the microscopic states involved in the dynamic surface-vapor system [50]. The actual  $J_{ads}/J_{des}$  ratio should include the input mass of species  $i$  ( $[i]$ ), which ensures sufficient adsorption of GaCl up to 1040 K.

it can be assumed that the high dechlorination rate mentioned above remains valid for VLS when it takes place on the catalyst droplets surface. This explains the very rich Ga regime governing the growth of NWs by HVPE [24, 25, 6].

In what follows, we present an experimental study of the dewetting of Au films on Si(111) substrates in order to form the catalyst droplets. After that, we will discuss the main experimental results obtained for Au-catalyzed growth of GaAs NWs on such substrates. As will be seen, we will show the bright as well as the dark side of our experiments in order to draw meaningful conclusions and understand some fundamental phenomena.

## I.2 Surface preparation: dewetting of gold film on Si(111) substrates

### I.2.1 Introduction

Instability of ultra-thin films has long been an important subject in material science and technology [54, 55, 56, 57, 58]. The high surface to volume ratio of these films produces a high driving force which tends to create discontinuity in order to reduce the total energy of the system. As a consequence, we obtain grains with a distribution that depends on many parameters such as temperature, substrate, deposited thickness, and so on.

One of the most important applications for gold nanoparticles is their ability to catalyze the growth of one-dimensional structures [6, 5, 23, 59]. Gold-assisted growth of NWs based on different materials such as ZnO, GaAs, GaN, InGaAs, Si, Ge and InAs have been performed by the growth techniques presented previously in this chapter [60, 61, 62, 63, 64]. In fact, catalyst droplets act as a mediator between the vapor (gases in the reactor) and the solid (NW) phase. They decompose the precursors, collect and accumulate atoms coming from the gaseous phase, to deposit them as a solid phase at the interface with the substrate once the saturation is reached. Depending on the growth temperature, which differs from one technique to another (in the range of  $450\text{ }^{\circ}\text{C} < T < 715\text{ }^{\circ}\text{C}$ ), one of the two following growth mechanisms can occur: the first is the VLS in which the catalyst droplet is liquid during NW growth [65, 59], and the second is the VSS (Vapor-Solid-Solid) in which the growth occurs by means of solid catalyst droplet [66]. In any case, the diameter of the resulting NW is predefined by the size of the gold droplet. Thus, the study of the morphology and the distribution of the droplets leads to a better control of NWs shape and density. Two methods are used to obtain these droplets: by spin coating of a colloidal solution containing nanoparticles, or by dewetting of ultra-thin metallic films.

In this work we are interested in growing GaAs NWs on Si(111) substrates by VLS process using Au droplets as catalyst, which we form by the dewetting method. While the dewetting of thin gold films on bare Si substrates is widely studied [67, 68, 69], there is still a lack of knowledge about oxidized Si substrates. It is the subject of the present section to describe the formation of gold droplets from ultra-thin gold films on  $\text{SiO}_2/\text{Si}(111)$  as function of different conditions and surface treatments.

It is commonly known that GaAs NWs grow in the  $\langle 111 \rangle_B$  direction in HVPE technique [5, 6]. From an energetic point of view, this growth direction is preferred because the surface energies of the orthogonal directions ( $\langle 110 \rangle$  and  $\langle 112 \rangle$  directions) forming the facets of the NWs are low. Consequently, working on (111) substrates seems to be suitable to obtain perpendicular arrays of NWs.

Three  $\langle 111 \rangle$  n-doped ( $10^{16}\text{ cm}^{-3}$ ) silicon wafers ( $W_1$ ,  $W_2$  and  $W_3$ ) with resistivity of  $6.10^{-12}\ \Omega$  were employed for this study. To check the role of the oxide layer thickness, 5 and 500 nm of oxide were thermally grown (using dry oxidation method) on, respectively,  $W_1$  and  $W_2$  after a chemical etching of their native  $\text{SiO}_2$  (by dipping in 1% HF solution for 3 minutes). The  $W_3$  was

kept with its 1.2 nm-thick native oxide estimated by X-ray photoelectron spectroscopy (XPS). Then, all of the wafers were cleaved into small substrates of size about  $0.5 \times 0.5 \text{ cm}^2$ . In what follows, we name  $E_1$ ,  $E_2$  and  $E_3$  the samples coming from  $W_1$ ,  $W_2$  and  $W_3$  wafers, respectively. The Ultra-High Vacuum (UHV) chamber of the Surfaces et Interfaces group of Institut Pascal was used for vapor deposition of pure gold films, post-deposition annealing, and *in-situ* combined XPS/EPES (elastic peak electron spectroscopy) measurements [70]. This chamber allows us to work at very low pressure in the range of  $10^{-7}$  Pa, and is equipped with a Knudsen cell that can deposit pure gold with a rate of about  $0.02 \text{ nm} \cdot \text{min}^{-1}$  when heated at  $1100 \text{ }^\circ\text{C}$ , a sample heater of  $T_{max} = 650 \text{ }^\circ\text{C}$ , two Aluminum and Magnesium anodes for X-Ray sources, an electron source and a hemispherical electron analyzer (HSA). The deposition rate was determined by several gold deposition/XPS measurement cycles. The amount of deposited gold is precisely controlled by the Knudsen cell's shutter. Along with the three types of substrates mentioned above, another one was used without any oxide layer ( $E_0$ ) obtained by etching  $E_3$  in HF solution just before the introduction in the UHV chamber.

The next section presents the study of the Au deposition on the different types of  $\text{SiO}_2$  surfaces ( $E_0$  to  $E_4$ ). We select the most suitable one and test afterwards the effective thickness  $h_{Au}$  of gold films and the impact of annealing time. It is well known that gold grows epitaxially on silicon substrates surfaces by either Stranski-Krastanov or Volmer-Weber mode [67, 68]. Thus, the term effective thickness is used rather than film thickness to signify the total amount of gold deposited.

## I.2.2 Effect of the $\text{SiO}_2$ film and substrate's temperature $T_s$

The presence of catalyst droplets is required in any VLS process, however their preparation may differ from one growth technique to another. For example, the growth of Au-catalyzed NWs by HVPE is performed under atmospheric pressure inside reactors in which the deposition of gold films is not doable. Therefore, the surface preparation is achieved outside reactors by depositing and dewetting gold films in an UHV chamber. Note that it is possible to deposit gold films in UHV chamber and do the dewetting in an independent growth reactor (HVPE or MOVPE) by heating up the substrates to the NWs growth temperature. On the other hand, for MBE, formation of gold droplets and NWs growth can be achieved subsequently in the same reactor.

Depending on the growth technique, the deposition of gold can be done either at RT before the heating step or directly at the growth temperature ( $\sim 600 \text{ }^\circ\text{C}$  in MBE) right before switching on the growth materials. In order to examine the effect of  $T_s$  on the distribution of gold droplets, we have deposited the equivalent of 1 nm (4 monolayers ML) of gold on all samples ( $E_0$ ,  $E_1$ ,  $E_2$  and  $E_3$ ) at two different  $T_s$ : RT and  $600 \text{ }^\circ\text{C}$ . Subsequently, substrates were cooled down directly after switching off the gold evaporator. SEM images showing the distributions of Au structures are shown in Table I.1. If we focus at the moment on samples  $E_1$ ,  $E_2$  and  $E_3$ , we can see clearly that after deposition at  $T_s = \text{RT}$  the density and size distribution of Au droplets for all samples show very similar configuration (panel b to d in Table I.1). At the same time, the deposition at  $T_s = 600 \text{ }^\circ\text{C}$  enables to discriminate different behaviors of the three samples. The density and the size distribution decrease considerably when increasing the  $\text{SiO}_2$  thickness (panel f to h in Table I.1). Notice that the sticking coefficient

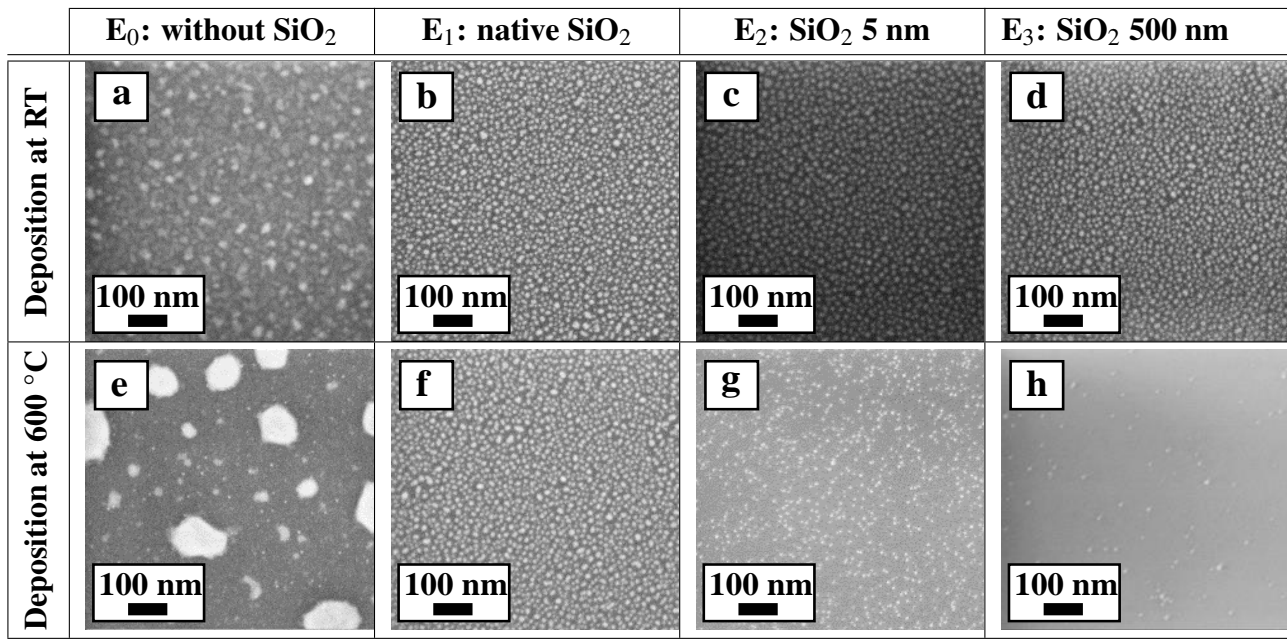


Table I.1: SEM images showing the distribution of as-deposited Au structures after evaporation of 1 nm of gold at RT (upper line) and 600 °C (lower line), on different types of substrates (a)  $E_0$ , (b)  $E_1$ , (c)  $E_2$  and (d)  $E_3$ .

is considered to be unity in the range of temperature studied (beneath 600 °C) [71]. In addition to small droplets, we notice that some big gold clusters were found on the surface of  $E_2$  and  $E_3$  of sizes increasing with the thickness of thermal  $\text{SiO}_2$  (Fig. I.9.a-b). Energy-Dispersive X-Ray Spectroscopy (EDS) measurements show that these clusters are nothing than gold (Fig. I.9.d-f). We should mention also that some regions showing a very high density of droplets were found as well on those samples (Fig. I.9-c).

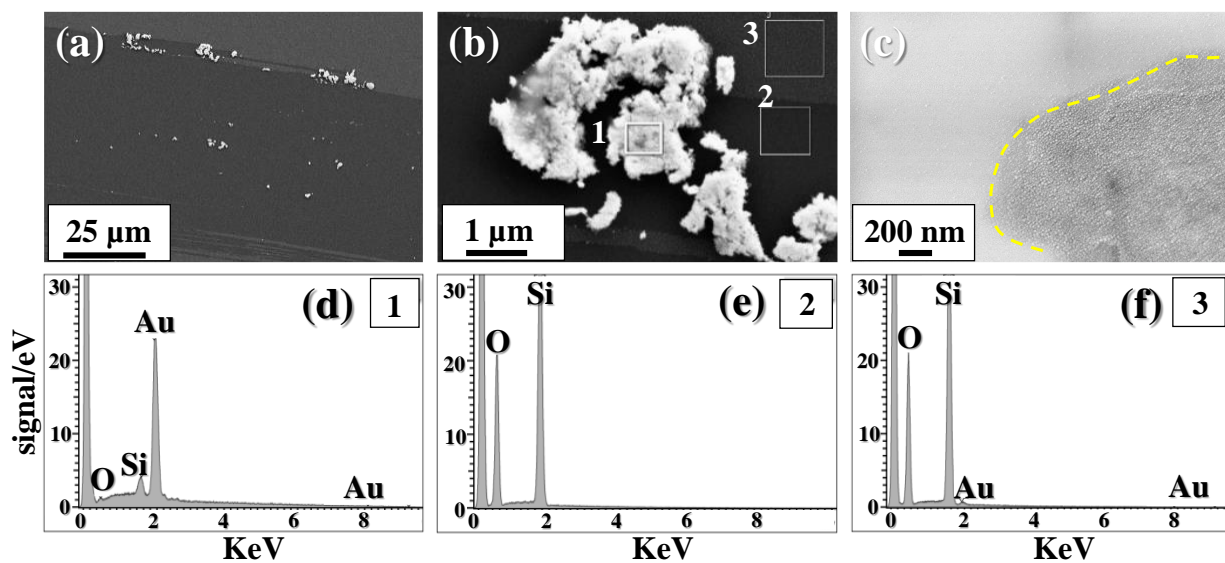


Figure I.9: (a-c) SEM images of  $E_2$  with the corresponding EDS measurements (d-e) of the regions containing clusters in panel (b).

An interpretation of this could be related to the activation energies  $Q_s$  of atoms reported to be three times smaller on thermal thick  $\text{SiO}_2$  [72] than on native  $\text{SiO}_2$  [69]. This change can be attributed to the surface roughness that decreases with thermal oxidation thickness [73]. Therefore, this suggests an increase of the surface diffusion constant given by  $D_s = D_0 \exp(-\frac{Q_s}{k_B T_s})$ , where  $D_0$  is a constant and  $k_B$  is the Boltzmann's constant. Thus, atoms coming on the surface of thick  $\text{SiO}_2$  at high  $T_s$  can diffuse and meet each others easily, forming then the big clusters and regions with high density of droplets as mentioned above. On the other hand, Table I.2 shows that heating samples for 10 minutes after the deposition of 1 nm of gold at RT doesn't have any effect on the distribution and density of the gold droplets. Once formed, the stable droplets are less mobile on the surface because of their high activation energy compared to the atoms [74].

Concerning samples with removed oxide layers ( $E_0$ ), it can be clearly seen that the deposition of 1 nm of gold at RT yields a discontinuous layer (panel a in Table I.1). After annealing, this layer transforms into clusters with irregular shapes (panel a in Table I.2), very similar to those obtained by deposition at 600 °C (panel e in Table I.1). This matches well with the results reported by LeLay et al. [75] who showed that at RT, a texture starts to appear for an equivalent quantity of gold beyond 1 ML. For 20 ML, this texture becomes a 2D layer with mosaic structures. Moreover, Otter et al. [76] claim to have observed by TEM a surface-stabilized Au-Si silicide with the Si substrate, forming at RT a film of two or three atomic layers, whose composition is close to the  $\text{Au}_{81}\text{-Si}_{19}$  eutectic. Under heating, several oriented superstructures appear at different temperatures [77].

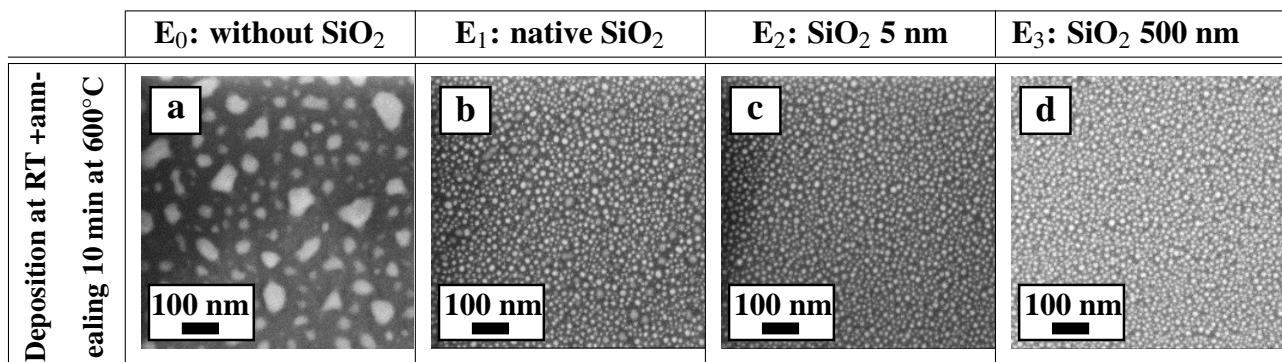


Table I.2: SEM images of (a)  $E_0$ , (b)  $E_1$ , (c)  $E_2$  and (d)  $E_3$ , after deposition of 1 nm of Au at RT and 10 minutes of annealing at 600 °C in UHV chamber.

### I.2.3 Different amounts of gold deposited

Obtaining arrays of NWs with homogeneous diameters and acceptable density requires the same criteria for catalyst droplets. From the results obtained in the previous section, we are able now to select the most two suitable types of substrates for VLS growth to continue our study. Therefore, we have chosen  $E_1$  and  $E_2$  to test the effect of the thickness  $h_{Au}$  of gold films deposited on the surface. Four  $h_{Au}$  (0.2, 0.5, 1 and 2 nm) are deposited at RT, and then undergo an annealing at 600 °C for 10 minutes in the UHV chamber. This annealing step is required since all NWs growth are performed at

$T > 500$  °C. Table I.3 shows the evolution of the grain sizes and their distributions on the surfaces of the substrates ( $E_1$  top line and  $E_2$  bottom line).

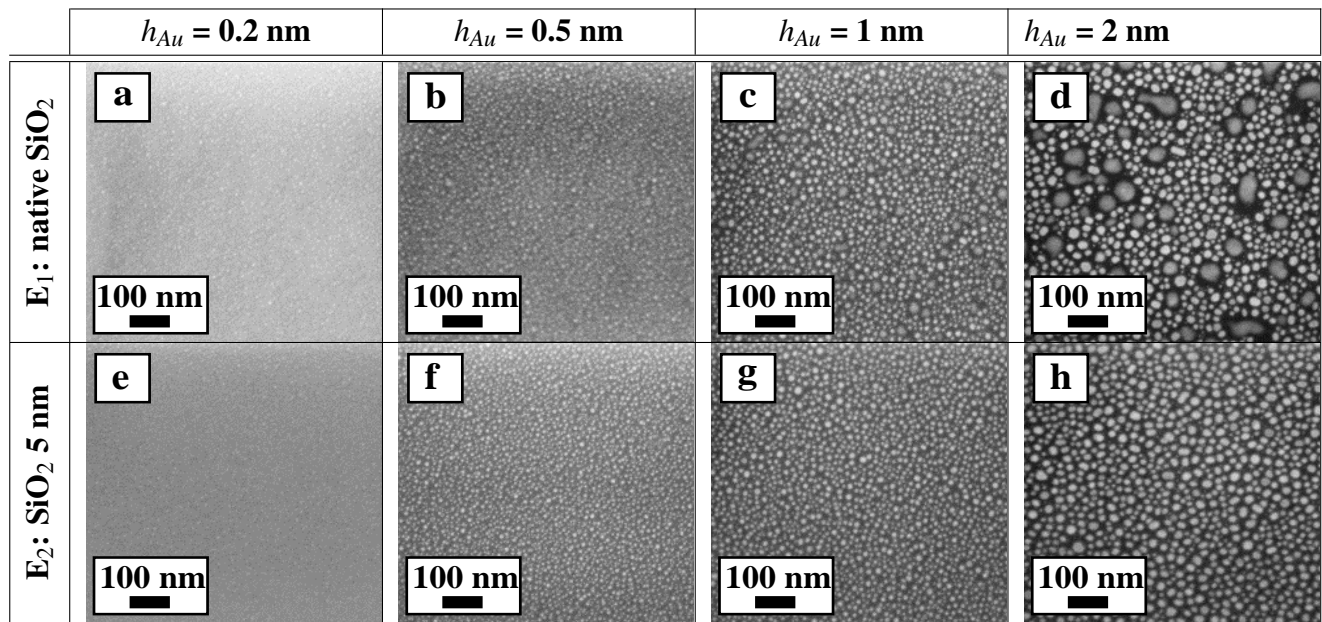


Table I.3: *Distribution of Au droplets after deposition of (a,e) 0.2, (b,f) 0.5, (c,g) 1 and (d,h) 2 nm of gold at RT followed by an annealing at 600 °C for 10 minutes under UHV. The upper images correspond to  $E_1$  (native  $SiO_2$ ) and the lower ones are related to sample  $E_2$  (5 nm of  $SiO_2$ ).*

The first point that stands out from these figures is the increase of the droplets size when increasing  $h_{Au}$ . We should mention that even though we do not see them, small droplets having size beyond the resolution of our SEM may exist, and they grow when increasing the quantity of Au. As they grow, the coalescence starts to take place and bigger droplets appear, decreasing then the density. We believe then that the density has the biggest value at the beginning with very small amount of gold and decreases continuously while increasing  $h_{Au}$ . It is worthy to note also that there is a slight difference between the native and the 5 nm thermal  $SiO_2$  in terms of droplets shapes. In panel d of Table I.3, some droplets start to get irregular forms after the annealing and become very similar to superstructures of  $E_0$  in panel a of Table I.2. This suggests that the Au droplets are transformed into Au-Si alloy, whose origin will be discussed below in section I.2.5.

#### I.2.4 Influence of the annealing time $t_a$

In what follows, we focus our interest on  $E_1$  and we fix  $h_{Au}$  at 1 nm since it gives acceptable size distribution and density. Fig. I.10 shows the evolution of the droplets after deposition at RT and annealing at 600 °C for different  $t_a$  (0, 10, 30, 60 and 180 minutes). It can be clearly seen that the size of droplets increases when increasing  $t_a$ , until the mentioned irregular structures start to appear for  $t_a \geq 1$  h. Due to the low activation energy of surface diffusion, calculated to be 1.4 eV by Jiran and Thompson [69], adsorbed single atoms (called ad-atoms) can diffuse easily on the

surface, especially at high temperatures. These latter can then easily meet each others and form small clusters. Subsequently, these clusters continue to grow by absorbing the surrounding ad-atoms. As we anneal, a considerable redistribution of the droplets occurs, allowing the system to minimize the overall interfacial energy (Fig. I.10 b-e). This can be clearly seen in panel (f) which shows that the as-deposited droplets have a mean diameter of 5 nm with a narrow full width at half maximum (FWHM). Upon annealing, the diameter increases and the distributions become wider. Therefore, the

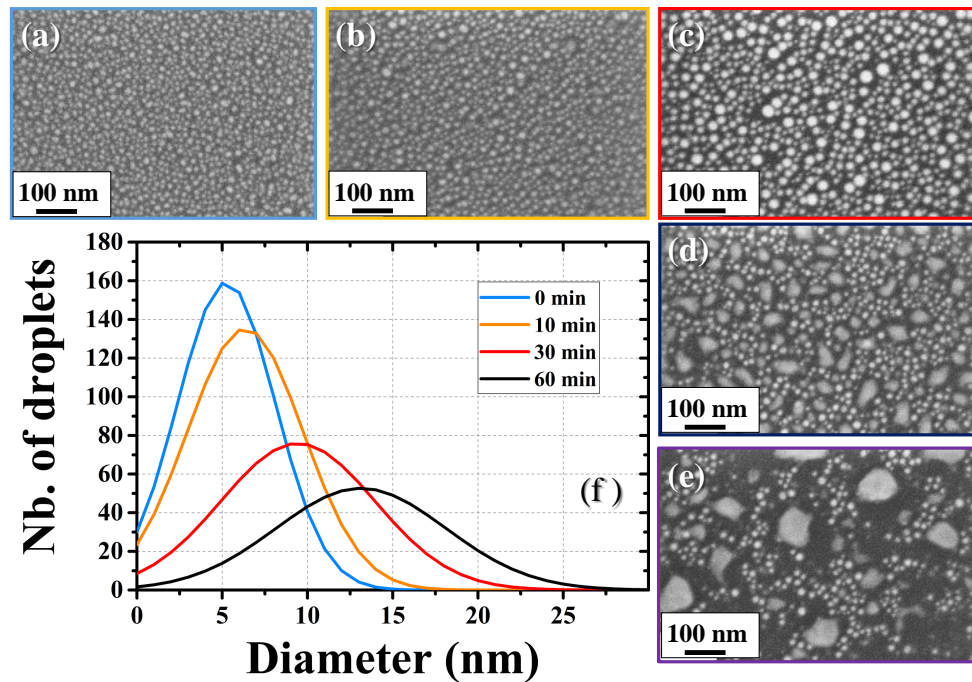


Figure I.10: *Distribution of gold droplets after deposition at RT and annealing at 600 °C of 1 nm of gold film on  $E_1$  for different annealing times  $t_a$ : (a) 0, (b) 10, (c) 30, (d) 60 and (e) 180 minutes. Analyzing these figures gives the Gaussian distributions shown in panel (f).*

large stable droplets grow at the expense of the small ones to lower the total surface to volume ratio of the grains. In the next section we will study in details, using low energy electron microscopy, what happens for longer  $t_a$  and how these clusters evolve.

### I.2.5 Dynamics of Au clusters and decomposition of $\text{SiO}_2$

It has been demonstrated long ago that  $\text{SiO}_2$  decomposes at temperatures above 900 °C according to the reaction [78]:



Some years later, Dallaporta et al. [79] showed experimentally that the presence of metal atoms (including Au) at the interface  $\text{SiO}_2/\text{Si}$  tends to catalyze this reaction, i.e. the decomposition could occur at lower temperatures. In our case, where the Au is supplied by Au droplets deposited on the top surface of the oxide, the decomposition mechanism is expected to take place as follows:

(i) The diffusion of Au atoms present at the surface of the  $\text{SiO}_2$  is thermally activated. These atoms start to migrate through the oxide layer until reaching the  $\text{SiO}_2/\text{Si}$  interface.

(ii) At the interface, the decomposition process is accelerated by the presence of Au atoms. The released  $\text{SiO}_g$  evaporates, leaving behind it voids for Au atoms. When these latest are supplied by a droplet, this process continues until a full decomposition of the oxide layer underneath the droplet, forming then a pinning site.

(iii) The Au droplets localized in these sites start to pump Si atoms from substrate forming a Au-Si alloy that is liquid at  $T > 370$  °C [80, 81].

(iv) More heating helps the droplets to evolve by collecting more Au atoms from surface diffusion and therefore to pump more Si atoms to ensure a stable eutectic composition ( $\text{Au}_{81}\text{Si}_{19}$ ) [76].

Let us now prove experimentally these expectations. To do so, we use an *in-situ* Low Energy Electron Microscopy (LEEM) coupled with a Low Energy Electron Diffraction (LEED). This study is achieved as a part of collaboration with Pr. Frédéric Leroy who gave me the opportunity to do these experiments in his laboratory CINaM - Marseille. The experiments were performed in an UHV chamber equipped with an Elmitec LEEM III microscope described in Ref. [82]. The observations were carried out in bright field mode, with an electron beam energy of 1.8 eV. Sequential images were recorded at a rate of 0.25-10 Hz in sliding average mode. This allows a good compromise between image quality and real-time acquisition. Surface diffraction pattern were taken in LEED mode. As substrates, we used Si(111) B-doped (with resistivity of  $1\text{-}10 \text{ } \Omega\cdot\text{cm}^{-1}$ ),  $500 \text{ } \mu\text{m}$  thick, cut in square shape of  $1\text{ x }1 \text{ cm}^2$ . An effective thickness of 1 nm of Au is deposited at RT and then heated at 700 °C.

Fig. I.11 shows the evolution of the surface under annealing at 700 °C for different  $t_d$ . Notice that the time delay (called  $t_d$ ) before the appearance of the clusters is function of the temperature, and is about 30 minutes at 700 °C. Here, the origin of time  $t_0$  is taken when the clusters become sufficiently large to be observed clearly. The yellow bars represent  $1 \text{ } \mu\text{m}$ . We can see clearly that the droplets increase in size while diffusing on the surface, forming behind them bright regions whose LEED pattern is shown at the right of the figure. The first thing that we should mention is the existence of some spots in the pattern, proving that the amorphous  $\text{SiO}_2$  layer is attacked. The hexagonal symmetry of the pattern is characteristic of the  $\sqrt{3}\text{x}\sqrt{3}$  phase. Notice that the same results have been obtained for lower temperatures ( $\sim 600$  °C), except that much longer  $t_d$  was required, and of course longer  $t_d$ .

In order to support these observations, we made Atomic Force Microscopy (AFM) images on the surface after cooling down the substrate. The results are shown in Fig. I.12. First of all, these figures show that the tracks consist of cavities, confirming the attack of the  $\text{SiO}_2$  layer. The high difference in contrast between these regions and the surrounding substrate suggests that some of the unveiled zones have been attacked as well by the droplets. This is due to the pump (mentioned earlier) of Si atoms from the substrate. At the same time, the flatness of these regions is almost perfect, confirming the mono-phase  $\sqrt{3}\text{x}\sqrt{3}$  structure of the surface. Concerning the droplets, their heights exceed 15 nm and they have irregular shapes. This could be related to the diffusion anisotropy of the droplets due

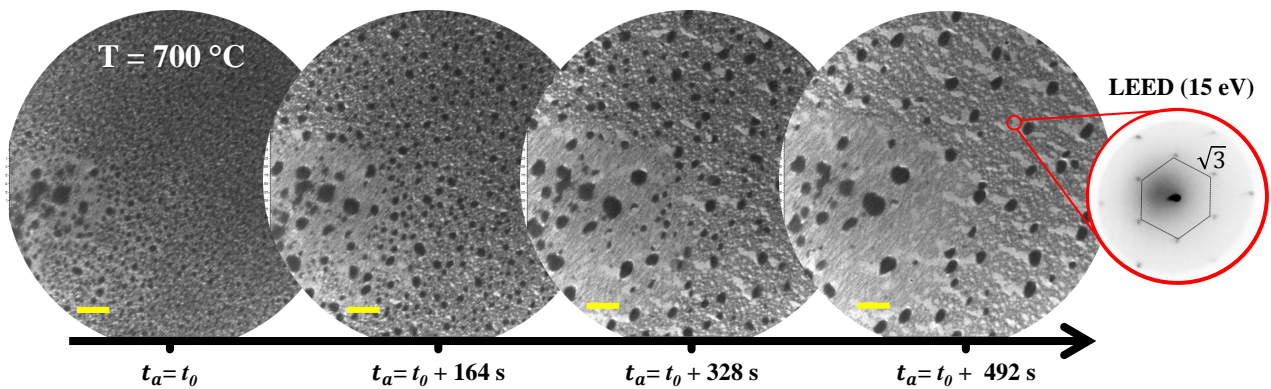


Figure I.11: *LEEM images ( $E = 1.8 \text{ eV}$ ) showing the evolution of the Au-Si clusters diffusing on the surface while decomposing the native  $\text{SiO}_2$  at  $700 \text{ }^\circ\text{C}$ . The effective thickness of Au is  $1 \text{ nm}$ , deposited at RT before annealing. The yellow bar represents  $1 \text{ } \mu\text{m}$ . At the right, a LEED pattern of the trace formed behind the diffusing cluster is shown. The dashed hexagon evidences that the unveiled surface exhibits a  $\sqrt{3} \times \sqrt{3}$  reconstruction.*

to the pinning of the droplets contact line onto some remaining oxide at the surface.

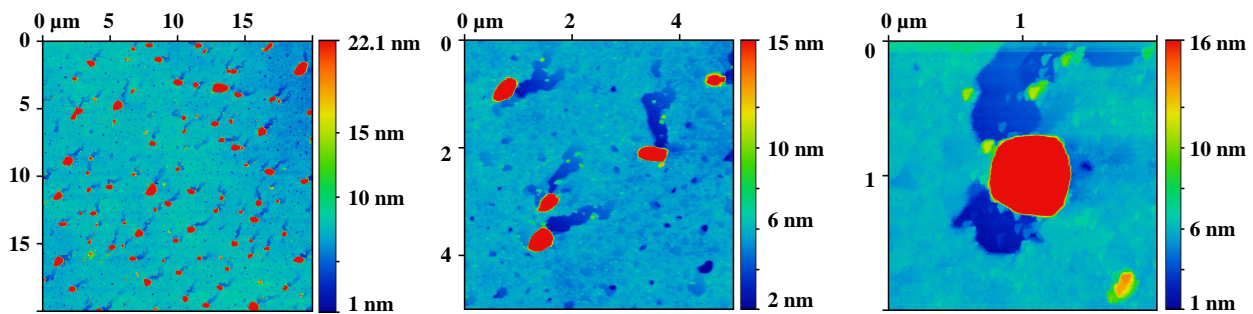


Figure I.12: *AFM images showing the attack of the  $\text{SiO}_2$  layer by lateral diffusion of the Au droplets. The dark blue zones correspond to the unveiled surface of the substrate.*

Let us now transpose all the results obtained in this part to the growth of NWs by the HVPE technique. Remember that the deposition of gold is, unlike MBE, not feasible in the HVPE reactor. So we have to deposit Au under UHV conditions in a separate chamber before growing NWs. For some reasons (shown later in Chapter III), it is of interest to have NWs with small diameters. Therefore, a  $h_{\text{Au}} = 1 \text{ nm}$  deposited at RT and annealed 10 minutes at  $600 \text{ }^\circ\text{C}$  seems to be the good quantity according to the size distribution shown in panel c in Table I.2. On the other hand, a comparison between an annealed sample for 10 minutes in the UHV chamber (at  $600 \text{ }^\circ\text{C}$ ) and the HVPE reactor (at  $700 \text{ }^\circ\text{C}$  under atmospheric pressure) shows that the size distribution is almost the same. Therefore, it is safe to replace the annealing step under UHV by a NWs pre-growth step where the HVPE reactor is heated up to temperature around  $700 \text{ }^\circ\text{C}$ . In addition, a  $t_a$  of 10 minutes is comparable to the time needed to initiate the growth once the temperature is stabilized.

Significantly, the decomposition mechanism of the  $\text{SiO}_2$  is not expected to change for small droplets, although we could not prove it experimentally because of the limited resolution of our LEEM

technique. It is then concluded that **Si atoms are always present in our Au catalyst droplets**. The influence of Si has been proven to be critical for the growth of Au-catalyzed GaAs NWs on Si substrate. It will be at the heart of Chapter II.

In the next section we present the main results obtained for the growth of GaAs NWs by HVPE, on Si substrates prepared according to section I.2

### I.3 Experimental results on the growth of GaAs NWs on Si(111) by HVPE

I mentioned earlier that our group has reported unique results on the growth on GaAs substrates of ultra-long Au-catalyzed GaAs NWs. Exceptional lengths were obtained along with perfect ZB structure over the whole length of the NWs. However, the picture becomes different when the VLS growth of GaAs NWs takes place on silicon substrates, and this is for two main reasons presented in this section. The first one is related to the surface, while the second one concerns the growth process.

Let us first consider the surface energies present in both systems and calculate their change upon the formation of an island during the first step of growth. Fig. I.13 shows the VLS Au-catalyzed growth model in the case of nucleation at the Triple Phase Line (TPL) and inside the liquid droplet, with the surface energies of interest. Considering the TPL nucleation separately, for instance, the formation of a solid GaAs island of height  $h$  from the liquid phase involves a change of the total surface energy as follows [83, 28]:

$$\Delta G_{surf} = [(1-x)\gamma_{SL} + x(\gamma_{SV} - \gamma_{LV}\sin\beta)]ph + \frac{2\gamma_{LV}\sin\beta}{R}(\Omega_S - \Omega_L)i \quad (\text{I.16})$$

with  $i$  is the number of The first term corresponds to the creation of a solid-liquid interface with the surface energy  $(1-x)\gamma_{SL}ph$  and the solid-vapor interface with the surface energy  $xph\gamma_{SV}$ , where  $p$  is the island perimeter,  $x$  is its fraction along the TPL, and  $h$  is the height of a III-V island. The negative term  $-xph\gamma_{LV}\sin\beta$  represents the change of the droplet surface energy due to the elimination of its small part. The second term is the volume dependent term  $\frac{2\gamma_{LV}\sin\beta}{R}(\Omega_S - \Omega_L)i$  which corresponds to the surface energy change due to the difference between the elementary volumes of the island in the liquid ( $\Omega_L$ ) and solid phase ( $\Omega_S$ ), with  $\beta$  being the contact angle of a droplet of radius  $R$  and the substrate. It is called the Gibbs-Thomson term, which is positive when  $\Omega_S > \Omega_L$  and linearly dependent on the number of GaAs pairs forming the island. Note that the same equation can be obtained for the nucleation inside the catalyst droplet by eliminating the terms corresponding to the creation of solid-vapor interface and suppressing a part of liquid-vapor interface. Anyway, the interface energy between the solid island and the substrate is present, which is not supposed to be the same if the growth is performed on GaAs or Si substrate. Subsequently, the energy cost of island formation is different.

At later stages of growth, this difference of interface energy will play an important role in the determination of whether the grown structure is going to grow as NW or a trace. Indeed, for Au-catalyzed NW growth on GaAs substrate, the settlement of solid occurs at the interface between Au and substrate until the formation of a complete monolayer at the interface. Then, further growth adds material to this monolayer and the droplet should adjoin the deposited GaAs to form the NW. Since the substrate and the formed solid are of the same material, another possibility for the droplet is to stay in contact with the substrate and move laterally while depositing GaAs as a trace rather than NW (Fig. I.14). Here, only the kinetics of the droplet diffusion on the substrate determines the grown

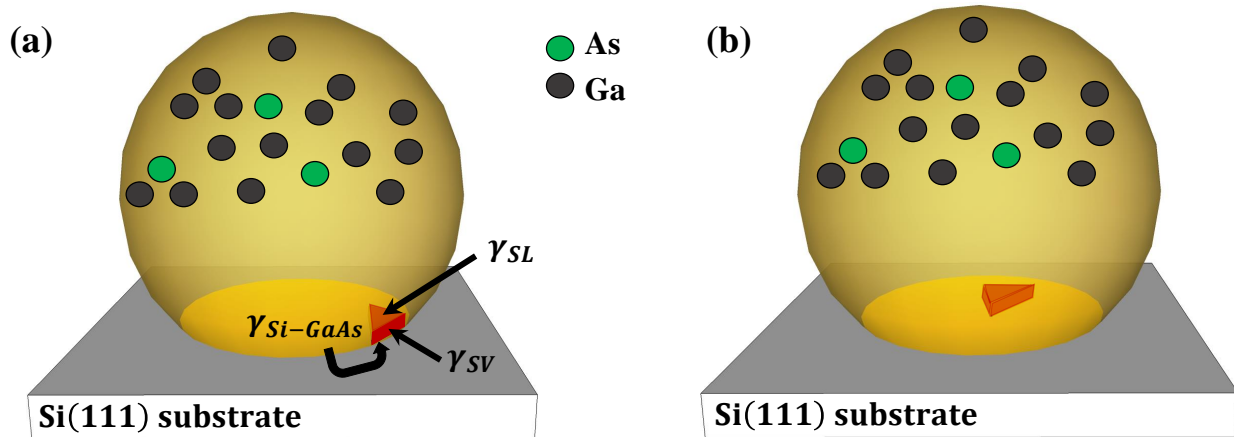


Figure I.13: Schematic representation of the nucleation at the TPL line (a) and inside the Au-catalyst droplet (b).  $\gamma_{SV}$  and  $\gamma_{SL}$  are the Solid-Vapor and Solid-Liquid interface energies, respectively. The GaAs nucleus is represented in red triangle.  $\gamma_{Si-GaAs}$  is the interface energy between the Si(111) substrate and the GaAs solid nucleus.

structures. High mobility leads to a trace formation, whereas low mobility results in NW growth. It is well known that this surface diffusion is strongly favored when the growth temperature  $T_g$  is increased. In our case,  $T_g$  is about 715 °C for GaAs NWs on GaAs substrates, which is considered to be relatively high compared to other techniques. Even though, the presence of NWs and the absence of 2D parasitic layers on Si(111) evidence that the diffusion of the droplet on the surface is not sufficiently activated to form traces [6].

On the other hand, for the growth on bare Si substrates, this phenomenon is found to delay the growth of NWs until a complete 2D GaAs layer is formed on the surface by a pure traces formation stage [84]. In other words, once the whole surface of the substrate is covered by a GaAs buffer layer, NWs start to grow on its top. This is due to the low interface energy between Au and the Si substrate compared to Au and GaAs:  $\gamma_{Au-Si} < \gamma_{Au-GaAs}$ . This notation is not completely true since during the growth the droplet is not only made of Au, it consists actually of an alloy between the Au and the growth materials. It is worth mentioning also that in those experiments, the native oxide layer was removed by Ga polishing before deposition of gold droplets in the MBE chamber.

However, in our case the  $\text{SiO}_2$  layer is always present at the surface of the substrate because HVPE operates at atmospheric pressure. This obviously makes the system more complex due to the roughness and the presence of bonds between oxygen of the  $\text{SiO}_2$  and Au droplet. Another parameter that may add some complexity is the presence of  $\text{H}_2$  in the reactor during growth, whose behavior is not known. In addition, the temperature dependent diffusion coefficient of the catalyst alloy on the native oxide layer is not known. Given that, it is almost impossible to make predictions about the intention of growing as NWs or traces. This is why it seemed important to do some experiments using Si(111) substrates with native oxide and varying the  $T_g$ . The effective thickness of gold deposited ( $h_{Au}$ ) under UHV was fixed at 1 nm (as described earlier), which showed to form droplets with an average diameter of 5 nm. All growth times are fixed at 30 minutes. The III/V ratio is fixed at 4.5, that

corresponds to our standard growth conditions of NWs by HVPE ( $P_{GaCl} = 31$  and  $P_{As_4} = 71$  Pa). For comparison, the same procedure was done on the same type of substrates but after etching the  $SiO_2$  layer by dipping in 1% HF solution for 3 minutes. The obtained SEM images are shown in Table I.4.

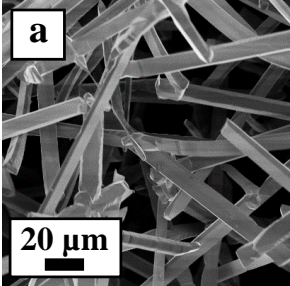
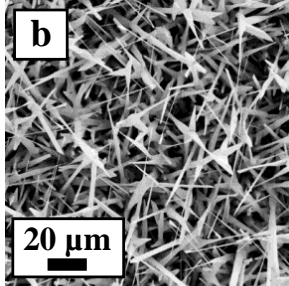
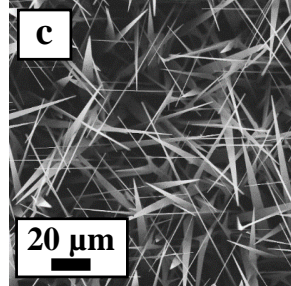
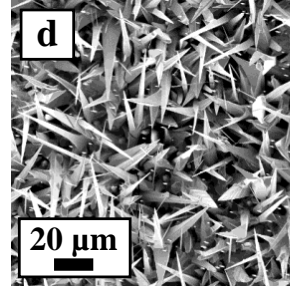
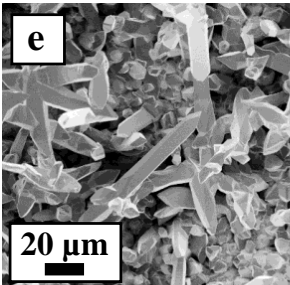
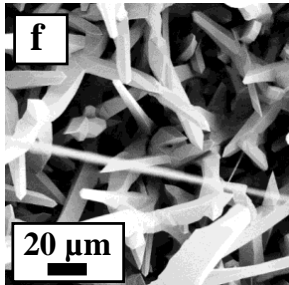
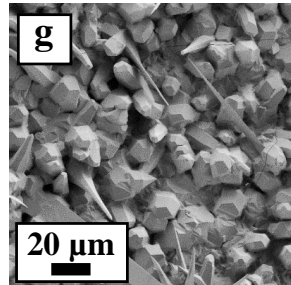
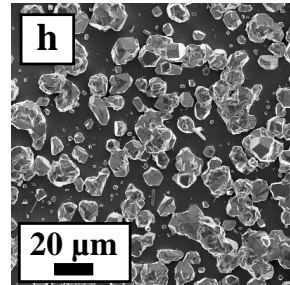
	T = 580 °C	T = 620 °C	T = 715 °C	T = 760 °C
$h_{Au} = 1$ nm, III/V = 4.5, $P_{GaCl} = 31$ Pa, $P_{As_4} = 71$ Pa and $P_{HCl_{add}} = 70$ Pa				
SiO <sub>2</sub> /Si(111) substrate				
Bare Si(111) substrate				

Table I.4: SEM images showing the grown structures at different temperatures on: SiO<sub>2</sub>/Si(111) substrate (upper line) and bare Si(111) substrate (lower line). The growth conditions are mentioned on top of the table.

It can be clearly seen that the growth is better on oxidized than bare Si(111) substrates. This will be the subject of Chapter II where we present a thermodynamic model to explain this behavior. Let us concentrate on the SiO<sub>2</sub>/Si(111) substrates. If we look more precisely at those images (Figs. a-d in Table I.4), the first things that come out are the very high density and the randomness of the structures. In addition, these structures are very tapered with very large bases, except the ones grown at 580 °C (panel a) which exhibit a very large uniform diameters. The sample grown at 715 °C presents the thinnest structures. Therefore, this  $T_g$  is chosen for the coming experiments. The purpose now is to optimize these structures in order to obtain well-ordered NWs with uniform diameters. After many unsuccessful attempts (changing III/V ratio, amount of gold deposited, input masses of growth materials and additional HCl flow), this task appeared to be more difficult than expected. Some of the obtained results are presented in Table I.5. First of all, decreasing the amount of deposited gold almost completely suppresses the growth of small structures. As we can see in Fig. a and b of Table I.5, the size of the grown structures significantly increases while decreasing  $h_{Au}$ . Another parameter that may have an impact on the density of structures is the input mass of growth precursors. Figures (c-f) of I.5 show that, instead of decreasing the density, we obtain a complete suppression of the structures when decreasing the partial pressures of precursors (while keeping constant the III/V ratio).

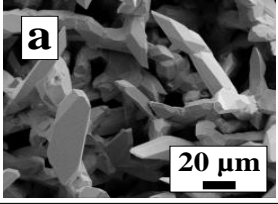
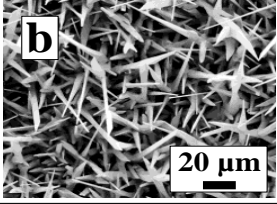
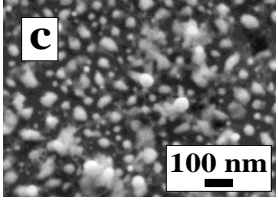
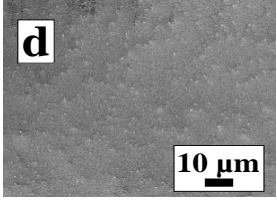
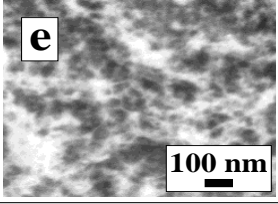
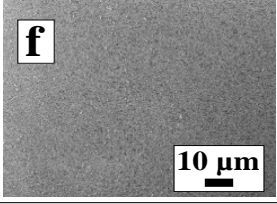
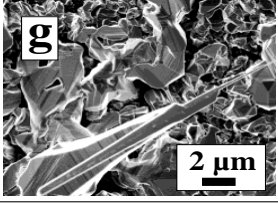
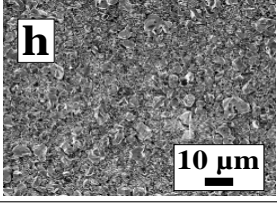
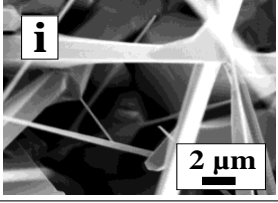
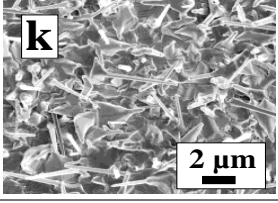
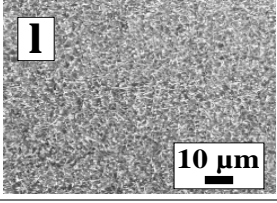
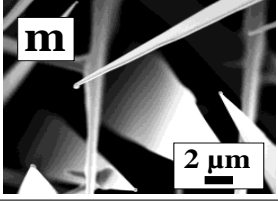
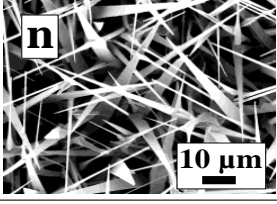
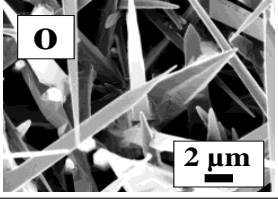
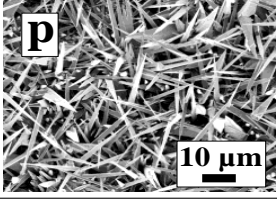
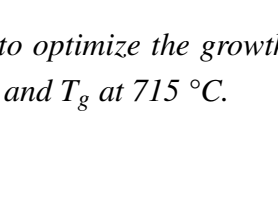
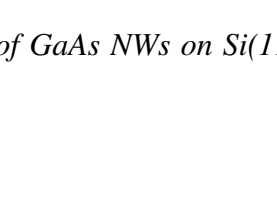
	$P_i$ (atm)		Substrate	III/V	SEM images		
Impact of Au	GaCl	$3.1 \cdot 10^{-4}$	0.2 (a) or 0.5 (b) nm Au /SiO <sub>2</sub> /Si(111)	4.48			
	As <sub>4</sub>	$7.1 \cdot 10^{-4}$					
	HCl <sub>add</sub>	$6.6 \cdot 10^{-4}$					
Impact of input mass	GaCl	$3.2 \cdot 10^{-4}$	1 nm Au/SiO <sub>2</sub> /Si(111)	4.65			
	As <sub>4</sub>	$7.3 \cdot 10^{-5}$					
	HCl <sub>add</sub>	$6.6 \cdot 10^{-4}$					
	GaCl	$9.7 \cdot 10^{-4}$		4.55			
	As <sub>4</sub>	$2.2 \cdot 10^{-4}$					
	HCl <sub>add</sub>	$6.6 \cdot 10^{-4}$					
Impact of III/V ratio	GaCl	$3.2 \cdot 10^{-4}$		1 nm Au/SiO <sub>2</sub> /Si(111)	180		
	As <sub>4</sub>	$1.8 \cdot 10^{-5}$					
	HCl <sub>add</sub>	$6.7 \cdot 10^{-4}$					
	GaCl	$1.6 \cdot 10^{-3}$			3.4		
	As <sub>4</sub>	$4.3 \cdot 10^{-4}$					
	HCl <sub>add</sub>	$6.5 \cdot 10^{-4}$					
	GaCl	$3.2 \cdot 10^{-4}$	2.2				
As <sub>4</sub>	$14 \cdot 10^{-4}$						
HCl <sub>add</sub>	$6.5 \cdot 10^{-5}$						
Impact of HCl <sub>add</sub>	GaCl	$3.3 \cdot 10^{-4}$	1 nm Au/SiO <sub>2</sub> /Si(111)	4.65			
	As <sub>4</sub>	$7.3 \cdot 10^{-5}$					
	HCl <sub>add</sub>	$1.6 \cdot 10^{-3}$					
	GaCl	$3.3 \cdot 10^{-4}$					
	As <sub>4</sub>	$7.3 \cdot 10^{-5}$					
	HCl <sub>add</sub>	$2.9 \cdot 10^{-6}$					

Table I.5: The main experimental results obtained to optimize the growth of GaAs NWs on Si(111) substrates. The growth time was fixed at 30 minutes and  $T_g$  at 715 °C.

Now, let us see what happens when we change the III/V ratio. As shown in Figs. g-l of Table I.5, a high III/V ratio favors the formation of a thick buffer layer, as does a low III/V. Finally, the remaining parameter is the  $\text{HCl}_{add}$  that is known to have a great impact on the equilibrium constant, i.e. the growth process. This is true in the case of 2D epitaxial layers as shown in section I.1.6. However, the experimental results shown in Figs. m-p of Table I.5 suggest that this precursor does not have as high impact in VLS process. The obtained structures are very tapered and their density is still very high upon decreasing or decreasing the partial pressure of  $\text{HCl}_g$ . Despite the great body of experimental work, of which only the "tip of the iceberg" has been presented here, we realized that the problem is not the vapor phase. Other phenomena have to be unveiled in order clarify the issue of the VLS growth of GaAs on Si.

As a first step the density of structures has to be reduced. This can be done by reducing the growth time to few minutes and see what happens during the first stages of growth. Fig. I.14 shows the surface state after 5 minutes of growth. Looking at Fig. I.14-a, we can see the beginning of the formation of growth domains. Each of them is initiated by a nucleation site, which is supposed to be random since the surface is homogeneous and no preferential sites should be present.

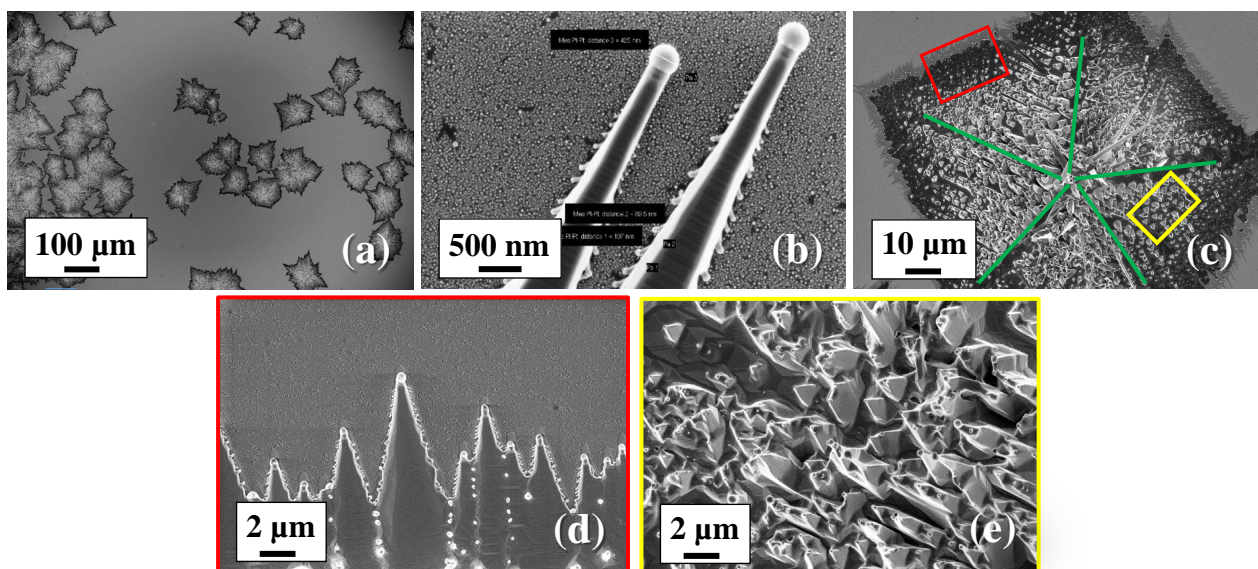


Figure I.14: SEM images after 5 minutes of growth showing the different stages. In panel (a) we can see the beginning of growth domains formation, each of them is initiated by a nucleation site. This latest can be thought as a catalyst droplet that gets saturated before others and starts to deposit materials as 2D buffer layer (b). After coalescence with other layers, there occurs domains limited by green lines as shown in panel (c). The growth of structures in each domain takes place in a defined direction. As shown in panels (d) and (e), these structures are catalyzed by the catalyst droplets stuck between coalescing 2D layers, which after coalescence are pushed upward to the surface.

So what is the origin of these nucleation sites and why do they exist?

Actually, no concrete answer can be given without *in-situ* observation of the first moments of growth, which is not possible in HVPE. However, a logical hypothesis can be formulated using the

SEM images. A nucleation site can be thought as a catalyst droplet that gets saturated before others and starts to deposit materials (Fig. I.14-b). However, it keeps the contact with the substrate and, instead of forming structures, it diffuses on the surface and forms a trace. During this process, the initial droplet gets bigger by collecting other small gold droplets. Simultaneously, other droplets are doing the same and diffuse randomly until all GaAs traces coalesce with each others forming then the so-called growth domain (Fig. I.14-c). Between these traces, the existing gold droplets are pushed upward to the surface of the GaAs 2D layer and start to form the structures (Fig. I.14-d). Fig. I.14-e shows the edge of a growth zone. We can see clearly the gold droplets diffusing and forming the 2D layer, on which the structures start to grow. Of course, longer growth time leads to the expansion of these growth zones and finally their coalescence and the formation of the final state observed earlier after 30 minutes of growth (Fig. c in Table I.4). Here again, the lateral motion is more favorable for the droplets, evidencing that the interface energy between the catalyst alloy and the substrate is lower than with GaAs:  $\gamma_{Au-SiO_2} < \gamma_{Au-GaAs}$ . An obvious solution could be to fix the droplets inside holes by using patterned substrates. However, experimental results on such substrates ( $SiO_2$  mask with holes of 20 nm of diameter) showed that the temperature required to grow NWs is very high, and the diffusion of droplets cannot be limited.

An alternative strategy is to make the nucleation of GaAs easier, so that more solid can be formed before the droplet starts to move laterally. It has been reported that the presence of Ga atoms in the catalyst droplet increases the liquid chemical potential, increasing then the driving force from liquid to solid [85]. This Ga supply can be ensured from the substrate when the growth is performed on GaAs. However, working on Si substrates excludes this possibility. Therefore, we had to add Ga atoms prior to the growth while preparing the catalyst droplets under UHV. We have deposited 1 nm of Ga and covered it with 0.5 nm of Au to avoid the immediate oxidation of Ga during the transfer from UHV chamber to HVPE reactor. The initial surface state of the substrate after deposition of catalyst droplets is very similar to that without Ga (see Fig. c of Table I.3 in section II). The  $T_g$  is the same (715 °C), and the III/V ratio is fixed at 4.5. Indeed, some NWs appear in the SEM images among the tapered structures seen earlier. Actually, in one growth domain we can distinguish two types of structures growing in two different directions (see Fig. I.15).

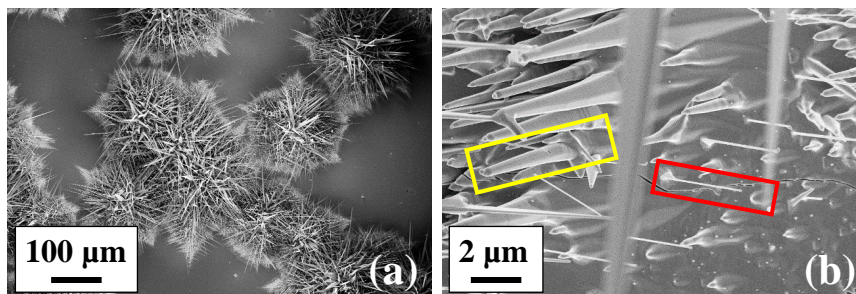


Figure I.15: (a) SEM images showing the final state after 10 minutes of growth of GaAs NWs on Si(111) substrates. The catalyst droplets are made of Ga and Au, deposited in UHV chamber prior to NWs growth in HVPE reactor. (b) A zoom showing the two types of structures obtained in each growth domain: the NWs (in red rectangle) and the scales (in yellow rectangle).

The first corresponds to a pure VLS growth leading to the formation of NWs with uniform diameter all along their length, labeled with a red rectangle in Fig. I.15-b. While the second includes tapered structures (called scales hereafter), which are formed by lateral growth on the side facets of NWs (orange rectangle in Fig. I.15-b). This suggests that the side facets of NWs grown along the second direction are suitable, unlike others, for lateral growth. Unfortunately, adding more Ga does not improve the NWs/scales ratio, or suppress the 2D layer.

Nonetheless, we have obtained at least long NWs that we could study (Chapter III). Moreover, HRTEM images (Fig. I.16) show that these NWs grow along the  $\langle 111 \rangle_B$  direction and are entirely defect free. They exhibit a pure ZB structure with diameters varying from 50 to 200 nm.

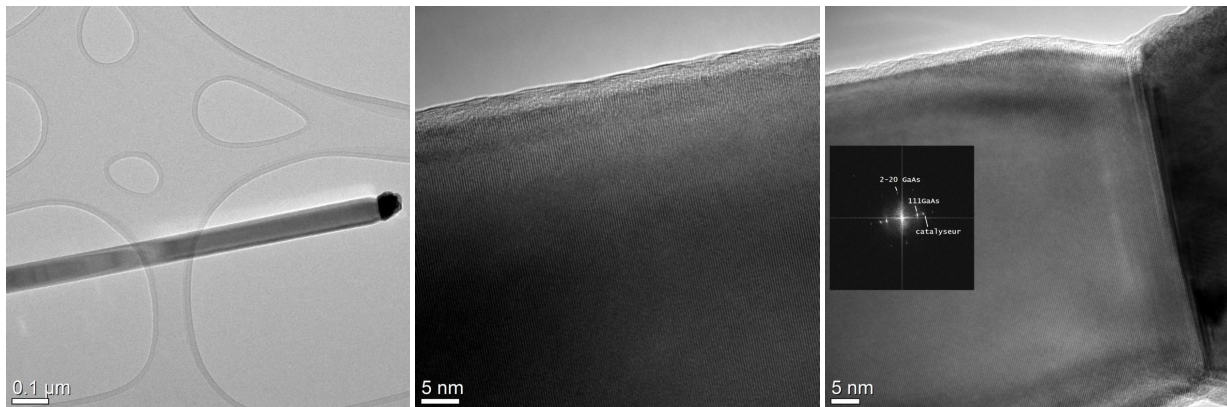


Figure I.16: *HR-TEM* image revealing the uniformity, good crystalline quality and the ZB structure (insert FFT pattern) of GaAs NWs grown by HVPE on Si(111) substrates.

## I.4 Conclusion

The first section of Chapter I introduced my work. We presented the potential of the HVPE technique for the growth of nano-structures, especially GaAs NWs. An overview of the literature on the growth of such structures by other techniques (MBE and MOVPE) was given, allowing for a comparison with the unique results reported by our group.

In the second section, the dewetting of ultra-thin gold films on  $\text{SiO}_2/\text{Si}(111)$  substrate was reported. This study is the first step in my thesis towards the fabrication of NWs. The aim is to better control the distribution of the gold droplets formed after dewetting, which serve as catalyst for NWs growth. We have studied the impact of different parameters on the size distribution and the density of these droplets, such as the thickness of the  $\text{SiO}_2$  layer, the impact of annealing after deposition, the effective thickness of gold film, etc. We have demonstrated that the presence of the  $\text{SiO}_2$  layer is necessary for obtaining regular gold nanodroplets, otherwise silicide clusters of irregular shapes are obtained. On the other hand, we have shown that annealing the substrates at high  $T$  ( $> 600$  °C) for long time produces the same clusters. This is due to the decomposition of the oxide layer in presence of Au, which is studied experimentally *in – situ* in this part.

The last section of this chapter contains the main experimental results obtained for GaAs NWs growth by HVPE. We have demonstrated that, even though ultra-long and defect-free NWs can be obtained on Si substrates, controlling the growth process in HVPE is far from being optimized compared to MBE. We have seen that the main problem does not come from the vapor phase but other issues are also involved. During the growth, the catalyst droplets diffuse on the surface and deposit the GaAs as a buffer layer until covering the whole surface of the substrate. Once the latter is entirely covered, very tapered structures (scales) start to grow on its top, along with a very low density of NWs. So far, we have demonstrated that adding Ga atoms in the catalyst droplets prior to the growth is necessary for increasing the NWs/scales ratio. HRTEM images show that these NWs grow along the  $\langle 111 \rangle_B$  direction and exhibit a pure ZB phase along their entire length.



# Thermodynamics of GaAs nanowires growth in presence of Si

## II.1 Introduction

**I**NTEGRATION of GaAs nanowires (NWs) on silicon substrates has long been assumed as a beneficial step towards realizing high performance devices, and this is for many reasons: the lower-cost, the higher mechanical strength and the higher thermal conductivity of Si substrates compared to GaAs. Such an integration allows to combine the good properties of both materials, which appeared to have a high market potential given its suitability for many applications (e.g. photovoltaic, microwaves devices, photodetectors, etc). However, the lower cost of Si substrates would be offset by some obstacles that have to be overcome in order to obtain optimal devices. We have pointed out in the Chapter I of this manuscript that the surface energies play an important role in the NWs growth. Another difficulty that could be encountered is the presence of some Si atoms in the catalyst droplet coming from the Si substrates by inter-diffusion.

In the first section of the present chapter, we only consider the influence of the silicon concentration in the droplet on the nucleation probability of pure GaAs NWs on different SiO<sub>x</sub>/Si substrates, that is, not allowing for silicon to enter the solid state. The incorporation of Si atoms, i.e. the growth of Si-doped GaAs NWs and ultimately a ternary Si-GaAs solid alloy will be presented in the last part of this chapter.

The work presented in chapter II has been done in collaboration with Pr. Vladimir Dubrovskii from ITMO University, Saint Petersburg, Russia. We acknowledge the Université Clermont Auvergne (UCA) for financial support of his stays in Institut Pascal. I am personally deeply grateful to CPER Région Auvergne for funding my stay in Saint Petersburg in December 2018. We also gratefully thank the research director Frank Glas from C2N for stimulating discussions.

## II.2 Influence of Si on the nucleation rate of GaAs NWs grown on Si substrates.

III-V semiconductor NWs grown by the vapor-liquid-solid (VLS) method [10] are promising for fundamental studies as well as applications in electronic [11], photovoltaic [15], photonic [14], thermoelectric [86], and sensing devices [16]. Each of the growth techniques operates only within a certain temperature domain. For example, gold-catalyzed GaAs NWs on GaAs substrates are grown by MBE at temperatures from 400 to 620 °C [23], while gold-catalyzed HVPE GaAs NWs are grown at temperatures higher than 700 °C [5, 6]. In this wide range of temperatures, the interdiffusion of atoms between the GaAs substrate and the catalyst always serves as an additional supply of gallium and should be favorable for the NW nucleation on GaAs substrates [21, 23, 85].

The picture becomes different when the VLS growth of GaAs NWs takes place on silicon substrates covered/or not with an oxide layer, which is paramount for monolithic integration of III-V photonics with silicon electronic platform. It has been shown that the presence of an oxide layer at the interface between gold and silicon substrate blocks the interexchange between the two materials [80]. Therefore, the interdiffusion of silicon atoms into the gold alloy droplets occurs only after the decomposition of SiO<sub>2</sub> underneath the droplets, which has been long known for temperatures above 400 °C [81], and demonstrated *in-situ* in section I.2 of Chapter I. The Si<sub>(s)</sub> + SiO<sub>2(s)</sub> → 2 SiO<sub>(g)</sub> reaction is enhanced in the presence of gold atoms that reach the SiO<sub>2</sub>/Si interface by thermally activated diffusion into SiO<sub>2</sub> [87, 79]. Obviously, this diffusion is easier through thinner SiO<sub>2</sub> layers. A similar enhancement is anticipated when the VLS growth on silicon is assisted by the gallium droplets [88, 89, 90, 33]. Additionally, the SiO<sub>2</sub> layer can be decomposed at high enough temperatures via the reaction with gallium [91]. A fraction of the gallium droplet is evaporated as Ga<sub>2</sub>O and the remaining part pumps silicon atoms away from the substrate.

Therefore, in both gold-catalyzed and self-assisted VLS growth of GaAs NWs on silicon substrates, the diffusion or re-adsorption of silicon atoms into the droplet prior to nucleation of GaAs NWs is unavoidable. The strength of this effect may vary depending on the deposition conditions and is anticipated to be larger for thinner oxide layers. Also, silicon should diffuse into the catalyst droplets more easily at higher temperatures and in chemical epitaxy techniques where different precursors are able to etch out some silicon from the substrate. Consequently, here we present an approach to quantify how the presence of silicon atoms in the catalyst droplet affects the nucleation rate of GaAs NWs on silicon substrates. We then use this approach to interpret the data on gold-catalyzed HVPE growth of GaAs NWs on silicon. Our model is general as it treats chemical potentials in a quaternary Au-III-V-Si liquid alloy over a wide range of temperatures and irrespective of a particular epitaxy technique employed. Therefore, any VLS III-V NWs grown on silicon with different catalysts (gold, gallium, and indium) may be treated using the proposed scheme.

## II.2.1 Thermodynamic model

We will compare two VLS systems, (I) quaternary Au-Ga-As-Si liquid droplet and (II) ternary Au-Ga-As droplet without silicon, both producing the first monolayer of GaAs NW on a silicon substrate. Assuming that silicon is added to an initially ternary Au-Ga-As droplet at fixed total numbers of gold, gallium, and arsenic atoms  $N_{Au} = const$ ,  $N_{Ga} = const$ , and  $N_{As} = const$  we first compare the atomic concentrations in the droplet before and after adding Si atoms, which are denoted  $c_i$  and  $\check{c}_i$ , respectively, and expressed as:

$$c_i = \frac{N_i}{N_{Au} + N_{Ga} + N_{As}} \quad (\text{II.1a})$$

$$\check{c}_i = \frac{N_i}{N_{Au} + N_{Ga} + N_{As} + N_{Si}} \quad (\text{II.1b})$$

with  $i = \text{Au, Ga, As}$  in the droplet and  $N_{Si}$  is the number of added Si atoms. It is easy to find that in this case  $\check{c}_i \simeq c_i(1 - c_{Si})$  for  $i = \text{Ga, As}$  (and Au), with  $c_{Si} = \frac{N_{Si}}{N_{Au} + N_{Ga} + N_{As} + N_{Si}}$ . We will now consider how adding a given number of silicon atoms changes the chemical potential value of GaAs in the droplet having the initial composition  $c_{Ga}$  and  $c_{As}$ .

In our approach, we consider silicon influencing the initial nucleation step of GaAs NWs. This is supported by the data of Ref. [92], where it has been shown that silicon starts to incorporate into solid NWs after the NW growth is being initiated.

Regular solution model [93, 94, 95, 96] for chemical potentials of gallium and arsenic atoms in a quaternary Ga-As-Au-Si liquid is given by:

$$\begin{aligned} \mu_{Ga} = & \mu_{Ga}^0 + k_B T \ln(c_{Ga}) + \omega_{GaAs} c_{As}^2 + \omega_{GaSi} c_{Si}^2 + \omega_{GaAu} (1 - c_{As} - c_{Ga} - c_{Si})^2 \\ & + (\omega_{GaSi} + \omega_{GaAs} - \omega_{AsSi}) c_{As} c_{Si} + (\omega_{GaSi} + \omega_{GaAu} - \omega_{AuSi}) c_{Si} (1 - c_{As} - c_{Ga} - c_{Si}) \\ & + (\omega_{GaAs} + \omega_{GaAu} - \omega_{AsAu}) c_{As} (1 - c_{As} - c_{Ga} - c_{Si}) \end{aligned} \quad (\text{II.2a})$$

$$\begin{aligned} \mu_{As} = & \mu_{As}^0 + k_B T \ln(c_{As}) + \omega_{GaAs} c_{Ga}^2 + \omega_{AsSi} c_{Si}^2 + \omega_{AsAu} (1 - c_{As} - c_{Ga} - c_{Si})^2 \\ & + (\omega_{AsSi} + \omega_{GaAs} - \omega_{GaSi}) c_{Ga} c_{Si} + (\omega_{AsSi} + \omega_{AsAu} - \omega_{AuSi}) c_{Si} (1 - c_{As} - c_{Ga} - c_{Si}) \\ & + (\omega_{GaAs} + \omega_{AsAu} - \omega_{GaAu}) c_{Ga} (1 - c_{As} - c_{Ga} - c_{Si}) \end{aligned} \quad (\text{II.2b})$$

Here,  $\mu_i^0$  are the reference chemical potentials of atoms  $i$  in pure liquids,  $\omega_{ik}$  are the binary interaction constants between atoms  $i$  and  $k$ ,  $T$  is the absolute temperature and  $k_B$  is the Boltzmann constant. The binary composition-independent interaction constants  $\omega_{ik}$  are tabulated in Table II.1.

We omit the higher order interactions [96, 99] as less essential for our analysis. The chemical potential difference per GaAs pair in the droplet with and without silicon is given by

$$f = \Delta\mu_{Si} - \Delta\mu_0 \quad (\text{II.3})$$

Here  $\Delta\mu_{Si}$  and  $\Delta\mu_0$  are, respectively, the difference of chemical potentials with and without Si atoms in the droplet.

Binary	Interaction Parameter (eV)	Ref.
Ga-As	- 0.2643 - 4.4679 $10^{-5}$ T	[96]
Ga-Si	0.1544 + 5.0785 $10^{-5}$ T	[97]
Ga-Au	0.7445 + 4.3827 $10^{-4}$ T - 4.4452 $10^{-5}$ T ln(T)	[96]
As-Si	- 0.9126 + 5.8147 $10^{-4}$ T	[98]
As-Au	0.1882 - 1.4850 $10^{-4}$ T	[96]
Au-Si	- 0.2473 - 1.6826 $10^{-4}$ T	[99]

Table II.1: Binary interaction parameters used for calculation of Ga and As chemical potentials.

Assuming that the solid state is (almost) pure GaAs without silicon, the same equation is valid for the chemical potential difference per GaAs pair in the droplet with and without silicon and is given by:

$$f = \mu_{Ga}[c_{Ga}(1 - c_{Si}), c_{As}(1 - c_{Si}), c_{Si}] + \mu_{As}[c_{Ga}(1 - c_{Si}), c_{As}(1 - c_{Si}), c_{Si}] - \mu_{Ga}[c_{Ga}, c_{As}, c_{Si} = 0] - \mu_{As}[c_{Ga}, c_{As}, c_{Si} = 0] \quad (\text{II.4})$$

After some calculations (detailed in Appendix A.1), the  $f$  function can be obtained from Eqs. (1) and (2) in the form:

$$f = 2k_B T \ln(1 - c_{Si}) + \eta c_{Si} + \kappa c_{Si}^2 \quad (\text{II.5})$$

The coefficients  $\eta$  and  $\kappa$  are the second order polynomials of  $c_{Ga}$  and  $c_{As}$  given by:

$$\begin{aligned} \eta = & \omega_{GaSi} + \omega_{AsSi} - \omega_{GaAu} - \omega_{AsAu} - 2\omega_{AuSi} \\ & + (5\omega_{GaAu} + \omega_{AsAu} + 2\omega_{AuSi} - 2\omega_{GaSi} - \omega_{GaAs})c_{Ga} \\ & + (5\omega_{AsAu} + \omega_{GaAu} + 2\omega_{AuSi} - 2\omega_{AsSi} - \omega_{GaAs})c_{As} \\ & + 4(\omega_{GaAs} - \omega_{GaAu} - \omega_{AsAu})c_{Ga}c_{As} - 4\omega_{GaAu}c_{Ga}^2 - 4\omega_{AsAu}c_{As}^2 \end{aligned} \quad (\text{II.6a})$$

$$\begin{aligned} \kappa = & 2\omega_{AuSi} + 2(\omega_{GaSi} - \omega_{GaAu} - \omega_{AuSi})c_{Ga} + 2(\omega_{AsSi} - \omega_{AsAu} - \omega_{AuSi})c_{As} \\ & + 2(\omega_{GaAu} + \omega_{AsAu} - \omega_{GaAs})c_{Ga}c_{As} + 2\omega_{GaAu}c_{Ga}^2 + 2\omega_{AsAu}c_{As}^2 \end{aligned} \quad (\text{II.6b})$$

For small enough  $c_{Si}$ , we can expand the logarithmic function in Eq. II.2a, yielding :

$$f \cong \bar{A}c_{Si} + \bar{B}c_{Si}^2 \quad (\text{II.7})$$

with  $\bar{A} = \eta - 2k_B T$  and  $\bar{B} = \kappa - k_B T$ .

The composition-independent interaction constants  $\omega_{ik}$  used here are different from Ref. [93] where they were taken inversely proportional to the sum  $V_i c_i + V_k c_k$  according to Ref. [100], with  $V$  as the elementary volume of the corresponding element in liquid. For the composition-independent interaction constant, the  $f$  function is approximately parabolic and its sign at small  $c_{Si}$  is determined

by the sign of  $\bar{A}$ . Negative  $\bar{A}$  corresponds to lower chemical potentials and hence more difficult nucleation of GaAs NWs from the droplets with silicon. Note that both  $\bar{A}$  and  $\bar{B}$  depend on the droplet composition, most importantly, the gallium content  $c_{Ga}$ , so the nucleation probabilities of GaAs NWs on silicon should be highly sensitive to whether the alloy is gold or gallium-rich.

According to Ref. [101], the nucleation probability for each NW monolayer in the mononuclear vapor-liquid-solid growth, including the very first GaAs monolayer on the substrate, is given by  $p = \pi R^2 J$ , with  $R$  as the droplet base radius and  $J$  the Zeldovich nucleation rate given by:

$$J = \frac{3^{3/4}}{\sqrt{\pi}} D_{As} c_{As} \left( \frac{h}{\Omega} \right)^2 e^{\bar{\mu}_{GaAs} \Delta \bar{\mu}} \exp \left( a - \frac{a^2}{4 \Delta \bar{\mu}} \right) \quad (\text{II.8})$$

Here,  $D_{As}$  is the diffusion coefficient of As in liquid,  $h = 0.326$  nm in the monolayer height of GaAs,  $\Omega = 0.0452$  nm<sup>3</sup> is its elementary volume in solid,  $\bar{\mu}$  denotes chemical potentials in the units of  $k_B T$  and:

$$a = 2 \times 3^{3/4} \frac{\gamma}{k_B T} (\Omega h)^{1/2} \quad (\text{II.9})$$

is the energetic constant related to the effective surface (or edge) energy  $\gamma$  of two-dimensional island with regular triangle shape. At  $T = 715$  °C, this constant equals  $40.5 \times \gamma$  if  $\gamma$  is measured in J/m<sup>2</sup> and therefore the  $a^2/4$  value under the exponent of the Zeldovich nucleation rate is very large, typically on the order of several tens [102].

Analyzing Eqs. II.8 and II.9, it is reasonable to assume that the island surface energy remains the same at low enough silicon concentrations in the droplet. This is also supported by the fact that gallium is the lowest surface energy element among the droplet constituents and hence should segregate at the droplet surface. In this case, the most important part of the ratio between the nucleation probabilities of GaAs from the droplets with ( $p_{Si}$ ) and without silicon ( $p_0$ ) is given by an extremely steep exponential term  $\exp \left( \frac{a^2}{4 \Delta \bar{\mu}} \right)$ , while all the unknown terms cancel in the ratio. Therefore, we can write:

$$\alpha = \frac{p_{Si}}{p_0} = \exp \left( \frac{a^2}{4 \Delta \bar{\mu}_0 \Delta \bar{\mu}_{Si}} \frac{f}{k_B T} \right) \quad (\text{II.10})$$

where  $f$  is the chemical potential difference defined in Eq. II.3. This can be further simplified to:

$$\alpha \cong \frac{p_{Si}}{p_0} = \exp \left( i_c \frac{f}{k_B T} \right) \quad (\text{II.11})$$

with

$$i_c = \frac{a^2}{4 \Delta \bar{\mu}_0^2} \quad (\text{II.12})$$

as the critical size of classical nucleation theory [101] for the droplet without silicon.

Here, we account only for the differences in the chemical potential values by adding silicon to the liquid droplet. It should be noted that dissolving more silicon also increases the contact angle of the droplet resting on the substrate surface. This effect may additionally decrease the nucleation rate and ultimately suppress the NW growth according to Ref. [88].

## II.2.2 Results and discussion

Figure II.1-a shows the evolution of  $f$  as a function of  $c_{Si}$  for the lowest and highest growth temperatures of GaAs NWs, 450 °C (for MOVPE and MBE) and 715 °C (as in our HVPE growth experiments) and different  $c_{Ga}$  ranging from 0.5 to 0.99. The curves reveal that the chemical potential difference  $f$  in the droplets with and without silicon depends drastically on  $c_{Si}$  for all  $c_{Ga}$  in the entire range of temperatures. Although the temperature domain is very wide, the curves at 450 °C and 715 °C are not so different and follow the same trends. For gallium-rich droplets with  $c_{Ga} \geq 0.6$ , the chemical potential in the droplets with silicon is lower than without it for low enough  $c_{Si}$  ( $f < 0$ ), with the difference becoming larger toward higher  $c_{Ga}$ . Therefore, adding silicon to gallium-rich Au-Ga droplets makes the initial nucleation of GaAs NWs more difficult, and this effect is stronger for more gallium-rich droplets. The limiting case of gallium-assisted VLS growth ( $c_{Ga} \rightarrow 1$ ) is the most sensitive to the presence of silicon even for its very small fractions in the droplet. The chemical potential difference becomes positive after exceeding a certain critical  $c_{Si}$ , which depends upon  $c_{Ga}$ .

This critical silicon concentration is greater than 0.35 for  $c_{Ga}=0.99$  and about 0.1 for  $c_{Ga}=0.6$  at any temperature. For gold-rich droplets ( $c_{Ga} < 0.6$ ), the chemical potential difference in systems with and without silicon becomes monotonically increasing with  $c_{Si}$ , meaning that adding any amount of silicon to such droplets only helps to nucleate GaAs NWs. Figure II.1-b shows the dependence of  $f$  on  $c_{Si}$  for different  $c_{Ga}$  and  $c_{As}$  at a fixed temperature of 715 °C. As expected, the curves are not very sensitive to  $c_{As}$  (in the plausible range between 0.005 and 0.06) due to the smallness of the interaction terms with arsenic.

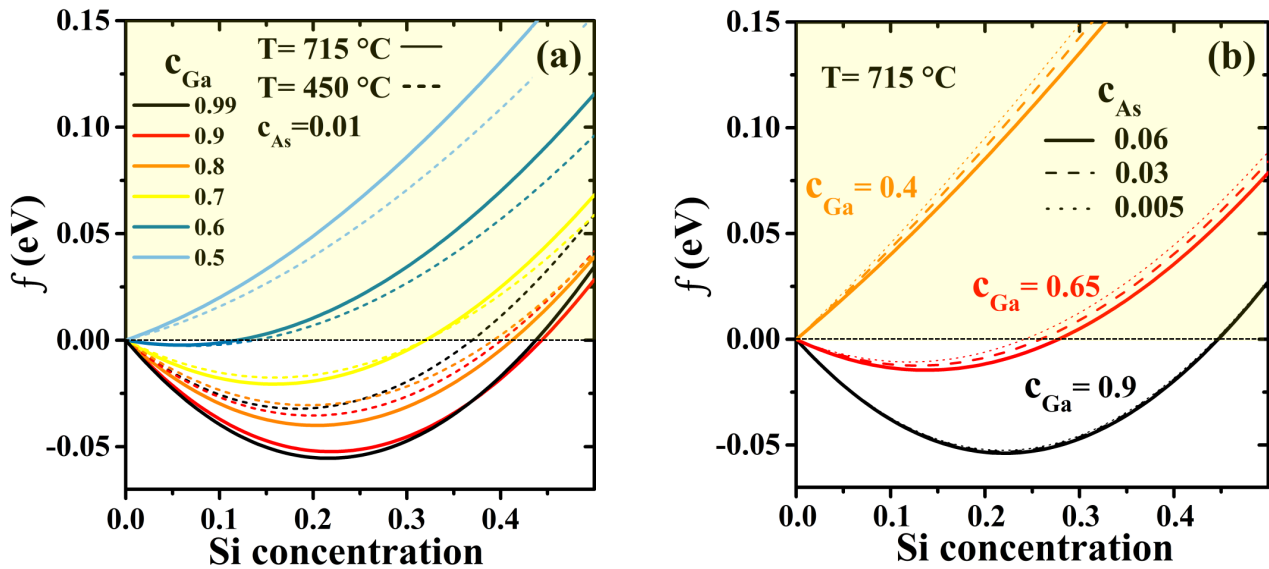


Figure II.1: The chemical potential difference per Ga-As pair in quaternary Au-Ga-As-Si liquid alloy versus ternary Au-Ga-As alloy as a function of the silicon concentration  $c_{Si}$  for (a) different  $c_{Ga}$  from 0.5 to 0.99, with the arsenic concentration  $c_{As}$  fixed at 0.01, at  $T = 450$  °C (dashed lines) and 715 °C (solid lines), and (b) different  $c_{Ga}$  and  $c_{As}$  at  $T = 715$  °C.

We now consider our experimental data on the gold-catalyzed HVPE GaAs NWs grown at 715

$^{\circ}\text{C}$  on Si(111) substrates using the above model. Figure II.2 depicts the typical behavior when the silicon surface is covered with 500 nm of thermal  $\text{SiO}_2$  layer (S1) or with a native  $\text{SiO}_2$  (S2) (Figure II.2-a and II.2-b, respectively). We observe the simultaneous formation of almost cylindrical NWs and pyramidal-like “scales”, while we can only see fewer but larger scales and some parasitic islands on the bare Si(111) after HF etching of the oxide layer (S3) (Figures II.2-c). According to the analysis of Ref. [6], pure zincblende crystal structures of HVPE GaAs NWs requires gallium-rich Au-Ga-Si droplets, with  $c_{\text{Ga}}$  definitely higher than 0.65.

According to Figures II.1-a, such droplets should produce fewer GaAs NWs for larger silicon concentrations. As mentioned above, more silicon should arrive to the droplets resting on the bare Si(111) substrates than on Si(111) covered by an oxide layer, because the latter suppresses the silicon etching. Ignoring the influence of highly volatile arsenic, the data of Refs. [103, 104] give a silicon solubility of about 0.3 in liquid gold and 0.05 in liquid gallium. Therefore, for any Au-Ga alloy, we should not anticipate to have more than 0.3 of silicon dissolved in the droplets.

Looking again at the curves of Figure II.1-b, the condition  $c_{\text{Si}} < 0.3$  at  $c_{\text{Ga}} > 0.65$  guarantees that the presence of silicon suppresses nucleation of GaAs NWs on Si(111), while they perfectly grow under the same conditions on GaAs substrates [6]. Therefore, our model is very well consistent with the experimental observations Fig. II.2.

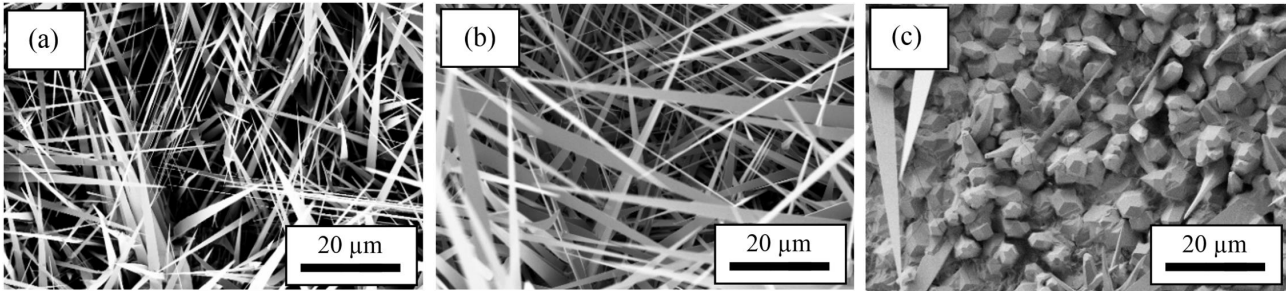


Figure II.2: *Scanning electron microscopy (SEM) images of GaAs structures grown at 715  $^{\circ}\text{C}$  after depositing 1 nm of gold on Si(111) (a) with 500 nm of thermal  $\text{SiO}_2$ , (b) native  $\text{SiO}_2$  and (c) without  $\text{SiO}_2$ . These images were taken in InLens mode with an electronic incident energy of 3 KV.*

More quantitatively, Figure II.3 shows high resolution transmission electron microscopy (HRTEM) images and the corresponding energy dispersive spectroscopy (EDS) compositional data given in Table II.2 for the catalyst droplets of GaAs structures grown on S1, S2, and S3 substrates at 715  $^{\circ}\text{C}$  and under otherwise identical conditions. Of course, the EDS data are obtained for the droplets after growth, which have lost some of their gallium atoms in the cooling down stage under the arsenic flux. This process leads to a droplet shrinking and the corresponding diminishing of the NW top radius [90]. Assuming that the number of gold and silicon atoms present in the droplet during growth remains the same after growth, we can roughly estimate the  $c_{\text{Si}}$  and  $c_{\text{Ga}}$  from geometry by comparing the initial volume of the droplet with gallium and its final volume without gallium with the measured initial and final radii of the NW top (see Figure II.3-d). The detail of this calculation is given in Appendix A.2. These estimates yield the values of silicon concentrations given in Table II.2. In terms of

$c_{Ga}$ , the calculations show the values close to 0.95 for all samples (we reiterate that the influence of arsenic on the shapes of the chemical potential curves is weak according to Figure II.1-b).

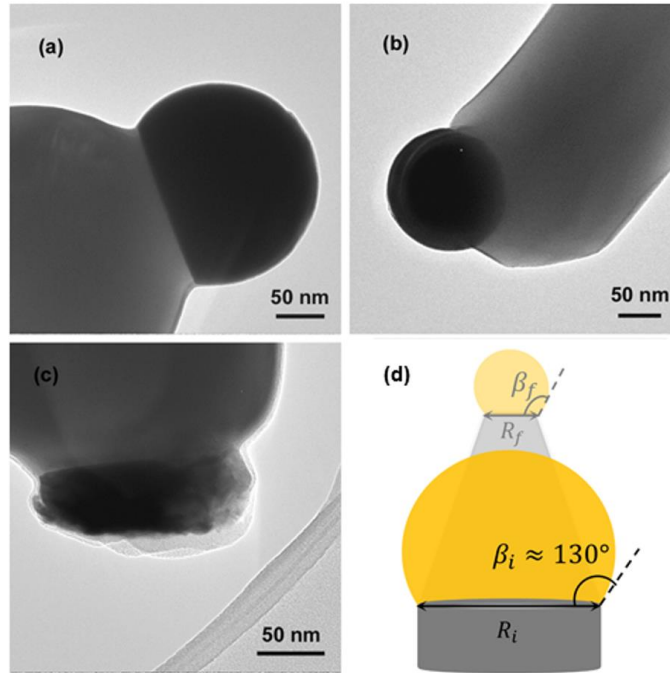


Figure II.3: HRTEM images of the gold-catalyzed GaAs structures with droplets on top, grown at 715 °C on different substrates -(a) S1, (b) S2, and (c) S3. The technique used to estimate the concentrations of gallium and silicon during growth is represented schematically in (d), with  $\beta_i = 130^\circ$  and  $\beta_f = 95^\circ$  reported in Ref. [90].

Sample	$c_{Si}$ after growth	$c_{Si}$ during growth	$c_{Ga}$ during growth
S1	0.02	0.001	0.95
S2	0.05	0.003	0.946
S3	0.21	0.031	0.937

Table II.2: EDS compositional data for the silicon concentrations in the droplets catalyzing GaAs structures on S1, S2 and S3 substrates after growth, with the corresponding estimations of  $c_{Si}$  during growth.

Assuming that the critical size  $i_c$  in Eq. (9) equals six GaAs pairs, and using the chemical potential curve at a fixed  $c_{Ga}$  of 0.95, the surface energy  $\gamma$  equals 0.178 J/m<sup>2</sup> (corresponding to  $a = 7.21$ ). This is close to the estimates of Refs. [33] and [105] for purely gallium-assisted and gold-catalyzed growths of GaAs NWs, respectively. With this surface energy, the ratio of nucleation probabilities for GaAs NWs emerging from the droplets with and without silicon is plotted in Figure II.4 and gives the excellent quantitative correlation with the data. Indeed, we can see that adding a small amount of silicon to the droplets (0.001 and 0.003 in samples S1 and S2) does not have any significant impact on the nucleation probability ( $\alpha \cong 1$ ). On the other hand, the nucleation probability decreases by three times when the silicon concentration is increased to  $\sim 0.03$ , as in sample S3.

Therefore, the droplets on the bare Si(111) do not produce any NWs and instead inflate with the arriving gallium, which makes the NW nucleation even less probable. This explains why almost no regular NWs are seen in sample S3, but only large scales catalyzed by the swelling droplets.

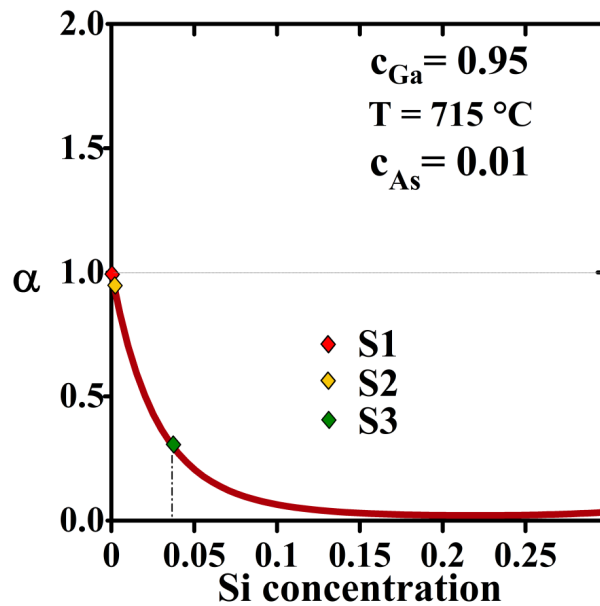


Figure II.4: Ratio of nucleation probabilities of GaAs structures at 715 °C with and without silicon at a fixed  $c_{Ga}$  of 0.95 and  $c_{As}$  of 0.01. The labels show the positions of the three samples (S1, S2 and S3) on the curve corresponding to their  $c_{Si}$  during growth estimated in Table II.2.

The obtained results call for a more general discussion. It is well known that gallium-assisted growth of GaAs NWs on silicon is extremely difficult to achieve in chemical epitaxy techniques such as MOVPE and HVPE. For example, our own results [48] reveal some gallium-catalyzed HVPE GaAs NWs on silicon, but with very low density, which should be due to difficult nucleation in the presence of silicon according to our Figure II.1. Similar difficulties have been described for gallium-assisted GaAs NWs on silicon in MOVPE technique [106, 107], where the rate of silicon etching from the substrate under the gallium droplets is enhanced by the presence of Trimethylgallium. On the other hand, much less etching should be present during MBE, which is why the silicon concentration is lower and gallium-catalyzed GaAs NWs can easily be grown on silicon by this technique [88, 89, 90]. The results presented in this section reveal that having more gold in the droplets helps to nucleate GaAs NWs on silicon. This property has been long known for MOVPE (see, for example, Ref. [108, 109]).

Very high concentration of silicon dissolved in either pure gallium droplet or an Au-Ga alloy may lead to the formation of ternary GaAsSi or even pure silicon NWs. We have observed such NWs in some samples grown on the bare Si(111). This requires a generalization of the model to enable silicon crystallization in the solid state.

## II.3 Si doping of vapor-liquid-solid GaAs NWs: n-type or p-type?

After showing how nucleation of GaAs NWs is affected by the presence of Si in the catalyst droplet, let us now consider that those Si atoms participate to the NWs growth as dopants. It is clear that the doping concentration is not determined in the nucleation stage, because the critical island consists of only a few III-V pairs [102] and contains no Si atoms. Therefore, the nucleation model for ternary VLS-grown NWs cannot be used for doping.

III-V NWs and hetero-structures based on such NWs show great promise for applications in various optoelectronic devices [110, 12, 111, 15], which can be integrated with a silicon electronic platform [110, 12]. However, this requires a controllable methodology for n-type and p-type doping. Consequently, significant efforts have been put into the investigation of the NW doping process (see, for example, Ref. [112] for a review). In the VLS growth, dopants can be incorporated either through the catalyst droplet or via the vapor-solid (VS) mechanism at the NW sidewalls. In the case of Si, for expected standard n-type doping of planar GaAs layers in MBE [113], VS incorporation gives n-type doping, while the VLS mechanism usually leads to p-type doping [13, 92]. As a result, n-type Si doping of GaAs NWs in MBE is the exception [114], rather than the rule. P-type Si doping via the VLS mechanism has been observed in both Au-catalyzed [115] and self-catalyzed [116, 13, 117, 92] MBE-grown GaAs NWs. In the case of MOVPE, the typical temperatures for growing Au-catalyzed GaAs NWs can be insufficient for cracking the Si precursors [118]. In many cases, these difficulties with n-doping limit the use of VLS-grown GaAs NWs and GaAs-based NW hetero-structures in electronic and optoelectronic devices, unless Si is replaced by a better n-dopant, such as Sn [118, 119] or a group VI element (Te or Se) [120, 121, 122]. Of course, another possibility is using the catalyst-free selective area epitaxy method, where n-type doping of GaAs NWs with Si is easily achieved [123].

As with other group IV elements, Si is known for amphoteric behavior [124, 114, 116, 13, 117, 92, 112, 113, 123, 125, 126], meaning that it can either replace group V atoms (anions) to become an acceptor, or be incorporated into cation sites of group III atoms to become a donor. This property has previously been used to change the doping of GaAs layers from n-type to p-type in liquid phase epitaxy [125] and MBE [126] by tuning the growth conditions. In the case of MBE, p-doping is achieved by lowering the As/Ga ratio and increasing the growth temperature [126]. Predominantly p-type doping of VLS GaAs NWs with Si, leads us to suggest a definite mechanism for increasing the probability of replacing As atoms by Si, which is usually absent from the VS growth. First-principles density-functional theory (DFT) calculations using pseudopotentials (see [127] and a discussion therein) have considered some specific features of GaAs NWs that can lead to p-doping. In particular, donors have been shown to preferentially segregate to surface dangling-bond sites and act as deep impurities, rather than shallow donors, thus hindering n-type conductivity. On the other hand, the kinetics of Si incorporation should play an even more important role according to the results given in Refs. [116, 13, 117, 92].

Leaving aside the n-type VS doping, here we present a thermodynamic model for the VLS-

type doping of GaAs NWs with Si, which shows the important role of the As concentration in the droplet. Increasing the As concentration always favors n-type doping. Furthermore, we prove that n-type Si doping occurs in Au-catalyzed GaAs NWs grown under the extreme conditions of HVPE. As shown in Chapter I, this process corresponds to very large material inputs, rapid growth rates and high As-concentrations in the droplet. To our knowledge, this is the first attempt to quantify the strongly amphoteric behavior of Si in VLS III-V NWs as a function of the droplet composition and temperature. This approach provides a simple way to tune the Si doping and even switch it from p-type to n-type if required.

### II.3.1 Thermodynamic model

In the following, we use the notation  $x$  and  $y$  for the atom-fractions of Si atoms replacing Ga and As atoms in solid GaAs, respectively. Replacing Ga with Si atoms creates As-Si pairs and results in n-type doping, while replacing As with Si atoms creates Ga-Si pairs and results in p-type doping. The replaced Ga or As atoms are dissolved in the liquid droplet. A simplified scheme of the doping process is illustrated in Figure II.5.

Considering the VLS growth of GaAs:Si NWs from a quaternary Au-Ga-As-Si liquid alloy, we study the Si incorporation from liquid to solid under equilibrium conditions for all species containing Si. Such an approach has recently been justified for the compositional modeling of ternary III-V NWs [128] and is expected to be even more relevant for doping due to extremely low Si concentrations in both liquid and solid phases. At equilibrium, chemical potentials of both As-Si and Ga-Si pairs in the liquid (L) and solid (S) states must equal each other:

$$\mu_{AsSi}^S = \mu_{As}^L + \mu_{Si}^L, \quad (\text{II.13a})$$

$$\mu_{GaSi}^S = \mu_{Ga}^L + \mu_{Si}^L. \quad (\text{II.13b})$$

However, we do not assume thermodynamic equilibrium for GaAs.

As  $x$  and  $y$  are much smaller than 1, we can write the chemical potentials of both pairs in this solid, using the perfect alloy approximation, that is:

$$\mu_{AsSi}^S = \mu_{AsSi}^P + k_B T \ln(x), \quad (\text{II.14a})$$

$$\mu_{GaSi}^S = \mu_{GaSi}^P + k_B T \ln(y). \quad (\text{II.14b})$$

Here,  $T$  is the absolute temperature,  $k_B$  is the Boltzmann constant and  $\mu_{AsSi}^P$ ,  $\mu_{GaSi}^P$  are the unknown chemical potentials of pure AsSi and GaSi solids (which do not exist). To circumvent this unknown, we choose the reference solid state to be pure GaAs (i.e. chemical potential  $\mu_{GaAs}^P$ ) by presenting the solid chemical potentials of As-Si and Ga-Si in the form:

$$\mu_{AsSi}^S = \mu_{GaAs}^P + \mu_{AsSi}^P - \mu_{GaAs}^P + k_B T \ln(x), \quad (\text{II.15a})$$

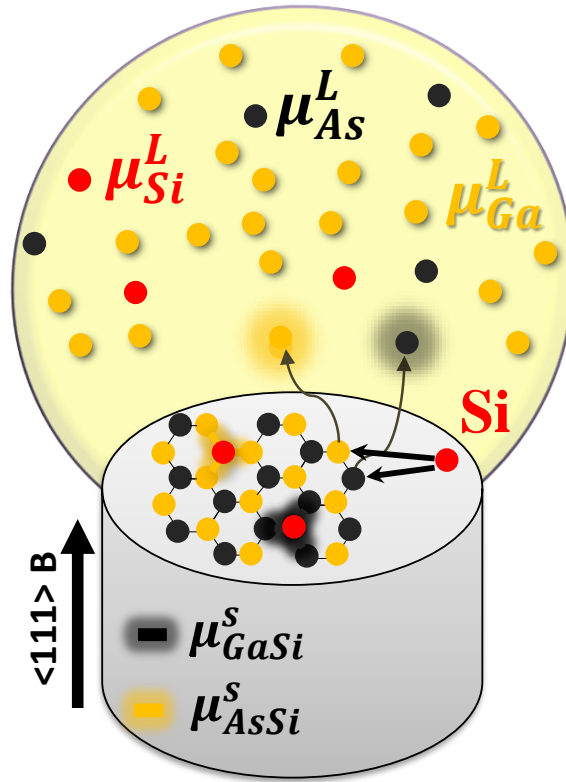


Figure II.5: Illustration of the VLS growth of  $\langle 111 \rangle$ -oriented zinc-blende GaAs NWs with Si, which can be incorporated into either Ga or As sites of GaAs. Replacing Ga with a Si atom ( $n$ -type doping) creates As-Si pair with a contribution  $\epsilon_{AsSi}$  to the total internal energy and increases the chemical potential  $\mu_{Ga}^L$  by adding one Ga atom to the liquid. Replacing As with a Si atom ( $p$ -type doping) creates Ga-Si pair with a contribution  $\epsilon_{GaSi}$  to the total internal energy and increases the chemical potential  $\mu_{As}^L$  by adding one As atom to the liquid.

$$\mu_{GaSi}^S = \mu_{GaAs}^P + \mu_{GaSi}^P - \mu_{GaAs}^P + k_B T \ln(y). \quad (\text{II.15b})$$

Using Eq. II.15 in Eq. II.13, we obtain:

$$x = \exp\left(\frac{\mu_{GaAs}^P - \mu_{AsSi}^P + \mu_{Si}^L - \mu_{Ga}^L + \Delta\mu_{GaAs}}{k_B T}\right), \quad (\text{II.16a})$$

$$y = \exp\left(\frac{\mu_{GaAs}^P - \mu_{GaSi}^P + \mu_{Si}^L - \mu_{As}^L + \Delta\mu_{GaAs}}{k_B T}\right). \quad (\text{II.16b})$$

where  $\Delta\mu_{GaAs} = \mu_{Ga}^L + \mu_{As}^L - \mu_{GaAs}^P$  is the difference of chemical potentials per GaAs pair in the liquid and solid phases [93]. For the  $x/y$  ratio, Eq. II.16 gives:

$$\frac{x}{y} = \exp\left(\frac{A + \mu_{As}^L - \mu_{Ga}^L}{k_B T}\right) \quad (\text{II.17})$$

where  $A = \mu_{GaSi}^P - \mu_{AsSi}^P$ .

Eq. II.17 and its derivation presented here is similar to the classical expression of the Hannay model [129]. However, we prefer to describe the liquid-solid system on the basis of a model involving

atomic pairs rather than individual atoms, as in the classical theory. While Eq. II.17 is insensitive to this choice, the absolute concentrations of donors and acceptors given by Eqs. II.16 in our treatment contain the difference of chemical potentials in liquid and solid, which can only be defined for GaAs pairs [128] and depend on both Ga and As concentrations in the quaternary Au-Ga-As-Si droplet.

Indeed, both Ga and As atoms, with very different concentrations in the droplet, should be transferred from liquid to solid to form stoichiometric GaAs. Furthermore, any Si incorporation into solid GaAs releases either Ga or As atom back into liquid. All these specific features of the liquid-solid growth of GaAs:Si are taken into account in our model. The main contribution to  $A$  is the difference of internal energies between, on one hand, a pure GaAs cell, and on the other hand the same GaAs cell but with a Si impurity replacing either As (system I) or Ga (system II) atom. These energies have been reported for surface segregation [130, 131], which is very unlike the conditions of our VLS system. Therefore, they were evaluated for this work by first principles density functional theory (DFT). All DFT calculations has been done by Philip Eric Hoggan in Institut Pascal whom we thank warmly. A periodic cell of GaAs in the zinc blende structure is constructed from 24 atoms. One is replaced by a Si atom. To evaluate the internal energy of system I, the As is replaced by Si, whereas for system II, Si replaces a Ga atom in the cell. Both systems are repeated with the lattice periodicity. We limit our considerations to the first nearest neighbors, which are four atoms in the zinc blende structure. Therefore, the total estimated internal energies corresponds, on average, to the contribution of four pairs. The contribution of one pair, which we note  $\epsilon_{GaSi}$  or  $\epsilon_{AsSi}$  hereafter, can be obtained simply as one-fourth of the total energies evaluated. The electron density within the cells is nearly all highly localized around the atoms that can be represented by hard spheres. A small portion of the density is completely delocalized and almost isotropic. It is interpreted as the conduction band. The atoms are polarized, their interaction is dominated by electron-nuclear attraction. The internal energy of interaction between the Si dopant atom and its 4 neighbors can thus be determined with reference to the exchange of isolated neutral atoms involved. A diagram showing different steps of the DFT calculation is given in Fig. II.6.

The Perdew-Burke-Ernzerhof (PBE) functional [132] was used within the generalized gradient approximation (GGA). This functional has no fitting parameter and can be considered *ab initio*. An added incentive for this choice is that PBE is one of the few functionals that correctly reproduces lattice geometry. Nevertheless, the system size requires that atomic cores be replaced by pseudo-potentials (giving node-less atomic orbitals on a spherical harmonic basis). This approximation allows us to treat only valence electrons in the DFT band calculation. Each Ga atom should have a  $[3d^{10} 4s^2 4p^1]$  valence shell (13 electrons), whereas As can be treated with only the 5  $[4s^2 4p^3]$  valence electrons, since the metal d electrons participate in the band-structure but not those of electronegative elements (like group V members). Silicon is represented with a  $[3s^2 3p^2]$  ground valence state. Unfortunately, the involvement of 3d electrons in particular, gives rise to a systematic error due to non-locality effects [133]. A lesser but non-zero source of systematic error, of about 0.5% comes from the functional approximation itself. The total systematic error is below 0.05 eV per pair. These calculations used the ABINIT software for periodic solids on plane wave bases. Of course, replacing a host atom with an impurity that differs in size induces a strain energy in the structure. Therefore,

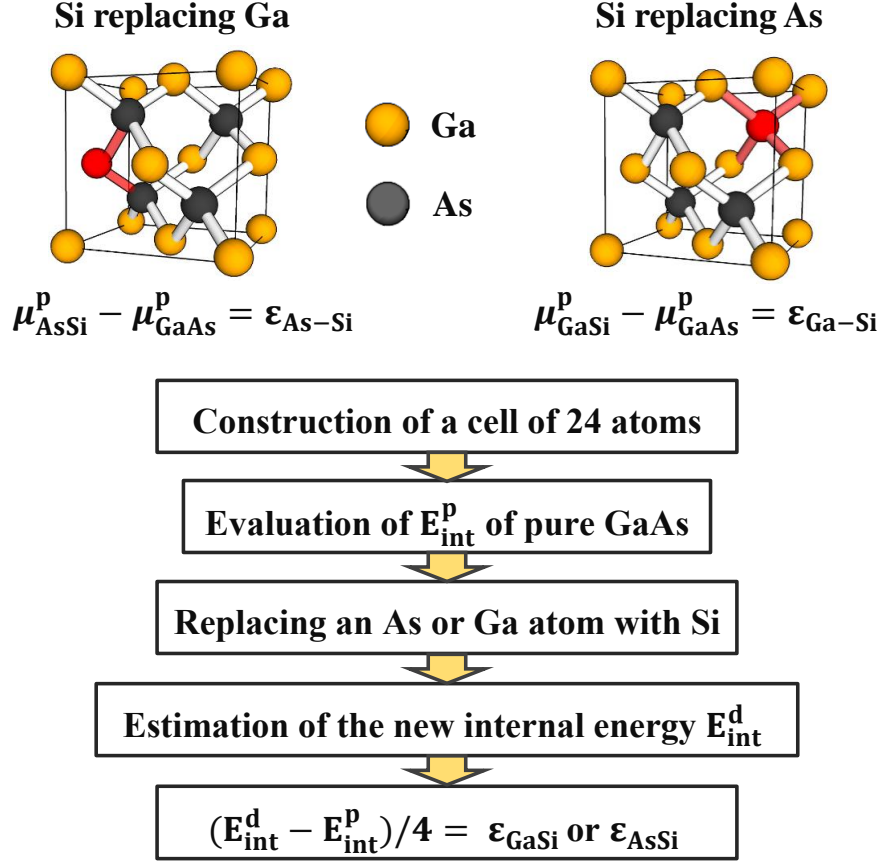


Figure II.6: Diagram showing different steps used for calculating the energy contributions  $\epsilon_{\text{GaSi}}$  and  $\epsilon_{\text{AsSi}}$  by DFT.

we have to consider the relaxation in our calculation. The results for Ga-Si and As-Si pairs are  $\epsilon_{\text{GaSi}} = 2.65 \pm 0.05$  eV and  $\epsilon_{\text{AsSi}} = 2.31 \pm 0.05$  eV. The difference obtained is  $A = 0.34 \pm 0.07$  eV. The coordinates of the atoms in the cells after relaxation are given in the Appendix (A.3).

Using similar considerations for the VS Si doping from vapor, with chemical potentials of Ga atoms  $\mu_{\text{As}}^{\text{V}}$ , Si atoms  $\mu_{\text{Si}}^{\text{V}}$ , and  $\text{As}_2$  molecules  $\mu_{\text{As}_2}^{\text{V}}$ , we obtain:

$$x = \exp\left(\frac{\mu_{\text{GaAs}}^{\text{p}} - \mu_{\text{AsSi}}^{\text{p}} + \mu_{\text{Si}}^{\text{V}} - \mu_{\text{Ga}}^{\text{V}} + \Delta\mu_{\text{GaAs}}}{k_{\text{B}}T}\right), \quad (\text{II.18a})$$

$$y = \exp\left(\frac{\mu_{\text{GaAs}}^{\text{p}} - \mu_{\text{GaSi}}^{\text{p}} + \mu_{\text{Si}}^{\text{V}} - \mu_{\text{As}_2}^{\text{V}}/2 + \Delta\mu_{\text{GaAs}}}{k_{\text{B}}T}\right). \quad (\text{II.18b})$$

Here,  $\Delta\mu_{\text{GaAs}}^{\text{V}} + \mu_{\text{As}_2}^{\text{V}}/2 - \Delta\mu_{\text{GaAs}}^{\text{p}}$  is the difference of chemical potentials per GaAs pair in the gas and solid phases. The  $x/y$  ratio has a similar expression to Eq. II.17, i.e.

$$\frac{x}{y} = \exp\left(\frac{A + \mu_{\text{As}_2}^{\text{V}}/2 - \mu_{\text{Ga}}^{\text{V}}}{k_{\text{B}}T}\right). \quad (\text{II.19})$$

Let us now qualitatively analyze the expressions obtained. We consider liquid or vapor as a metastable mother phase consisting of a mixture of Ga, As and Si. For Au-catalyzed VLS NWs, these atoms are dissolved in liquid Au. Eq. II.16 or II.18 shows that replacing Ga (As) with Si atom in the solid changes the following:

(i) The Gibbs free energy of the solid state, due to the different energies of GaAs and AsSi (GaSi) energy contribution;

(ii) The chemical potential of the mother phase, due to replacing one Si atom by a Ga (As) atom. Both  $x$  and  $y$  increase as  $\exp\left(\frac{\Delta\mu_{GaAs}}{k_B T}\right)$  with increasing  $\Delta\mu_{GaAs}$ ; that is, proportionally to the supersaturation of GaAs. A higher growth rate of GaAs thus increases the incorporation of Si into both Ga and As sites. Clearly, the  $x/y$  ratio determines the type of doping, with  $x/y > 1$  favoring n-type and  $x/y < 1$  favoring p-type doping. The value of  $x/y = 1$  corresponds to the full compensation of donors and acceptors as described in [13, 117, 92], leading to un-doped GaAs.

The  $x/y$  value is independent of the chemical potential of Si and GaAs. The constant in Eqs. II.17 and II.19 is positive and hence favors n-type doping. In the VS growth of GaAs from As and Ga vapors by MBE, the As and Ga chemical potentials in vapor are logarithmic functions of the corresponding partial pressures [33], with  $As_2$  being the dominant species in the vapor under the standard As-rich growth conditions for two-dimensional (2D) layers [134]. In contrast, the VLS growth of GaAs NWs from liquid is characterized by a low As concentration (and hence the corresponding low As chemical potential) due to its high volatility [93, 33, 102]. Comparing Eqs. II.17 and II.19, this qualitatively explains n-type doping of GaAs for planar layers and p-type doping for VLS NWs simply by the fact that it is much more difficult to get As atoms back into vapor than liquid. However, p-type Si doping can also be achieved in planar GaAs layers when the As chemical potential in the vapor is decreased by increasing the growth temperature and lowering the As flux, as in Ref. [126].

For the quantitative analysis of Si doping in VLS GaAs NWs, we should consider the chemical potentials of Ga and As in the liquid phase. In a quaternary Au-Ga-As-Si liquid alloy, both  $\mu_{Ga}^L$  and  $\mu_{As}^L$  are functions of temperature and of the three atomic concentrations  $c_{Ga}$ ,  $c_{As}$  and  $c_{Si}$  for Ga, As and Si, respectively, such that  $c_{Au} = 1 - c_{Ga} - c_{As} - c_{Si}$  [24].

The regular solution model is used, with composition-independent binary interaction constants and temperature-dependent chemical potentials of pure elements given in Table II.1 of the previous section (section II-2). Thus, we compute  $\mu_{Ga}^L$  and  $\mu_{As}^L$  as functions of the three concentrations and temperature as described in the previous section of this chapter (Eqs. II.2a). These chemical potentials are then used in Eq. II.17 with  $A = 0.34$ , as calculated in this work. We then investigate the  $x/y$  ratio as a function of these parameters.

## II.3.2 Results and discussions

Figure II.7-a shows the  $x/y$  ratio as a function of  $c_{Ga}$ , for two different growth temperatures (580 and 715 °C) and different As-concentrations in the droplet (in the range 0.005 and 0.06). Figure II.8

shows the  $x/y$  ratio as a function of  $c_{Ga}$ , at a fixed  $c_{As} = 0.02$  and different temperatures from 400 °C to 650 °C, corresponding to the entire temperature window where the VLS growth of GaAs NWs by MBE is possible [34, 102, 23].

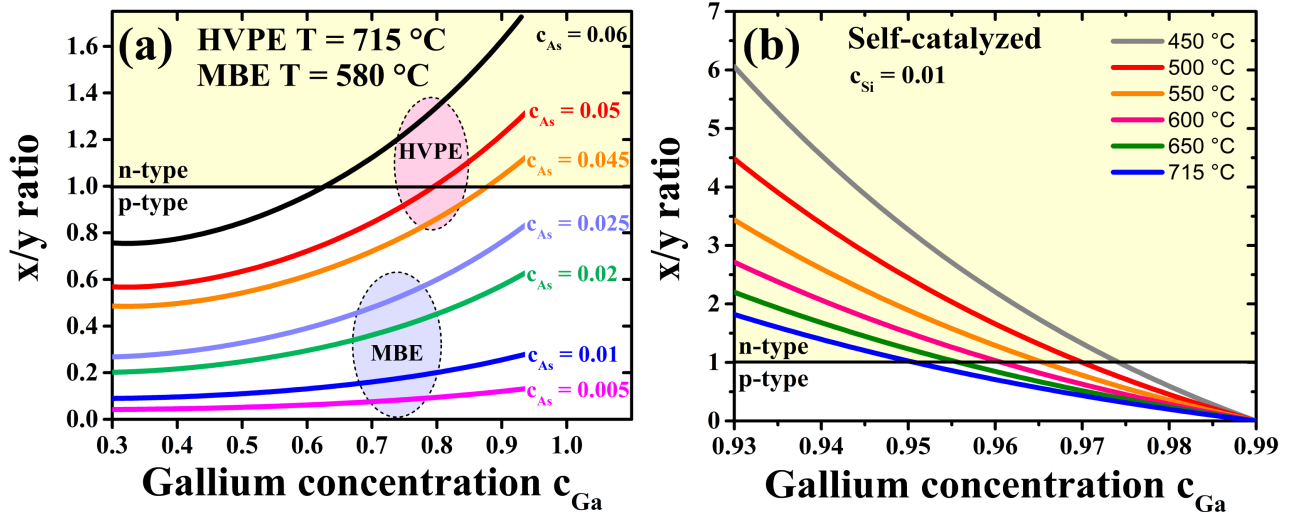


Figure II.7: The ratio  $x/y$  versus  $c_{Ga}$  under the typical MBE (580 °C, low As concentrations  $< 0.025$ ) and HVPE (715 °C, high As concentrations  $> 0.045$ ) growth conditions for Au-catalyzed GaAs NWs. The zero doping line (for  $x = y$ ), corresponds to a ratio of 1. The yellow region above the line corresponds to n-type doping and the white region below the line corresponds to p-type doping. The following trends can be seen: (i) MBE-grown GaAs:Si NWs are always p-type; (ii) In the case of HVPE, GaAs:Si NWs are n-type at lower As and Ga concentrations and p-type at higher As and Ga concentrations; (iii) All HVPE-grown NWs become n-type for  $c_{Ga} > 0.87$ . (b) The ratio  $x/y$  as function of  $c_{Ga}$  for self-catalyzed growth (where  $c_{Ga} = 1 - c_{As} - c_{Si}$ ) at fixed  $c_{Si}$  of 0.01 and different growth temperatures, reveals that n-type doping is favored when increasing As content in the droplet.

The Si concentration is fixed at 0.01. Note however, that the influence of  $c_{Si}$  on the resulting curves is very slight, provided that it remains lower than  $\sim 0.03$ .

Figures II.7 and II.8 clearly reveal the following trends:

- (i) Increasing the As concentration in the catalyst droplet always favors n-type doping;
- (ii) At a fixed As concentration, increasing the Ga content in the droplet favors n-type doping; therefore, n-type GaAs:Si NWs should be more easily obtained in Au-catalyzed growth with Ga-rich droplets,
- (iii) For self-catalyzed VLS process, increasing As concentration in the droplet always favors n-type doping, even though the Ga concentration decreases simultaneously;
- (iv) n-type doping becomes more likely for lower substrate temperatures.

A temperature of 580 °C is quite typical for Au-catalyzed growth of un-tapered GaAs NWs by MBE [34, 102, 22, 115, 23]. Ga-catalyzed GaAs NWs are usually grown at a slightly higher

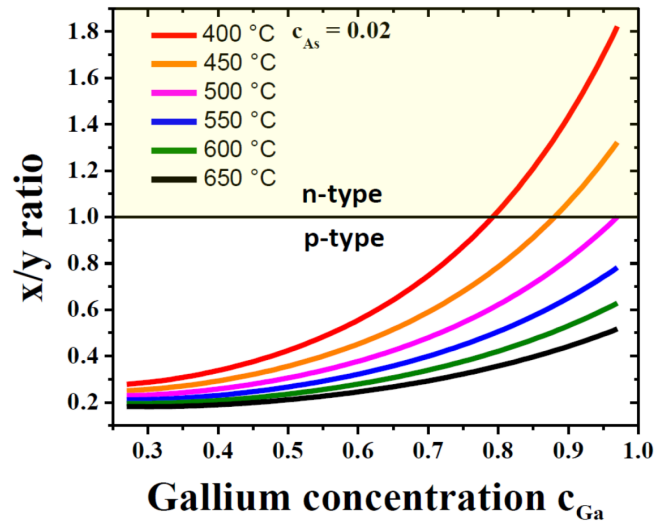


Figure II.8: The ratio  $x/y$  versus  $c_{Ga}$  at a fixed  $c_{As} = 0.02$  and different MBE growth temperatures, showing the tendency for n-type doping at lower temperatures.

temperature, from 580 °C to 650 °C [31, 116, 13, 117, 92, 33]. The MBE technique is characterized by relatively small material inputs and modest NW growth rates, usually lower than 1 nm/s [34]. This corresponds to a low As-concentration in the droplet, which was estimated to be about 0.01 for Ga-catalyzed GaAs NWs at around 600 °C in Ref. [33]. Therefore, a value of 0.025 is probably the upper limit for MBE conditions. Then, according to Figure II.7-a, all MBE-grown GaAs:Si NWs remain p-type over the entire range of Ga concentration, including self-catalyzed growth. Figures II.7-b and II.8 demonstrate, that n-type doping can be achieved using the MBE technique by lowering the growth temperature, particularly for Ga-rich droplets and in the self-catalyzed approach. All these trends are in full agreement with the experimental data of Ref. [115, 116, 13, 117, 92] and clearly show (i) the predominant p-type Si doping of MBE-grown NWs, (ii) the tendency for more compensation, and (iii) the transition to n-type doping at lower temperatures and higher As concentrations. We reiterate that our considerations apply only to the VLS doping mechanism through the droplet, whereas the VS contribution always enhances the concentration of n-type carriers [92].

On the other hand, the HVPE technique is known to produce ultra-long GaAs NWs growing at the record elongation rate ( $\sim 30$  nm/s), with a pure zinc-blende crystal phase [6, 5]. According to Ref. [6], a pure zinc-blende phase requires Ga-rich droplets, with  $c_{Ga}$  higher than 0.65. The As-concentration in the droplet corresponding to a measured elongation rate of 28 nm/s was estimated at  $c_{As} > 0.047$ , despite a high growth temperature of 715 °C [6]. The more recent estimate of Ref. [24] gives even higher values of  $c_{Ga} > 0.9$ . At these high concentrations, the upper curves in Figure II.7-a predict n-type doping. We note that the high temperatures used in HVPE growth generally suppress n-type doping (see Figure II.8) but this effect is more than compensated by extremely high As-concentrations in the droplets, inaccessible in MBE.

We recall that rapid growth in HVPE is ensured by the high de-chlorination rate of the group III precursor (GaCl). The element V precursor is injected, directly inside the hot-wall reactor as

AsH<sub>3</sub>, with a high input flux. It is immediately transformed into As<sub>4</sub> and As<sub>2</sub>. In order to control the supersaturation of the vapor phase during growth, an additional HCl flux is injected inside the reactor (see Chapter I). At a high temperature of 715 °C, this HCl reacts with the Si substrate by etching some Si atoms that are released into the vapor phase as SiCl<sub>4</sub>. This precursor subsequently acts as a dopant flux during the GaAs NW growth [24].

Au-catalyzed HVPE GaAs NWs, considered here, were obtained following the growth protocol explained earlier in Chapter I on Si (111) substrates covered with a native SiO<sub>2</sub> layer. The growth temperature was fixed at 715 °C. A transmission electron microscopy (TEM) image of a representative GaAs NW is shown in Figure II.9-a, along with the inserts revealing its defect-free zinc-blende structure. In order to estimate the doping level of these NWs, micro-photoluminescence ( $\mu$ PL) measurements were performed by Pr. Ray LaPierre and Nebile Isik Goktas from McMaster University in Hamilton, Canada, at 10 K on individual NWs. The carrier concentration was determined by empirical relations based on the full-width-at-half-maximum (FWHM) of the PL peak as reported in [121, 135, 136]. From Refs. [135, 136, 137, 138, 139], it is clearly mentioned that high p-type carrier concentration causes a red-shift in PL spectra, since high carrier concentration decreases the energy gap of the material. On the other hand, high n-type carrier concentration causes a blue-shift in PL spectra, which is ascribed to the Burstein-Moss shift [137, 138]. Therefore, PL spectra with different carrier concentrations can give information about the doping type. Excitation was provided by an Ar<sup>+</sup> laser ( $\lambda = 488$  nm) through a 60x objective. Spectra were collected by a 0.55 m Horiba Jobin Yvon spectrometer and dispersed onto a LN<sub>2</sub> cooled Si CCD detector. In Fig. II.9-b, PL spectra for different Si doping concentrations are shown. It is clearly seen that with increasing carrier concentration, the PL peak shifts to high energy side of the spectra meaning that it shows a blue shift. We can conclude that our Si doped GaAs NWs are showing n-type characteristic. The results were repeatable on other NWs grown under similar HVPE growth conditions. These experimental data fully confirm the model predictions on the n-type Si doping of Au-catalyzed HVPE GaAs NWs due to the high As and Ga contents in the liquid phase.

We used the equilibrium thermodynamic approach to quantify the doping type, determined by the  $x/y$  ratio. Using Eq. II.16, we can obtain the absolute concentrations of electrons and holes, which depend on the chemical potentials of GaAs and Si. Both  $x$  and  $y$  exponentially increase with the  $\Delta\mu_{GaAs}$  value, which gives a measure of supersaturation on the doping levels and will be very different for HVPE, MOVPE and MBE techniques. It will also be interesting to further investigate the influence of the VLS growth kinetics on the Si incorporation. It is clear that the doping concentration is not determined in the nucleation stage, because the critical island consists of only a few III-V pairs [102] and contains no Si atoms. Therefore, the nucleation models for the composition of ternary VLS NWs [96, 95] cannot be used in doping studies. The kinetic approach should preferably be applied. In the latter, the concentrations of free electrons and holes are determined at the stage of island growth [140]. Even the regular growth concept without macroscopic nucleation could be used [141]. The latter case is most likely to occur in NW growing under high material inputs, as in HVPE techniques. Of course, the restriction of stoichiometric composition of ternary III-V NWs, considered in [128, 142, 96, 95, 140, 141], is not relevant for doping. It should be replaced by the amphoteric behavior of

Si consistent with the approach presented here. Finally, we emphasize that our analytic expressions given by Eqs. II.16 and II.17 apply to the general case of any doping that can be incorporated into either anion or cation sites of an arbitrary III-V NW material.

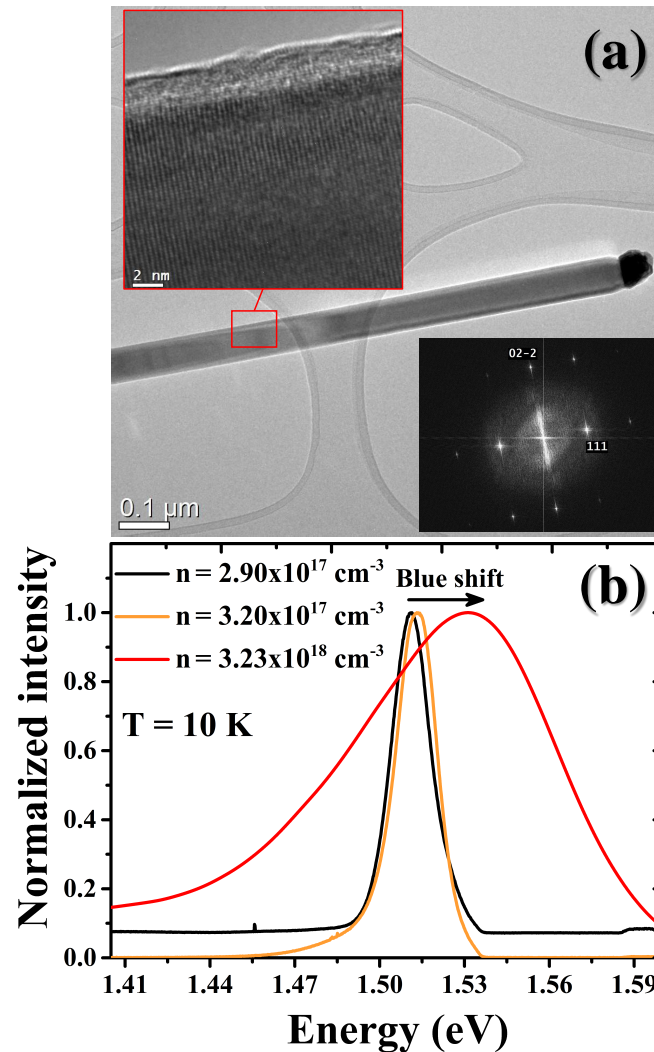


Figure II.9: (a) TEM image of a GaAs NW grown by Au-catalyzed HVPE at 715 °C, showing its un-tapered morphology. High resolution TEM image of the NW section highlighted in red and the corresponding annotated fast Fourier transform in the inserts reveal pure zinc-blende crystal phase of the GaAs NW (done by Catherine Bougerol, Grenoble, France). (b)  $\mu$ PL spectra for different Si doping concentrations at 10 K. The blue shift reveals the n-type behavior of GaAs NWs grown by HVPE.

## II.4 Conclusion

In conclusion, we have developed a thermodynamic model in the first section of this chapter and presented the supporting experimental data showing that adding silicon to Au-Ga-As droplets has a drastic effect on the chemical potentials and the nucleation probabilities of VLS GaAs NWs on silicon substrates. Most importantly, silicon suppresses nucleation from the gallium-rich droplets as long as a certain critical concentration is not reached, with the most difficult nucleation of GaAs NWs occurring in the gold-free self-assisted VLS growth. Adding silicon to the gold-rich droplets only enhances the NW nucleation. We speculate that more silicon should enter the droplets in MOVPE and HVPE due to enhanced silicon etching by chemical precursors. This explains the known problem of gallium-catalyzed growth of GaAs NWs by these techniques. It has been demonstrated that HVPE growth of GaAs NWs always occurs from very gallium-rich droplets due to a high material input of gallium. An oxide layer on Si(111) is then required which blocks out the silicon diffusion into the droplet and helps to start the NW growth. Overall, our model correlates with prior experimental findings and may be further used to understand and control the VLS growth of other III-V NWs on silicon, silicon doping of III-V NWs, and even hybrid III-V-Si NWs.

In the second section, a thermodynamic study of the Si incorporation in GaAs NWs is reported. We have presented a model correlated to experimental data which allows for better understanding of Si doping of Au-catalyzed and Ga-catalyzed GaAs NWs. It has been shown that Si atoms are preferentially incorporated into As, rather than Ga sites of GaAs NWs due to a much lower As/Ga ratio (prevailing) in the mother phase during the VLS growth compared to VS growth. This explains why most VLS GaAs:Si NWs are p-type, while the standard VS growth leads to n-type doping. However, n-type doping of GaAs NWs with Si is expected at higher As concentrations in the droplet, which occurs for HVPE growth on Si substrates. These results can be used for obtaining n-type or p-type Si doping in GaAs NWs by tuning the growth conditions, or even Si-doped p-n junctions within a single NW. Furthermore, they are valid for all VLS-grown III-V NWs by different techniques working at different temperatures and mass inputs.





# Charge and spin transport in GaAs NWs grown by HVPE

## III.1 Introduction

**I**N the last few years, interest in charge and spin transport in semiconductor nanowires (NWs) has been stepping dramatically. The advantage of this kind of structures is to enable an unlimited material design freedom in terms of chemistry and geometry, along with a high structural quality exempt from strain and dislocations. An attractive feature of 1D spin transport is the strong reduction of the spin relaxation speed. For example, if the  $k$  vector is in the  $\langle 111 \rangle$  crystallographic direction, which is the axial direction of our NWs, the Dyakonov-Perel process caused by the spin orbit interaction in the conduction band is no longer efficient [143]. Typical values of spin relaxation times up to 200 ns have been reported for quantum NWs of 20 nm of diameter, in which electrons are spatially confined in a 1D sub-band. This value is 500 times larger than structures exhibiting a continuous 3D electronic band structure [144]. These remarkable characteristics make semiconducting NWs very promising candidates for spin-based devices, such as spin-lasers and spin-FET.

Among the numerous possible applications, we can cite the possibility to create degenerate photoelectron gases at a temperature higher than observed in 3D crystals [145], thus strongly increasing the charge and spin diffusion lengths because of the Pauli principle [146, 147]. Another attractive application is the transfer of spin order from the photoelectrons to the spin of the lattice nuclei. Since the relaxation time of such nuclei can be as high as several tens of hours [148], this method is able to generate bubbles of spin-polarized nuclei with potential applications to quantum spin memories.

Many techniques are being used to investigate the charge and spin dynamics. An interesting one is the Kerr and Faraday Microscopy [149, 150]. It is based on the rotation of the linear polarization plane of an incident probe beam after reflection (or transmission) from a magnetized surface. Another elegant technique is the transient spin and charge gratings [151, 152], which consists in measuring the diffraction dynamics produced by an optically induced grating in a semiconductor. Other

workers scan an electron-beam across a semiconducting NW and measure the change of electron beam induced current (EBIC) as a function of the beam position [153]. Finally, using time-resolved photoluminescence, the carrier lifetime can be measured [154]. In this work, we use a continuous-wave (CW) polarized  $\mu$ -Photoluminescence ( $\mu$ PL) [145, 155]. This technique consists in exciting the semiconductor by a tightly-focused circularly-polarized laser and in monitoring the spatial profiles of the luminescence intensity and circular-polarization. This technique is the only one to enable a simultaneous monitoring of the charge and spin transport in the same conditions.

Among the entire range of III-V semiconductors, GaAs is known to be particularly suitable for spintronic [156], electronic devices [11], as well as for optical investigation of charge and spin transport using optical spin orientation. For this material, it was reported that the dimensions of the studied system have an influence on the charge transport [157, 158]. However, a large majority of studies report submicronic diffusion lengths. The charge diffusion length  $L_e$  has been reported to reach its maximum value of 4  $\mu\text{m}$  at LT in quantum NWs of diameter equals to 15 nm, and to decrease when increasing NW width [158]. This is consistent with the values of  $L_e < 1 \mu\text{m}$  obtained for NWs of diameters up to 50 nm at LT [159, 160, 161, 162] and RT [153]. Finally, to the best of our knowledge, spin transport is very rarely studied in NWs.

In this chapter, our interest will be focused on investigations of charge and spin transport in GaAs NWs of high structural quality grown by HVPE (Chapter I). It is known that GaAs surfaces suffer from immediate oxidation which leads to a degradation of transport properties. In order to reduce this effect, two surface passivation methods are used in the present work: the first is with  $\text{N}_2$  plasma under UHV conditions in Institut Pascal, and the second is a chemical treatment using hydrazine-sulfide solutions. We show that very high charge and spin diffusion lengths can be reached in passivated NWs. Record values of 6  $\mu\text{m}$  for charge and slightly lower for spin diffusion lengths are obtained along with high electronic spin-polarizations (20%). To generate a spin-polarized electronic gas, we excite the NW with highly-focused circularly-polarized light. These properties are investigated as function of NW diameter, doping level and excitation power.

The present chapter is a collaborative work with D.R. Daniel Paget, a research director from Physique de la Matière Condensée (PMC) group of Ecole Polytechnique in Paris, where I spent several months of my thesis to achieve this study. These stays were supported financially by CPER Région Auvergne.

## III.2 Optical spin orientation in GaAs

In a semiconductor, optical excitation of energy larger than the bandgap results in a transfer of an electron from the valence band (VB) to the conduction band (CB) by absorption of a photon. During this process, a hole is created in the VB for each electron transferred in the CB. The band structure of GaAs near  $k = 0$  is represented in Fig. III.1-a.

The kinetic energies of photo-generated carriers ( $\Delta\epsilon_C$  for electrons and  $\Delta\epsilon_V$  for holes) are de-

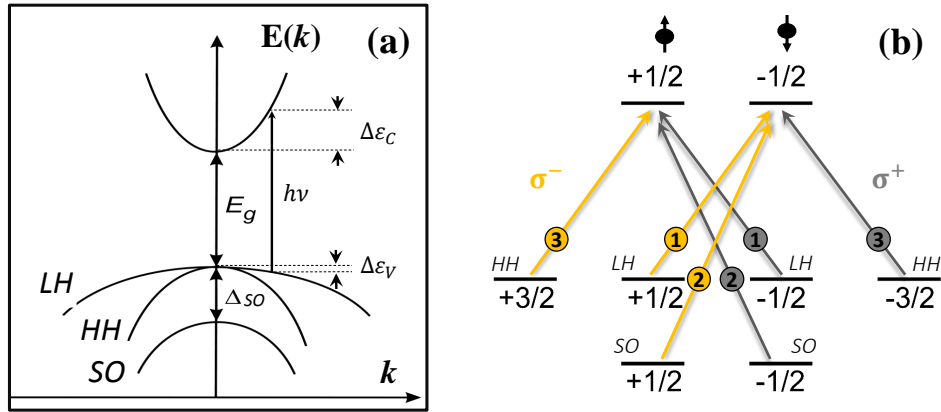


Figure III.1: (a) The dispersion relation near  $k = 0$  of GaAs of zinc blende structure. The maximum of the VB and the minimum of the CB are both situated at  $k=0$  ( $\Gamma$  point), revealing that GaAs is a direct bandgap semiconductor. At this point, the bands are considered parabolic. The VB is composed of three sub-bands. Two of them are degenerate (HH for heavy holes and LH for light holes), and the spin-orbit split-off band lies at an energy  $\Delta_{SO}$  below the energy levels of the others. (b) At  $k = 0$ , choosing the light excitation axis as the quantization axis, the states are labeled by their  $m_j$  quantum number, the projection of the total angular momentum on the axis of propagation of light. The allowed transitions following the absorption of right ( $\sigma^+$ ) or left ( $\sigma^-$ ) circularly-polarized photons of energy  $E_g < h\nu < E_g + \Delta_{SO}$  are represented in gray and yellow arrows, respectively, with the respective probabilities circled. The two particles with arrows heading up and down in the CB represent the two electron states, i.e. spin up and down respectively, after excitation.

terminated by the incident photon energy. If the photon energy is such that  $E_g < h\nu < E_g + \Delta_{SO}$ , the transition from the spin-orbit split-off band is not possible, where  $\Delta_{SO}$  is the energy of the spin-orbit split-off band. After establishment of an equilibrium and relaxation to the bottom of the conduction band, the photo-excited carriers live some time  $\tau_c$  before recombining. This recombination can be radiative (with emission of a photon of energy close to the bandgap) or non-radiative.

In addition to the electron momentum conservation during optical transitions, the conservation of the angular momentum is a fundamental law in physics and has to be respected. That is to say, following the absorption of right ( $\sigma^+$ ) or left ( $\sigma^-$ ) circularly-polarized photon, the allowed transitions are only those that ensure the projection of the angular momentum along the propagation axis  $\Delta m_j = \pm 1$ . These are known as optical selection rules presented by arrows in Fig. III.1-b with their respective probabilities in circles.

According to the selection rules, the absorption of an incident photon of circular polarization  $\sigma^\pm$  gives rise to a spin-polarized electron  $\mp$  in the CB with a probability 3 times larger than  $\pm$ . So the initial electronic spin polarization will be:

$$P_i = \frac{g_+ - g_-}{g_+ + g_-} = 50\% \quad (\text{III.1})$$

where  $g_{\pm}$  is the generation rate of electrons with helicity  $\pm$ . The steady-state electronic spin polarization is defined as:

$$P = \frac{n_+ - n_-}{n_+ + n_-} = \frac{s}{n} \quad (\text{III.2})$$

where  $n_+$  ( $n_-$ ) is the density of photo-created electron of spin up (down).  $s = n_+ - n_-$  and  $n = n_+ + n_-$  correspond to the difference and the sum of the densities of photocreated carriers of spin up and down. It is likely to be smaller than  $P_i$  if there occurs spin-relaxation of photoelectrons during their lifetime.

Therefore, it is possible to create a non-equilibrium spin polarization in a semiconductor by absorption of circularly-polarized light. This is called the optical pumping, demonstrated experimentally for the first time by G. Lampel [163] in Ecole Polytechnique in 1968 on Silicon. This phenomenon mainly concerns the photoelectrons since holes have an extremely short spin relaxation time, and are generally spin-unpolarized.

Notice that this process is reversible in time, meaning that radiative recombination transition from the CB to the VB is governed by the same selection rules as those in Fig. III.1-b. That is to say, a spin-polarized electron  $\pm$  will relax to equilibrium state by emitting a circularly-polarized photon  $\sigma^{\mp}$  with a probability 3 times larger than  $\sigma^{\pm}$ . Experimentally, the measurement of the intensities  $I^{\pm}$  of the  $\sigma^{\pm}$  components of the luminescence allows us to calculate the sum and difference intensities as follows:

$$I_s = I^+ + I^- = Kn \quad (\text{III.3a})$$

$$I_d = I^+ - I^- = P_i K s \quad (\text{III.3b})$$

where  $K$  is a constant. From these equations, it is seen that the degree of circular polarization of the luminescence  $P_{lum}$  will be related to the electron spin polarization  $P = s/n$  according to:

$$P_{lum} = \frac{I_d}{I_s} = \frac{I^+ - I^-}{I^+ + I^-} = -0.5P \quad (\text{III.4})$$

It will be shown below that a  $\mu$ PL technique, based on local measurement of luminescence intensity and circular polarization, allows us to investigate charge and spin transport.

## III.3 Polarization resolved $\mu$ -Photoluminescence $\mu$ -PL

### III.3.1 Principle of the method

This method consists in exciting the NW by a tightly-focused circularly-polarized laser, and in investigating at a given luminescence energy the spatial profiles of  $I_s$  and  $I_d$  defined in Eqs. III.3-a and b. A schematic representation of the technique is given in the left panel of Fig. III.2. As shown in the right panel, the  $\sigma^+$  or  $\sigma^-$  circularly-polarized laser beam  $h\nu$  creates a spin-polarized electron gas that diffuses laterally inside the NW, until radiative recombination, with emission of a circularly-polarized  $\sigma^+$  or  $\sigma^-$  photon. In red is the initial excitation laser profile and in blue are the sum and difference profiles. These profiles extend beyond the laser, thus revealing charge and spin diffusion.

In the case where these profiles are proportional respectively to  $n$  and  $s$ , they give the charge  $L_c$  and spin  $L_s$  diffusion lengths. In order for the measurements to be reliable without any birefringence ef-

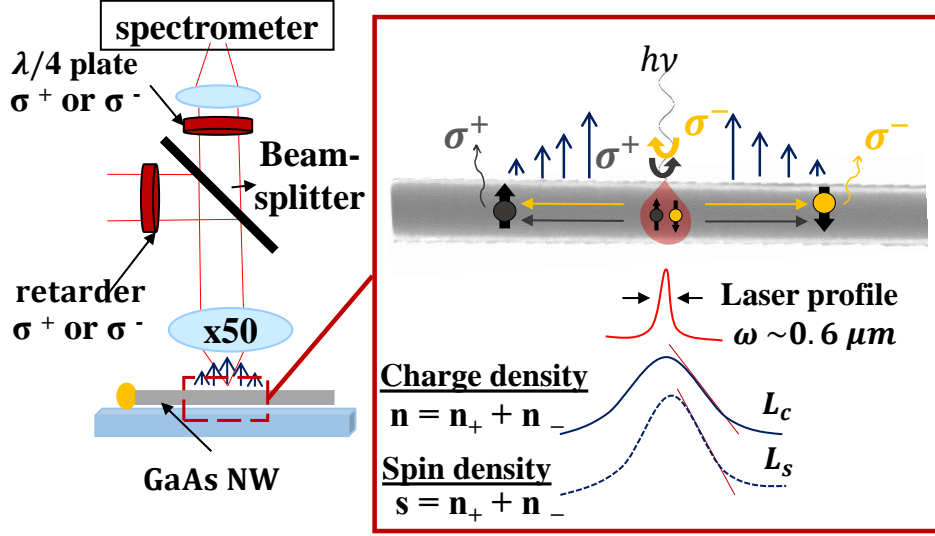


Figure III.2: A schematic representation of the  $\mu$ PL technique showing the excitation, the GaAs NW (sample) and the analysis parts. The right panel is a zoom on the processes occurring in the NW, showing the laser spatial profile and the profiles of charge and spin density, giving respectively the charge and spin diffusion lengths.

fects, both  $\sigma_{exc}^+$  and  $\sigma_{exc}^-$  are in turn used to excite the sample and, for each,  $\sigma_{rec}^+$  and  $\sigma_{rec}^-$  are collected at the reception. Therefore, we obtain 4 images denoted, hereafter,  $\sigma^{++}$ ,  $\sigma^{+-}$ ,  $\sigma^{--}$  and  $\sigma^{-+}$ , where the first sign is the excitation helicity and the second stands for the reception.

These images are combined to form sum and difference image given by:

$$I_{sum} = 0.5 (\sigma^{++} + \sigma^{+-} + \sigma^{--} + \sigma^{-+}) \propto Kn \quad (III.5a)$$

$$I_{diff} = 0.5 (\sigma^{++} - \sigma^{+-} + \sigma^{--} - \sigma^{-+}) \propto P_i K s \quad (III.5b)$$

here,  $n(s)$  represents the charge (spin) density, and  $K$  is a constant that depends on the ratio radiative/non-radiative recombination and on the parameters of the PL detection. [164]

### III.3.2 Experimental setup

The experimental setup is presented in Fig. III.3-a. An excitation laser beam of energy 1.59 eV serving for excitation is initially linearly-polarized before passing through a variable liquid crystal retarder. This retarder is controlled by an external switch, allowing us to change the retardation and, therefore, to switch from linear polarization to  $\sigma_{exc}^+$  or  $\sigma_{exc}^-$ . The resulting laser spot radius  $\omega$  on the sample is about  $0.6 \mu m$ , nearly diffraction-limited. The excitation power ( $P_{exc}$ ) of the laser can be adjusted by means of density filters.

The sample is fixed in a cryostat with a liquid Helium flow, enabling to control the temperature in a wide range between 5 and 300 K. After being aligned with the center of the tele objective, the incident laser has to pass through the cryostat's 1 mm thick BK7 window to reach the sample. That is why the objective is equipped with a compensation ring to limit aberrations. In order to accurately spot the NW, we use a scanning-mirror and telecentric lenses system that allow us to precisely move the laser. The auxiliary CCD camera is used during this process.

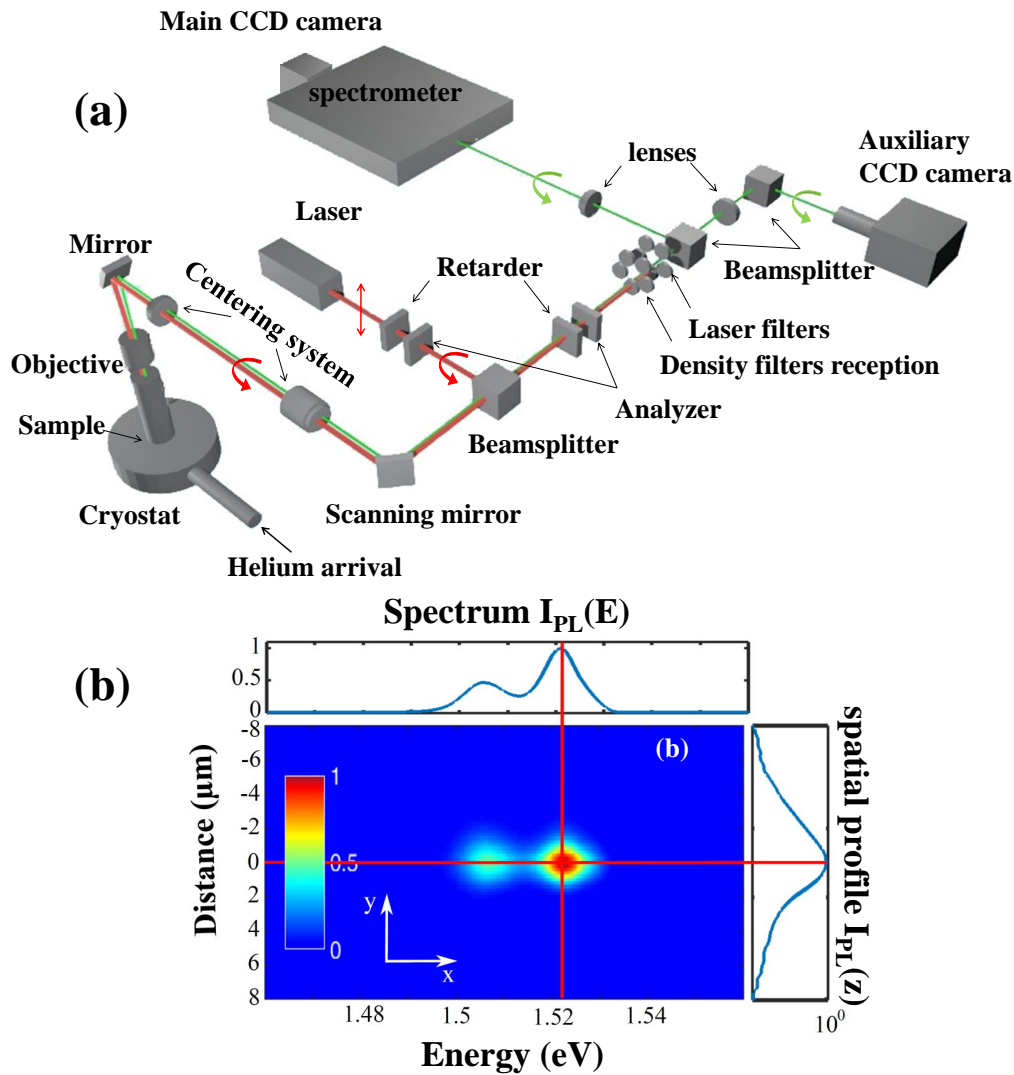


Figure III.3: Panel (a) shows a schematic representation of the experimental setup. Panel (b) shows a typical image of the CCD behind the monochromator obtained at 6 K on a  $10^{17} \text{ cm}^{-3}$  p-doped GaAs 2D layer. It is energetically and spatially-resolved along the x and y axis, respectively. Energetically and spatially integrated sections are shown by red lines, with the corresponding spectrum and profile shown in the top and left boxes, respectively.

Luminescence coming from the sample is analyzed by an externally-controlled quarter wave plate, and focused on the entrance slit of the spectrometer. If the spectrometer is set to zero, the CCD camera simply gives a spatial image of the sum and difference profiles, without any spectral resolution. At order 1, this spectrometer allows for energy-resolved spatial imaging of the charge and spin diffusion. This is shown in Fig. III.3-b in the case of p-type bulk GaAs at 6 K. Section of the

image along a horizontal axis (perpendicular to the slit) gives the luminescence spectrum at a given position on the sample on a straight line parallel to the entrance slit. Conversely, section of the image along a vertical axis at a given energy gives the spatial profile at the corresponding energy. It is then possible, provided the NW is parallel to the entrance slit, to study the diffusion profile of electrons as a function of the emission energy of the luminescence.

Since we shall be monitoring strongly decreasing spatial profiles, it is mandatory not to limit the dynamic range of the measurements and to eliminate all parasitic lights not related to the sample luminescence. First of all, since the excitation energy of the laser is cleanly selected at the source by adding a "laser clean-up" filter which transmits a narrow energy band centered on the laser and blocks other wavelengths, we can exclude all parasitic light due to the excitation setup. Moreover, the reception part contains components that may induce uncontrollable light scattering or generate luminescence. This parasitic light is suppressed by, exciting the NW and collecting data first, and then slightly moving the laser spot and exciting the silicon substrate close to the NW (see insert in Fig.III.4). Since no luminescence is emitted from this substrate, the measured signal consists only of the parasitic signal, and thus can be subtracted from the NW luminescence. This is shown in Fig. III.4 in a case where the PL signal is weak with respect to the background signal.

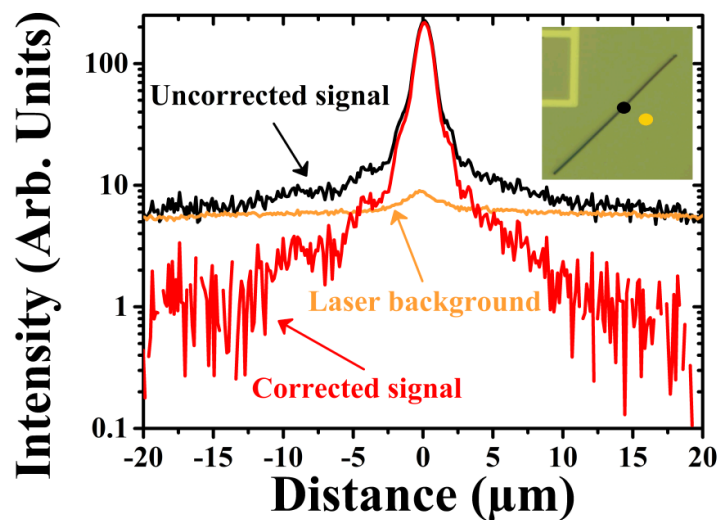


Figure III.4: *The insert is a schematic representation of the method used to clean up the data from parasitic laser contributions. By analogy with the profiles, the black spot represents the laser on the NW and the orange one gives the laser background by exciting the silicon substrate near the NW. Energetically integrated profiles of the uncorrected PL signal (in black) along with the laser background (in orange). The obtained corrected PL signal is shown in red after subtracting the black and the orange profiles.*

We see that parasitic light, which dominates the profiles for distances larger than 10  $\mu\text{m}$  is completely removed so that the corrected spatial profile can be investigated up to about 20  $\mu\text{m}$ .

## III.4 Background on spin and charge transport in GaAs

### III.4.1 The diffusion equation

We will consider the NW geometry described in Fig. III.5. This geometry shows the subsurface space charge region of width  $w_{SCR}$ .

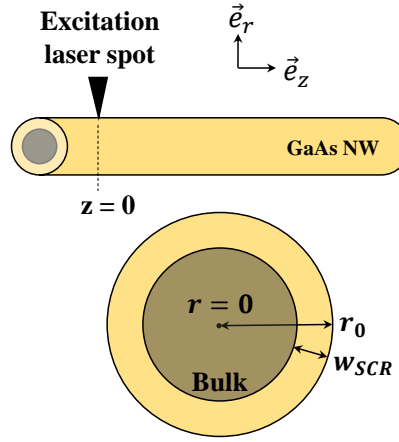


Figure III.5: A schematic representation of the studied NW. The  $r$  axis is taken parallel to its radius and the  $z$  axis is along its axis. The gray region represents the bulk of the NW and the orange one is the surface charge region SCR caused by localized surface states (discussed later).

For electronic spins  $\pm$ , the diffusion continuity equations can be expressed in steady-state as:

$$\frac{\partial n_{\pm}}{\partial t} = g_{\pm}(r, z) - \frac{n_{\pm}}{\tau_c} - \frac{1}{2T_1} (n_{\pm} - n_{\mp}) + \vec{\nabla} \cdot (D_e \vec{\nabla} n_{\pm}) \quad (\text{III.6})$$

The first term  $g_{\pm}$  describes the electron generation rates per unit volume as defined in Fig. III.1.  $\tau_c$  is the electron lifetime in the conduction band and  $T_1$  is the spin relaxation time. The last term on the right side represents the current density of electrons, with the diffusion term containing the diffusion coefficient  $D_e$ .

Here, we focus only on electrons because the photo-generated holes are not spin-polarized. This is due to their spin relaxation time smaller than their lifetime by several orders of magnitude [165, 166].

These considerations allow us to write the charge and the spin continuity equations, often named Helmholtz equations, as:

$$(g_+(r, z) + g_-(r, z)) - \frac{n}{\tau_c} + D_e \Delta n = 0. \quad (\text{III.7a})$$

$$(g_+(r, z) - g_-(r, z)) - \frac{s}{\tau_s} + D_e \Delta s = 0. \quad (\text{III.7b})$$

where the diffusion constant  $D_e$  is considered similar for charge and spin, and  $\tau_s$  such that:

$$\frac{1}{\tau_s} = \frac{1}{\tau_c} + \frac{1}{T_1} \quad (\text{III.8})$$

is the spin life time. These equations are written for photoelectrons assuming, as we will show below that for n-type NW, that they lie at an energy higher than dark electrons, and that they undergo diffusive transport.

In the present case, the absorption depth ( $\sim 1\mu\text{m}$  for a laser of  $E = 1.59$  eV in our experiment) is usually much larger than the typical dimension parallel to the excitation incidence. Therefore, the generation term  $g_{\pm}(r, z)$  can be considered constant throughout the cross section area and only dependent on  $z$  according to:

$$g_{\pm}(z) = g_{\pm} \exp\left(-\frac{(z-z_0)^2}{\omega^2}\right) \quad (\text{III.9})$$

where  $\omega$  is the radius of the laser spot. Given the shape of the NWs, Eqs. III.7-a and III.7-b must be solved in cylindrical coordinates, with  $z$  is the axial direction and  $r$  is the radial one (Fig. III.5). The Laplacian operator is then given by  $\Delta = \frac{1}{r} \frac{\partial}{\partial r} r \frac{\partial}{\partial r} + \frac{\partial^2}{\partial z^2}$ .

With these considerations, the Helmholtz equation (Eq. III.7) can be rewritten as:

$$L_c^2 \left( \frac{1}{r} \frac{\partial}{\partial r} r \frac{\partial n(r, z)}{\partial r} + \frac{\partial^2 n(r, z)}{\partial z^2} \right) - n(r, z) + g(z) \tau_c = 0. \quad (\text{III.10})$$

Here,  $L_c = \sqrt{D_e \cdot \tau_c}$  is the diffusion length of electrons in the bulk,  $g(z) = (g_+(z) + g_-(z))$  is the generation rate of electrons and  $S$  is the surface recombination velocity. The boundary condition of this equation, for a NW of radius  $r_0$ , is given by:

$$\left. \frac{\partial n(r, z)}{\partial r} \right|_{r=r_0-w_{SCR}} = -\frac{S}{D_e} n(r_0 - w_{SCR}) \quad (\text{III.11})$$

This condition expresses that the diffusive current  $D_e \vec{\nabla} n(r)$  is entirely compensated by the recombination current  $Sn(r)$  at the surface.

A similar equation can be written for the spin orientation:

$$L_s^2 \left( \frac{1}{r} \frac{\partial}{\partial r} r \frac{\partial s(r, z)}{\partial r} + \frac{\partial^2 s(r, z)}{\partial z^2} \right) - s(r, z) + g_s(z) \tau_s = 0. \quad (\text{III.12})$$

with  $L_s = \sqrt{D_e \cdot \tau_s}$  and  $g_s(z) = (g_+(z) - g_-(z))$ .

The general solution of Eq. III.10, as discussed in Appendix B.1, is expressed as a sum of spatial modes. In the present case, because of the weak surface recombination regime, only the lowest order mode can be considered. Assuming that the luminescence intensity at position  $z$  is proportional to the integral of  $n(z)$  over  $r$ , this gives an exponential decay of the luminescence intensity along the  $z$  axis, for which the characteristic length depends on the NW radius and the surface recombination velocity. That is:

$$I_{PL}(z) \sim \int_0^{\infty} \exp\left(-\frac{z_0}{L_c^*}\right) g(z_0 - z) dz_0 \quad (\text{III.13})$$

The effective diffusion length  $L_c^*$  of this mode is the length of the lowest order mode, which is expressed as:

$$L_c^* = L_0 = \frac{L_c}{\sqrt{1 + k_0^2 L_c^2}} \quad (\text{III.14})$$

where  $k_0$  is given by  $k_0 r_0 \approx 1.2 \sqrt{\frac{S r_0}{D_e}}$

### III.4.2 Other contributions to the charge and spin transport

In the present section, we discuss the various processes according to which charge and spin transports likely differ from the above simple picture.

#### III.4.2.1 Ambipolar coupling

Due to the smaller diffusion constant  $D_h$  of holes with respect to electrons, an electric field  $E_a$ , of ambipolar origin, appears between these two gases [145, 155, 146]. This electric field has to be taken into account when writing the continuity equations of the system for electrons and holes, which can be expressed as follows:

$$\vec{\nabla} \left\{ \mu_n n \vec{E}_a - D_e \vec{\nabla} n \right\} + g - \frac{n}{\tau_c} = 0 \quad (\text{III.15a})$$

$$\vec{\nabla} \left\{ -\mu_p p \vec{E}_a + D_h \vec{\nabla} p \right\} + g - \frac{p}{\tau_c} = 0 \quad (\text{III.15b})$$

where  $p$  is the concentration of photogenerated holes. The term involving the electric field  $\vec{E}_a$  is responsible for the electrostatic coupling between electrons and holes. It tends to ensure the spatial charge neutrality condition, i.e. to have  $n = p$  at any point of the semiconductor [147]. In n-type semiconductors, for example, this coupling brings back the electrons to the center and expels out the holes, modifying the exponential spatial profiles [155]. This term can be eliminated by coupling the two equations. As a result, Eqs. III.10 and III.12 are still valid, provided  $D_e$  is replaced by the ambipolar diffusion constant  $D_a$ , which is a weighted average of the diffusion coefficient called ambipolar diffusivity, given by:

$$D_a = \frac{\sigma_e D_h + \sigma_h D_e}{\sigma_e + \sigma_h} \quad (\text{III.16})$$

where  $\sigma_e = |q| n \mu_e$  and  $\sigma_h = |q| p \mu_h$  are the electron and hole conductivities, respectively, and  $\mu_e$  and  $\mu_h$  are their mobilities.

#### III.4.2.2 The nature of recombination

Several types of recombination processes can be considered. Apart from non-radiative recombination, characterized here by a time  $\tau_{nr}$ , other recombination processes can be monomolecular and radiative with a time  $\tau_r$  independent on electron concentration, or bimolecular, for which the inverse time  $Kn$  is

proportional to the electron concentration and  $K$  is the bimolecular constant. This inverse time is equal to  $K(n_0 + N_D)$  where  $n_0$  is the optically generated electron concentration and  $(n_0 + N_D)$  is the total electron concentration. In summary, the recombination-induced evolution of electron concentration is given for the two carriers by:

$$-\left.\frac{\partial p}{\partial t}\right|_{rec} = -\left.\frac{\partial n}{\partial t}\right|_{rec} = \frac{n}{\tau_{nr}} + \frac{n}{\tau_r} + K(n_0 + N_D)p \quad (\text{III.17})$$

For the present NWs, it will be assumed that non-radiative, monomolecular recombinations are dominant, so that no nonlinear term appears in the diffusion equation. For band-to-band luminescence, the PL intensity is proportional to  $K(n_0 + N_D)$ . At low excitation power  $n_0 \ll N_D$ , the luminescence intensity  $I_{PL}$  will be proportional to  $p$  ( $p \approx n$ ), i.e. to the excitation power. If on the other hand  $n_0 \gg N_D$ ,  $I_{PL}$  will be proportional  $p^2$ , where  $p \approx n$  is calculated in section III.4.1.

### III.4.2.3 Self-trapping effect of the photovoltage

In the same way as for bulk semiconductors there is at the surface a band bending (BB) of magnitude  $\phi_b$ , which is upwards for n-type semiconductors (see Fig. III.6). Application of the Poisson's equation in cylindrical coordinates is performed in Appendix B.2, and shows that the width of the subsurface depletion layer  $w_{SCR}$  depends on the NW radius. If  $w_{SCR} \ll r_0$ ,  $w_{SCR}$  is the same as for planar surfaces. On the other hand, if  $w_{SCR} \simeq r_0$  (nearly depleted NW), we have:

$$w_{SCR} = 2\sqrt{\frac{\epsilon_r \epsilon_0 \phi_b}{|q| N_D}} \quad (\text{III.18})$$

which is larger than for planar surfaces by a factor  $\sqrt{2}$ . Here  $\epsilon_0$  denotes the vacuum permittivity and  $\epsilon_r$  is the dielectric constant.

Under light illumination, holes are injected in the BB region, and reduce the BB height locally near the place of laser excitation [167]. Because of the large screening by holes in the BB region, the reduction of barrier height will manifest itself in the bulk rather than at the surface (see Fig. III.6) [[168]]. This photovoltage will generate an axial current, i.e. along the NW axis.

The resulting hole flux is then towards the place of excitation. As detailed in Appendix B.3, for planar surfaces, this flux exactly compensates the outward diffusive flux, leading to photocarrier self-trapping in the zone where the photovoltage is larger than  $k_B T$ . This self-trapping has been shown to increase the PL intensity at the place of excitation and therefore to modify the spatial profile.

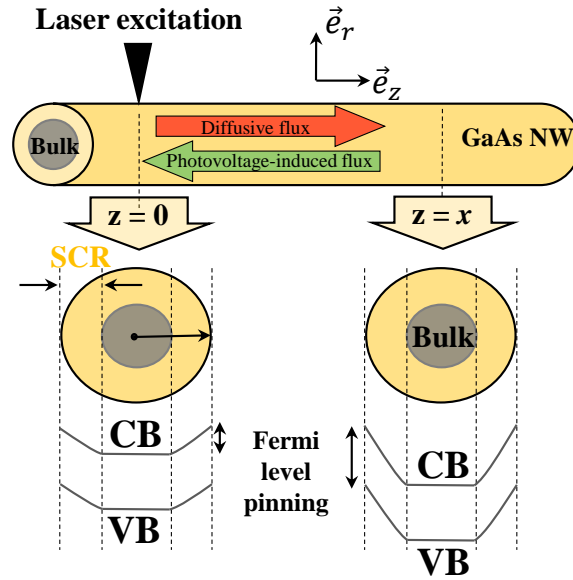


Figure III.6: The laser spot excites the NW at  $z = 0$ . Below are the cross sections under the laser spot and at  $z = x$ , showing the presence of the surface charge region (SCR) (in yellow) that surrounds the bulk (in grey). Also shown are the band structures that reveal the barrier band bending in this SCR. Outside the excitation zone ( $z = x$ ), the band-bending is larger than underneath the laser spot ( $z = 0$ ). The hole flux induced by the surface photovoltage is represented by a green arrow, whereas the diffusive flux is represented by the red one.

### III.5 Spin and charge diffusion in HVPE-grown GaAs NWs: introduction

In the present chapter, our interest is focused on investigating the charge and spin transport in single ultra-long GaAs NWs grown on Si(111) substrates by HVPE (see Chapter I) [5, 6]. We consider eight distinct NWs, for which the characteristics are summarized in Table III.1. For comparison, we also present some results on NWs grown on GaAs substrates.

NW	length ( $\mu\text{m}$ )	diameter $d$ (nm)	surface	substrate	NI-doping
NW1	60	300	oxidized	GaAs (100)	p-doped
NW2	120	250	oxidized	Si(111)	n-doped
NW3	120	200	hydrazine passivation	GaAs (100)	p-doped
NW4	50	90→500	hydrazine passivation	Si(111)	n-doped
NW5	40	250	plasma passivation	Si(111)	n-doped
NW6	75	90	hydrazine passivation	Si(111)	n-doped
NW7	60	300	hydrazine passivation	Si(111)	n-doped

Table III.1: Description of the investigated NWs.

All of them were grown under the conditions described in Chapter I. As found from Eq. III.14, the effective diffusion length is likely to be strongly reduced with respect to its bulk value in real conditions because transport in NW is strongly sensitive to surface recombination. As a result, NWs were investigated after surface passivation using hydrazine chemical solutions or nitrogen plasmas. For comparison, NW2 and NW1 were left naturally oxidized after growth.

Then the NWs, standing on the substrate, were scraped and deposited horizontally on grids of lattice spacing  $15 \mu\text{m}$ . An optical microscope was used to spot the NWs and to note their coordinates on the grids and an electron microscope was used to determine their diameters.

We mention that experiments at room temperature have shown an irreversible degradation of the PL emission for all NWs. This degradation was reduced for the passivated ones, but did not enable reproducible investigation. Therefore, all the results presented hereafter were obtained at low temperature around 6 K.

### III.5.1 Determination of the doping levels

As seen in Chapter II, growing GaAs NWs on Si(111) results in a non-intentional n-doping by Si atoms coming from the substrate.

In the present section, we propose a new method to determine the NW doping level. It is based on the estimate of the width of the surface depletion layer that allows for estimating the carrier concentrations. For this estimate, an independent setup was used. This setup enabled the determination of the spatially-integrated PL intensity while scanning a focused He-Ne laser beam across the NW at room temperature. This technique is quite different from the above  $\mu\text{PL}$  imaging since in the latter the laser position is kept fixed.

An optical view of the NW4 close to its tip is shown in panel A of Fig. III.7-a. Panel B shows the map of the luminescence intensity. As verified in Panel C which shows the spatial profile of the PL intensity along the NW, a very weak signal is observed in the first  $5 \mu\text{m}$  of the NW. This is interpreted since the diameter gradually changes from about 90 nm at the NW top to about 500 nm at its base. As observed elsewhere [169], the section of the NW giving a relatively weak luminescence is entirely depleted so that band-to-band radiative recombination is strongly reduced because of the absence of electrons in the dark. It is also seen that luminescence intensity  $I_{PL}$  is approximately proportional to  $r_0$ . Since one expects that: [169]

$$I_{PL} \propto \frac{gr_0}{2S} \left[ 1 + \frac{1}{4} \frac{Sr_0}{D_e} \right] \quad (\text{III.19})$$

where  $g$  is the rate of creation,  $S$  is the recombination velocity and  $D_e$  is the electron diffusion constant, this suggests that the NW at 300K is in the recombination limited regime defined by  $Sr_0/D_e \ll 1$  [170]. Such conclusion will be confirmed below, as explained in Appendix B.2.

From the estimate of the NW diameter at the threshold ( $\approx 180 \text{ nm}$  as shown in the insert of Fig. III.7-a), and using Eq. III.18 and a barrier height of 0.75 eV, we find a doping level of  $\approx 3.2 \times 10^{17} \text{ cm}^{-3}$ .

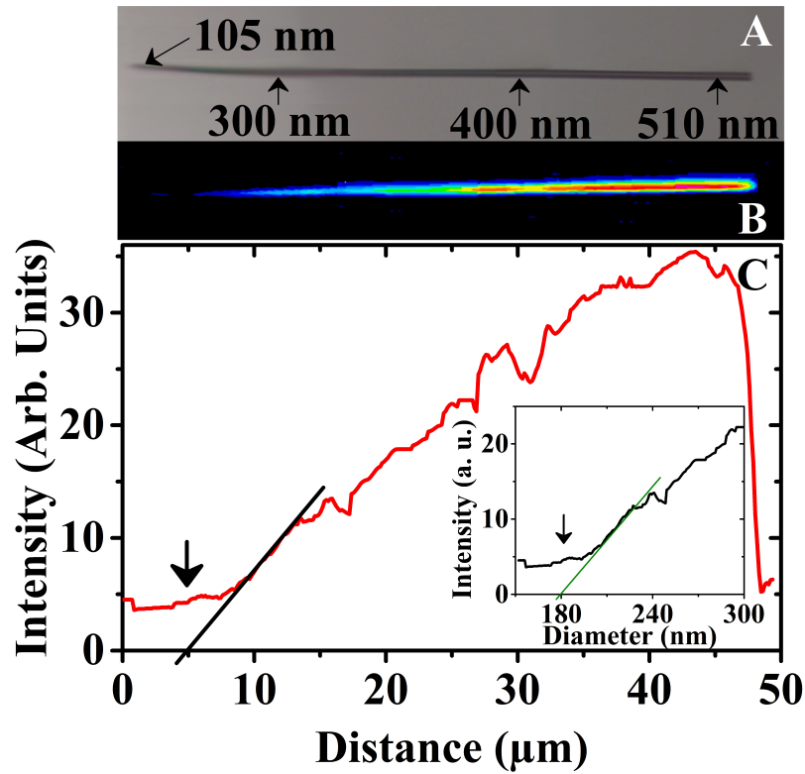


Figure III.7: (a) Panel A shows an image taken at room temperature with an optical microscope of the tip of NW4, for which the diameter increases from left to right. Panel B shows a map along the NW4 of the luminescence at the excitation spot. It is seen that the PL mostly appears at a distance of about  $5 \mu\text{m}$  from the end, as verified using the cross section shown in Panel C. Before this threshold, which corresponds to a NW diameter of 180 nm (insert in Panel C), the NW is entirely depleted. This gives an estimate of the NW donor doping.

This value is in remarkable agreement with the doping level measurements shown in Fig. II.9 of Chapter II and performed using the shape and position of the luminescence line, in which we have seen that a similar NW has a doping level of  $N_D \approx 2.9 \times 10^{17} \text{ cm}^{-3}$ . It will be considered that, since the growth process and conditions are the same, all NWs grown on Si substrates have a n doping level in the low  $10^{17} \text{ cm}^{-3}$  range.

On the other hand, HVPE-grown GaAs NWs on GaAs substrates show a residual p-type behavior, whose origin is not known in detail. The doping level was determined independently by electrical characterization. The experimental setup and the method used are not presented here but can be found elsewhere [171, 172, 173]. The obtained values are  $N_A \approx 3.3 \times 10^{17} \text{ cm}^{-3}$ . The results were similar to those obtained on other NWs grown under similar HVPE growth conditions.

### III.5.2 Expected specificities of NWs on Si substrates

The n-doping level estimated in the last section allows us to expect four outstanding properties of NWs grown on Si(111) substrates, which we summarize here:

(i) **Charge transport mostly concerns electrons and holes and not excitons**, since as shown by Shah *et al.* [174], the electron-hole electrostatic interaction is screened by the background charge (donors or dark electrons) as soon as  $N_D \gtrsim 10^{16} \text{ cm}^{-3}$ , thus quenching the exciton peak in the absorption spectrum.

(ii) **The NWs are metallic.** Indeed, the doping level for the insulator-metal transition, given in 3 dimensions by  $N_D^{1/3} a_0^* = 0.25$ , where  $a_0^* = 100 \text{ \AA}$  is the Bohr radius, corresponds to  $N_D \sim 10^{16} \text{ cm}^{-3}$ , that is, one order of magnitude smaller than the NW doping level. [175]

(iii) **The system must be considered disordered.** The statistical spatial fluctuations of donor concentration give rise to spatial fluctuations of the bottom of the CB and the top of the VB [176, 177]. In a sphere of radius  $R$ , the donor concentration  $n_d = \frac{4}{3}\pi R^3 N_D$  has a typical fluctuation  $\delta n_d = [n_d]^{1/2}$ , which generates a potential  $\frac{q}{\epsilon\epsilon_0} \delta n_d \frac{1}{R}$ . These fluctuations are illustrated in Fig. III.8 for an undepleted NW, i.e. of radius larger than  $w_{SCR}$  given by Eq. III.18, and the present simple approach shows that their magnitude is of the order of the donor binding energy 6 meV.

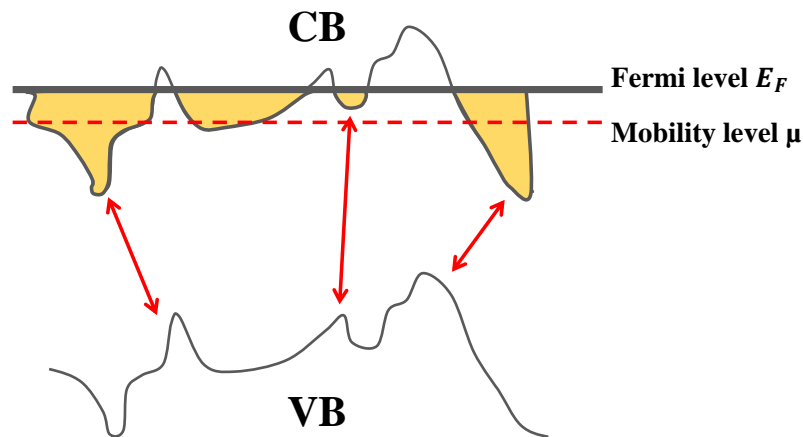


Figure III.8: A schematic representation of the expected NW band structure induced by statistical fluctuations of donor concentrations. The fluctuations are filled up to the Fermi level. The mobility level  $\mu$  is represented by a dashed red line. [177, 176]

The occurrence of metallicity implies that the Fermi level lies above the mobility level, which characterizes the level above which the electrons are mobile. Therefore, in addition to the usual transitions of near band-to-band energy, other transitions between localized states may occur (represented by red arrows in Fig. III.8). These transitions are indirect in the real space and form a PL tail of energy smaller than the bandgap.

(iv) **The absence of intrinsic holes strongly decreases the efficiency of spin relaxation.** As shown in Fig. III.9 [178], the doping level is close to the one of which the spin relaxation time is maximum at LT. A spin relaxation time  $\tau_s$  of 10 ns is expected for  $N_D \sim 10^{17} \text{ cm}^{-3}$ . As a result, these NWs are supposed to be nearly optimal for spin transport.

The following sections contain an investigation of unpassivated NWs, NWs passivated with hydrazine solution and NWs passivated using plasma treatment.

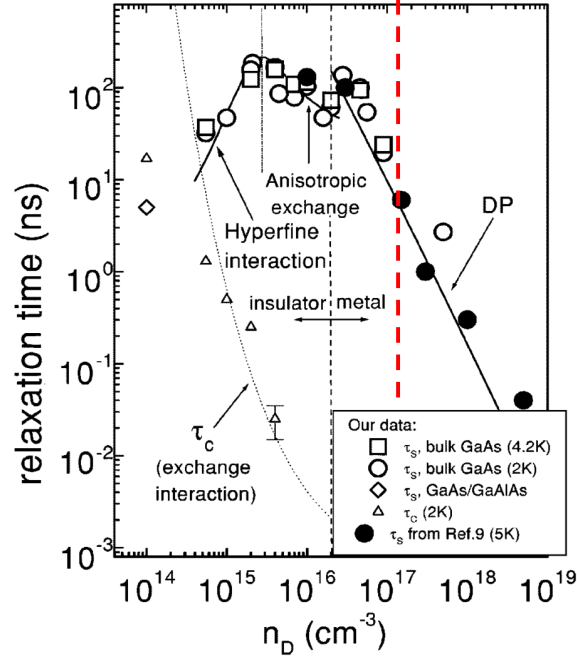


Figure III.9: Spin-relaxation time (called here  $\tau_s$ ) as function of donor concentration in *n*-GaAs. The red dashed line represents the *n*-doped NWs grown on Si(111) substrates studied in this work, which have a doping level in the low  $10^{17}$  range. Solid lines: theory. [178]

## III.6 Unpassivated NWs

In this section, we will present some results obtained on unpassivated GaAs NWs grown on GaAs (100) and Si(111) substrates by HVPE.

### III.6.1 Unpassivated NW on GaAs (100) substrate (NW1)

The results presented here are typical of attempts performed before my thesis work [85]. Fig. III.10-a shows the luminescence intensity for NW1 (red curve) taken at  $T = 6$  K with an excitation power of  $P_{exc} = 45 \mu\text{W}$ .

Besides the near band gap emission, a second peak represents carbon (C) acceptors which are reported to have a binding energy of 26 meV in GaAs and give rise to an emission near 1.49 eV [179, 180]. As seen in the red curve of the same figure, the luminescence degree of polarization has a relatively low value. This is because the exchange interaction with holes in the NW (Bir-Aronov-Pikus (BAP) mechanism [181]) reduces the spin relaxation time of photoelectrons.

Concerning diffusion, Fig. III.10-b shows that the charge profile coincides with the laser one, with a very slight broadening attributed to the very low diffusion of electrons out of the excitation zone. This implies that the diffusion length is smaller than the radius of the laser profile ( $0.6 \mu\text{m}$ ) and that, since the polarization  $\left(\frac{I_{diff}}{I_{sum}}\right)$  is very low, the spin diffusion length is even smaller.

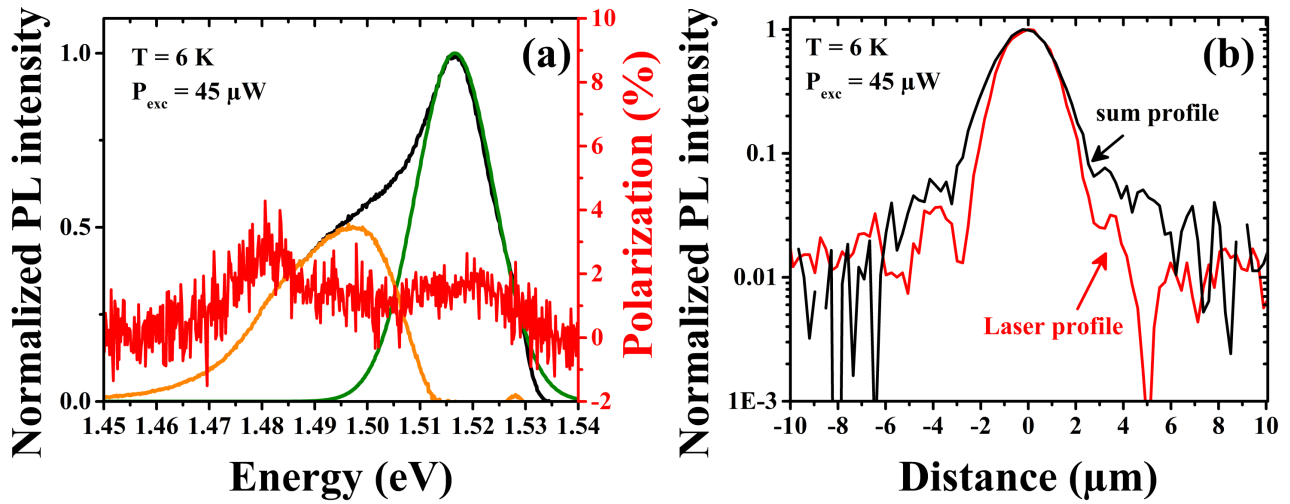


Figure III.10: (a) Spectrum of the luminescence intensity for NW1 (black curve), and the corresponding degree of circular polarization (red curve). From the decomposition of the PL spectrum, we can see clearly the acceptors contribution (orange curve) with the near bandgap transitions (green curve). (b) shows the energetically integrated sum profile (black curve) along with the excitation laser profile (red curve).

### III.6.2 Unpassivated NW on Si(111) substrate (NW2)

The replacement of the GaAs substrate by a Si substrate has several consequences shown in Fig. III.11, which we detail now:

(i) As expected because of the absence of holes in the dark, the polarization is now increased by a factor of about 3.

(ii) There appears a weak PL tail going to very low energy, caused as shown in Fig. III.8 by indirect transitions in real space.

(iii) In terms of transport, Fig. III.11-b shows that the charge as well as the spin diffusion lengths are larger than the radius of the laser spot. This fact is not understood in detail and can originate from the mobility or from the overall lifetime of minority carriers. Time-resolved experiments (in progress) would be necessary to elucidate this point. We obtain  $L_c^* \approx 1.64 \mu\text{m}$  and  $L_s^* \approx 1.34 \mu\text{m}$  for charge and spin, respectively. From these values, we are able to estimate the charge lifetime  $\tau_c$  using the following equation:

$$\frac{L_s^{*2}}{L_c^{*2}} = \frac{T_1}{T_1 + \tau_c} \quad (\text{III.20})$$

and taking  $T_1 = 10 \text{ ns}$  [178], we find  $\tau_c \approx 5 \text{ ns}$  and  $D_e \approx 53 \text{ cm}^2/\text{s}$ .

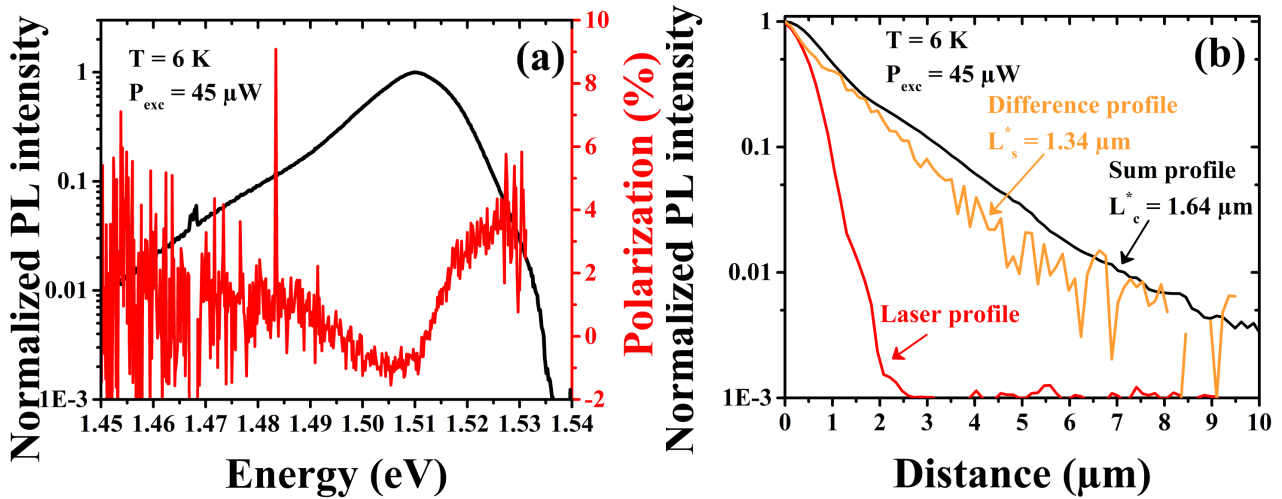


Figure III.11: (a) PL spectrum for NW2 (black curve), and the corresponding degree of circular polarization (red curve). (b) Energetically-integrated sum (black curve) and difference (orange curve) profiles, along with the excitation laser profile (red curve). The  $P_{exc}$  is  $45 \mu\text{W}$  and the temperature is  $6 \text{ K}$ .

## III.7 Hydrazine passivated NWs

### III.7.1 Principle of hydrazine passivation

Wet chemical treatment with hydrazine-sulfide solutions is known to be very efficient for improving surface optical properties of GaAs [182].

This chemical treatment consists in adding to the hydrazine solution ( $\text{N}_2\text{H}_4$ ) a small amount of sulfide  $\text{Na}_2\text{S}$ , which results in forming an alkaline solution that removes surface As atoms. The remaining Ga atoms are then doubly-bonded with N atoms in the solution in a robust bridge configuration [183, 184]. However, the conventional solution is highly alkaline ( $\text{pH} \approx 12$ ) and causes a microetching of the surface [185, 184]. To reduce this effect and prevent the degradation of NW properties, this solution has been diluted to a  $\text{pH} \approx 8.5$  using a hydrazine chloride solution  $\text{N}_2\text{H}_5\text{Cl}$ . A pioneer work was published recently [186], in which the efficiency of this method for protecting GaAs NWs grown by MBE has been reported.

### III.7.2 Hydrazine passivated NW on GaAs (100) substrate (NW3)

Let us consider a p-doped NW similar to that presented in section III.6.1 but passivated with hydrazine. The excitation power  $P_{exc}$  is equal to  $140 \mu\text{W}$  for this experiment. The PL spectrum in Fig. III.12-a shows a very similar behavior as the unpassivated NW (Fig. III.10), except that the relative intensity of the acceptor tail is lower. This behavior, which is common in p-type GaAs crystals, is attributed to the larger value of the photoelectron concentration due to which the near bandgap, bi-

molecular recombination, occurs preferentially with respect to the acceptor-related, monomolecular one.

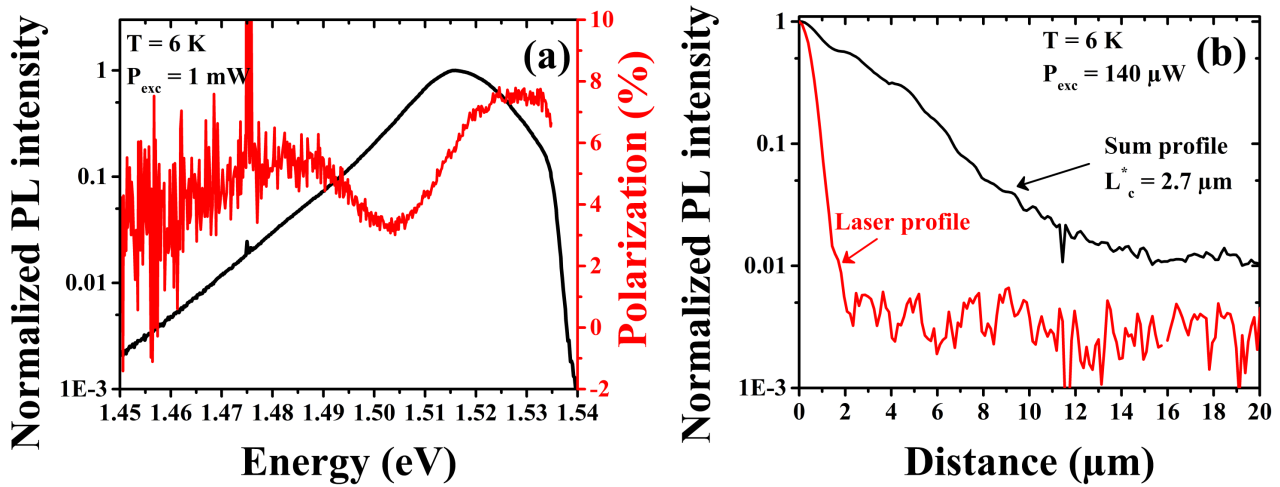


Figure III.12: (a) Spectrum of the luminescence intensity for NW3 (black curve), and the corresponding degree of circular polarization (red curve). (b) shows the energetically integrated sum profile (black curve) along with the excitation laser profile (red curve).

The main difference between the unpassivated and the passivated NW is the increase of the effective diffusion length (from 1.64 to 2.7  $\mu\text{m}$ ) caused by the decrease of surface recombination. As a result, an exponential decay profile is observed, in agreement with Eq. III.14, of effective diffusion length  $L_c^* = 2.7 \mu\text{m}$ , to be compared with the value of 1.64  $\mu\text{m}$  for the the unpassivated NW.

Note finally that, because of the efficient spin relaxation induced by holes due to the BAP mechanism [181], the spin diffusion length is still small, so that the spin spatial profile (not shown) cannot be resolved from the laser profile.

### III.7.3 Hydrazine passivated NW on Si(111) substrate (NW4)

In this section, we present the tapered n-doped NW passivated with hydrazine used for doping level measurements (NW4). We study here this NW on its large side, where the diameter is equal to 500 nm and constant over the whole luminescence spatial profile. This implies that the NW is not depleted and, in the dark, an electronic density is present in the CB. Most importantly, this means that the localized states in the CB, as shown in Fig. III.8, are partly or fully filled even at low  $T$  before any excitation. We will see later the impact of this level filling.

The PL spectrum with the luminescence polarization spectrum are shown in Fig. III.13-a. The degree of circular polarization shows a large enhancement compared to the n-doped unpassivated NW (Fig. III.11). A value of 10 % is obtained for high energies while it is reduced to  $\sim 5$  % for the low energy tail.

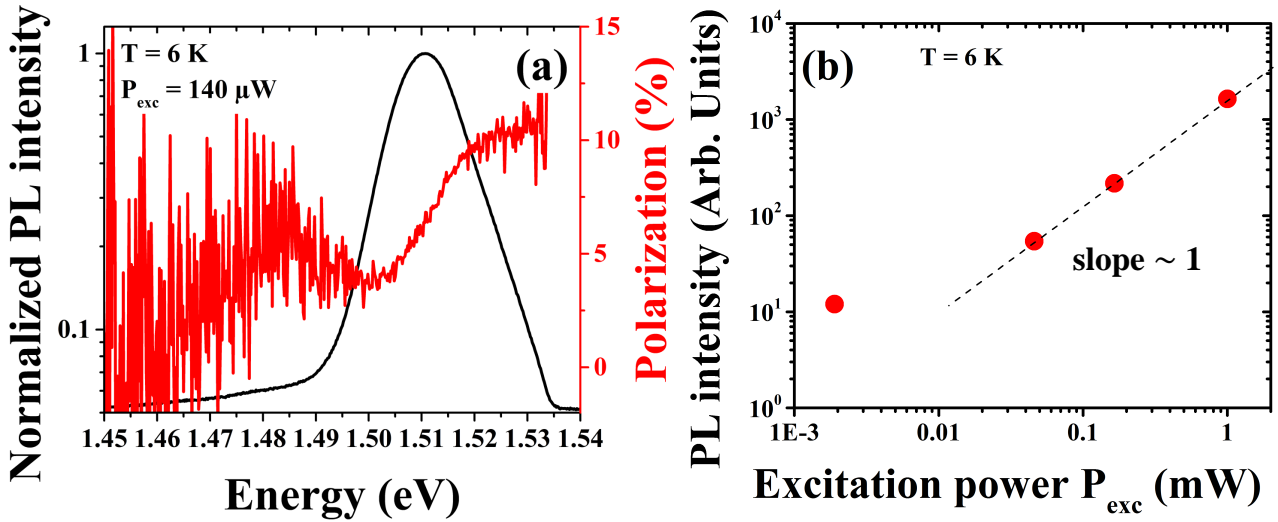


Figure III.13: (a) PL spectrum for NW4 (black curve), and the corresponding degree of PL circular polarization (red curve). The excitation power is  $P_{exc} = 140 \mu\text{W}$ . The studied part of the NW is the large one, where the diameter is equal to 500 nm. (b) The luminescence intensity as function of  $P_{exc}$  shows a linear behavior for an excitation power larger than  $50 \mu\text{W}$  and a power law of exponent  $\sim 1$  below. This implies that the bimolecular recombination is not effective in this NW.

Fig. III.13-b shows the dependence of the maximum of PL intensity on  $P_{exc}$ , which is found linear. Since the band-to-band recombination is described by the third term of Eq. III.17, this linear behavior suggests that, for the whole range of excitation powers, photocreated electrons are less numerous than dark electrons. Therefore, the hole recombination time is not modified by light excitation.

Fig. III.14 shows the normalized spatial profiles integrated over all the energy range considered. Talking about the positive distances, both the sum (black) and difference (orange) profiles exhibit two regimes: a relatively fast decay within a distance of  $2 \mu\text{m}$ , and a much slower decay characterized by a charge diffusion length  $\approx 5.7 \mu\text{m}$  and a slightly smaller spin diffusion length  $\approx 5.2 \mu\text{m}$ .

As seen before, the rapid decay shown in Fig. III.14 is not observed either on oxidized NW grown on Si substrate or on NWs on GaAs substrates (see section III.6.2), and is therefore characteristic of passivated NWs on Si substrates. The characteristic lengths for charge and spin transport, both above  $5 \mu\text{m}$ , constitute record values for NWs.

For negative distances, the NW end is reached at a distance of  $-6 \mu\text{m}$ , beyond which we observe an excess of luminescence intensity. To make sure that it is not a manifestation of an artefact, we have done the same measurement but closer (at  $2 \mu\text{m}$ ) to the NW end. Fig. III.14-b shows, on its negative side, that this excess of light becomes closer to the excitation zone, revealing that it is a real signal. This suggests a light channeling inside the NW until extraction at its end.

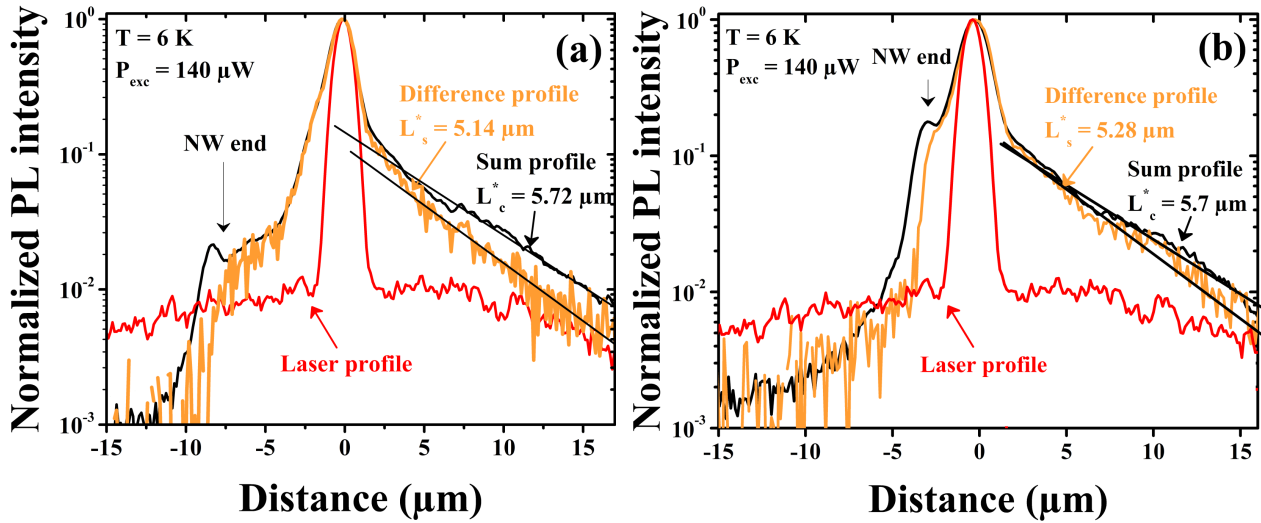


Figure III.14: The spectrally-integrated profile at  $6 \mu\text{m}$  from the edge of NW4 is given in (a). We can see the rapid decrease followed by a slower one for both sum (black) and difference (orange) profiles. The excitation laser profile is represented in red. The  $P_{\text{exc}}$  was  $140 \mu\text{W}$ . The light excess at  $-6 \mu\text{m}$  occurs near the NW end and suggests that a light channeling takes place in the NW. Shown in panel (b) are the spatial profiles with a laser excitation at  $2 \mu\text{m}$  from the NW end, and reveal as expected a signal excess near  $-2 \mu\text{m}$ .

Before interpreting the spatial profiles, it is important to exclude some possible explanations that can be confusing:

(i) **The rapid decay for a distance smaller than  $\sim 2 \mu\text{m}$  does not originate from convolution of the PL and the laser profiles [as shown in Eq. III.13].** We may simply relate the rapid decay at small distances to the convolution of the Green function, of typical decay length of  $5.7 \mu\text{m}$ , with the narrow Gaussian profile of the excitation laser (see Eq. B.18 in Appendix B.1). However, such a convolution results in an exponential decay equivalent to the Green function in terms of width [157].

(ii) **The channeling of the luminescence light does not affect the spatial profiles.** Because the high refractive index of GaAs, only photons with an angle  $< 15^\circ$  with the surface normal can be extracted from the NW. The other photons undergo total reflexion, and are responsible for the PL excess near the NW end shown in Fig. III.14. Photons are reabsorbed after a typical length  $1/\alpha \sim 3 \mu\text{m}$  and generate new electron-hole pairs, which can subsequently emit a photon, and so on [187] (see Fig. III.15). A simple calculation shows that the resulting spatial profile is composed of two exponentials, of length  $1/\alpha$  and  $L_c^*$  respectively. However, whenever this cycle occurs, and as seen from Eq. III.1, the electronic polarization should be multiplied by  $P_i$ , i.e. reduced by a factor 2. This leads to an expected decrease of the difference profile much more rapid than that of the sum, which in contradiction with Fig. III.14. It is concluded then diffusion in the NW is more efficient than light channeling to transport carriers.

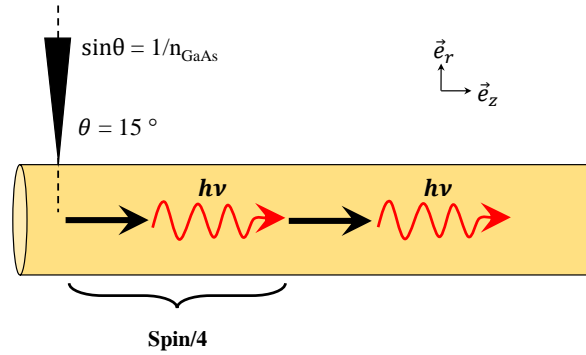


Figure III.15: A simplified representation of the photon recycling process, showing that the spin must be reduced by a factor 4 after a generation/recombination process.

(iii) **Absence of laser coupling into an optical mode of the NW.** In order to see if the excess of signal at the end of the NW is due to channeling of the laser light, we have excited the NW at two distances from the edge and analyzed the spatial profiles at the laser energy. As seen in Fig. III.16, the profiles, which exhibit Airy rings for the particular laser focusing used, are nearly identical, with no structure following the NW end. This means that the laser is not guided in the NW and therefore only excites electron-hole pairs at the place of focusing.

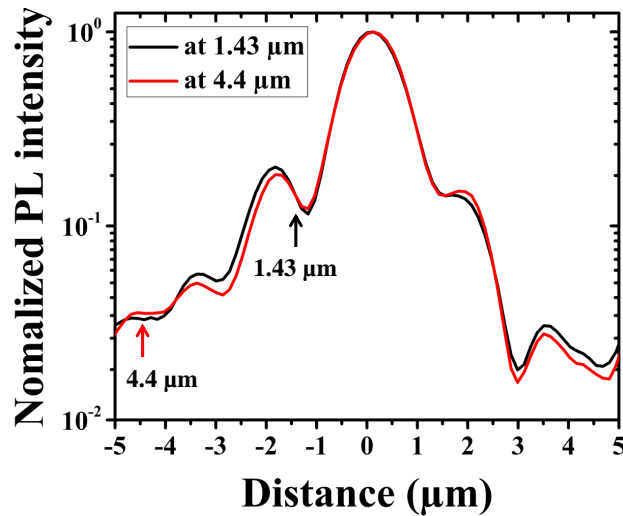


Figure III.16: Spatial profiles at the energy of the laser, for an excitation at two different distances from the NW's edge. The perfect coincidence between the two profiles indicates that the laser is not guided in the NW.

(iv) **Spatial modes of higher order.** It has been shown above and discussed in Appendix B.1 that the spatial profile is a sum of spatial modes. However, the steep signal observed near  $r = 0$  cannot be due to a spatial mode of high order since higher order modes are relatively more important if surface recombination increases. Thus, this signal should be more visible for the unpassivated NWs, which is not the case. This is also in agreement with estimates given in Appendix B.1.

Before interpretation of these results, we present in the next section the results obtained on  $N_2$  plasma passivated NWs.

## III.8 N<sub>2</sub> Plasma passivated NWs on Si(111) substrate (NW5)

Another powerful technique for surface passivation is to use a nitrogen plasma inside a UHV chamber. This technique is known to be softer and more controllable than chemical ones. In this section, we present this method and its impact on the properties of NWs.

### III.8.1 N<sub>2</sub> Plasma passivation process

The passivation of GaAs surfaces using N<sub>2</sub> plasma has been studied at Institut Pascal for several years. Many interesting results have been reported on GaAs planar surfaces showing a real luminescence enhancement. A increase of the PL intensity by a factor  $\sim 10$  has been obtained after passivation, along with a good stability in time [9].

A GaAs surface is first cleaned using the process reported by Tereshchenko et al. consisting in a treatment by HCl isopropanol at RT [188]. This process is known to reduce the surface damage as compared to ion etching. Following the cleaning step, the samples are immersed in ultrahigh purity isopropyl alcohol and then quickly introduced into the UHV to avoid any contamination.

We use a plasma produced by a commercial electron resonance cyclotron source (SPECS MPS-ECR), which works mainly in atom beam mode at pressures of  $10^{-2}$  Pa and  $2.5 \times 10^{-3}$  Pa with a low residual current density around  $10 \text{ nA.cm}^{-2}$ . We have reported recently an experimental study on the passivation kinetics of (100) GaAs layers [9]. Very briefly, the process is summarized as follows. The N atoms reach the sample surface with perpendicular incidence where they are adsorbed at vacant sites. Once adsorbed, they enter in the GaAs matrix and start filling the interstitial sites. This results in a weakening of the Ga-As bonds until they are dissociated and replaced by Ga-N. The free arsenic atoms migrate towards the surface where they are accumulated or desorbed if they possess enough energy (at sufficiently high temperature). Therefore, the sample temperature during the nitridation can play an important role in this process, first, to promote the diffusion towards the surface of the released As atoms until desorption, and second, to help the N atoms to diffuse into the GaAs matrix. The best results in terms of PL intensity of planar GaAs (100) surface have been obtained after a passivation of 1 hour at RT, followed by an annealing at 620 °C for 1 hour.

In the case of NWs, the chemistry of passivation may depend on surface orientations. We have seen that GaAs NWs grown by HVPE along the  $\langle 111 \rangle_B$  direction, forming then (110)- with some  $(1\bar{1}2)$ -oriented lateral facets. The mechanisms involved in the passivation of such surfaces are yet to be investigated.

In order to reduce any shading effect, the passivation of NWs standing on their growth substrates was performed at two different incident angles ( $+ 45^\circ$  and  $- 45^\circ$  with respect to the normal incident angle) by rotating the substrate during nitridation. We used the same process as for a planar layer (1 hour of passivation for each side) and we assume that the annealing of the rear face of the substrate results in a homogeneous temperature along the NW.

### III.8.2 Plasma passivated NWs

Now we discuss the results obtained on a plasma-passivated NW at RT for 2 hours (1 hour at  $+45^\circ$  and 1 hour at  $-45^\circ$ ) without annealing. This sample has shown very good features in terms of diffusion and resolution of the PL spectra, as compared to the annealed one (not shown here). This NW was grown on Si(111) substrate, so has an initial n-doping level in the low  $10^{17} \text{ cm}^{-3}$  range.

Fig. III.17-a shows PL spectra taken at  $T = 6 \text{ K}$  with excitation powers varying from  $8 \mu\text{W}$  to  $1 \text{ mW}$ . Also shown on the same figure, for comparison, the PL spectrum after hydrazine passivation, identical to the one shown in Fig. III.13-a. The differences between the two samples are immediately apparent. Firstly, the PL spectrum after plasma passivation has smaller linewidths than after hydrazine treatment. This may be due to a residual etching caused by the hydrazine solution, thus causing surface roughness of the NW. Secondly, the plasma treatment induces significant acceptor peaks, mostly due to the carbon acceptor at  $1.49 \text{ eV}$  and its LO phonon replicas at  $1.46$  and  $1.42 \text{ eV}$ . This reveals a partial compensation of the Si donors by C acceptors, for which the mechanism is not understood in detail.

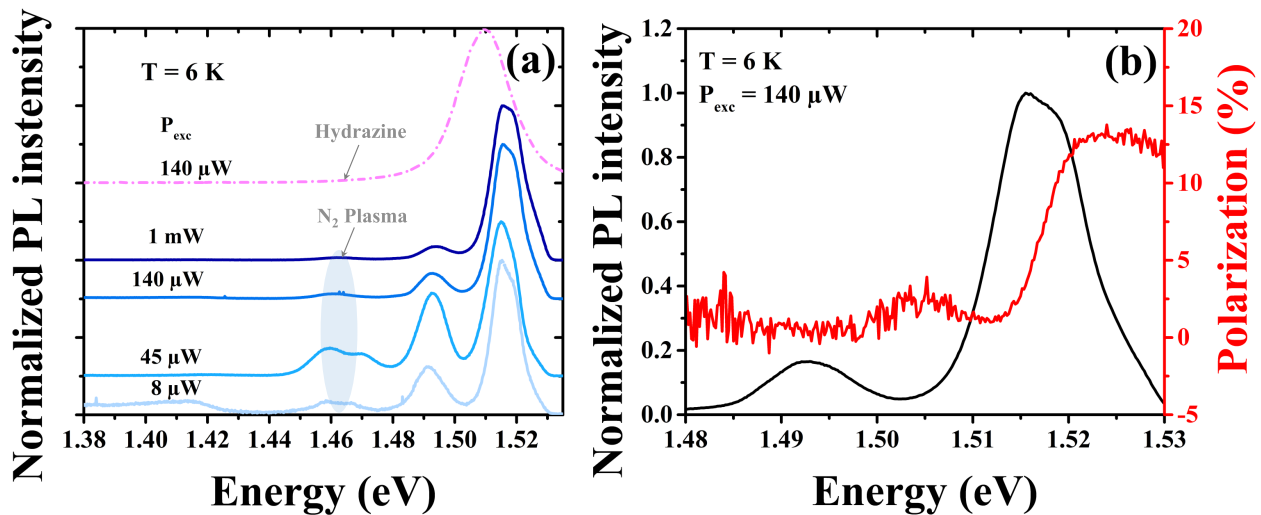


Figure III.17: (a) PL spectra at 6 K of a GaAs NW (NW5) grown on Si(111) substrate and passivated by  $\text{N}_2$  plasma (blue curves) and the hydrazine-passivated NW4 (pink dashed curve). The excitation power was varied between  $0.008$  to  $1 \text{ mW}$  for the plasma-passivated and fixed at  $140 \mu\text{W}$  for the NW passivated with hydrazine. Panel (b) shows the PL spectrum (black curve) in a restricted spectroscopic range with the corresponding degree of circular polarization (red curve) of the plasma-passivated NW taken at 6 K with  $P_{\text{exc}} = 140 \mu\text{W}$ .

Fig. III.17-b shows the polarization spectrum in a restricted energy range for  $P_{\text{exc}} = 140 \mu\text{W}$ , along with the PL spectrum in the same conditions. This figure exhibits a large spin polarization of hot electrons, together with a strongly-reduced one on the low energy side of the main line. These results are fully comparable with those of hydrazine passivation (Fig. III.13), rather than ones on GaAs substrates (Fig. III.12), thus suggesting that the increase of carbon concentration has not completely

compensated the donors. Note finally the structure in the PL spectrum, which may be caused by a slight stress resulting in a removal of the light hole/heavy hole degeneracy.

The PL intensities of the two NWs are now compared. Fig. III.18 shows for several excitation powers, the spectrally integrated PL intensities of the two samples normalized for the NW radius  $r_0$  using Eq. III.19 in which the first term is taken dominant because of the reduced surface recombination. It is seen that, in agreement with the quality of the spectra, the plasma-passivated NW has a lumines-

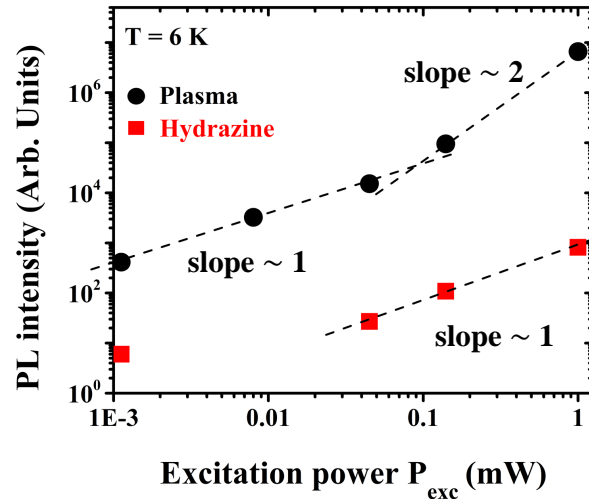


Figure III.18: The dependence of the PL intensity on the excitation power for plasma- (black points) and hydrazine- (red squares) passivated NWs. The linear behavior of slope  $\sim 1$  seen for the hydrazine passivated NW suggests a monomolecular regime implying that photoelectrons are less numerous than intrinsic electrons. For the plasma-passivation, because of the smaller concentration of intrinsic electrons, we observe a change of the slope from  $\sim 1$  to  $\sim 2$  revealing that a bimolecular regime prevails at high excitation powers (see section III.4.2.2)

cence intensity more than 1 order of magnitude larger than the hydrazine-treated one. Moreover, the hydrazine-treated surface reveals a slope of value unity, suggesting a monomolecular regime in which photoelectrons are less numerous than intrinsic electrons. The dynamics on plasma-passivated NW evolves from a slope 1 ( $P_{exc} \leq 0.04$  mW) to a bimolecular regime revealing that photoelectrons are more numerous than intrinsic electrons for excitation powers larger than 0.04 mW. This distinct behavior is directly related with the decrease of the concentration of intrinsic electrons caused by partial compensation of the Si donors by carbon acceptors. For the hydrazine-passivated NW, because of the larger concentration of intrinsic electrons, a monomolecular regime prevails.

In spite of these differences, the hydrazine- and plasma-passivated NWs exhibit very similar charge transport properties. The PL sum profile of the plasma-treated NW, shown in Fig. III.19, also exhibits a fast decrease near the laser excitation spot, with a rather slow tail characterized by a large diffusion length of  $\sim 6 \mu\text{m}$ . Since the photoelectron lifetime is probably larger than for hydrazine treatment, this may indicate a slightly smaller diffusion length, caused by a smaller mobility. The spin diffusion length, of about  $\sim 3 \mu\text{m}$ , is slightly smaller than for hydrazine passivation ( $L_s^* \sim 5 \mu\text{m}$ ).

This is in agreement with the above speculation suggesting a smaller diffusion constant.

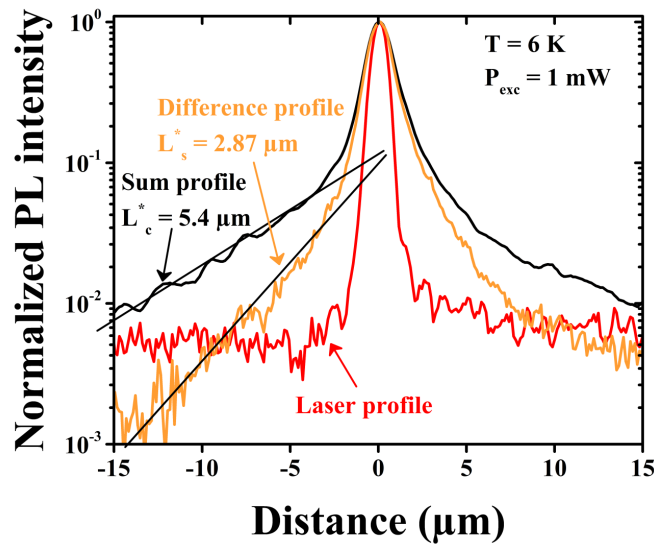


Figure III.19: The energetically integrated profile of NW5. Similar to NW4 passivated with hydrazine, the charge and spin profiles show a rapid decay at small distance followed by a slower one at large distances. The  $P_{exc}$  was 1 mW.

Up to now, more experimental data are available for the hydrazine-treated NWs than  $N_2$  plasma-passivated ones. Therefore, in spite of the slightly smaller efficiency of passivation, we choose to show in the following section only results obtained with hydrazine passivation assuming that they are representative for charge and spin transport.

### III.9 The nature of charge and spin transport in NWs grown on Si(111)

The spatial profiles of passivated NWs grown on Si substrates (Figs. III.14 and III.19) exhibit common features which contradict the predictions of the diffusion equation (Eq. III.14), according to which the decay is composed of a single exponent. Namely, the spatial profile is composed of 3 phases. There is first a rapid decay in the first 2  $\mu\text{m}$  followed by a nearly exponential phase, up to about 10  $\mu\text{m}$ . A third phase, shown in Fig. III.14-b, exhibits a more rapid decay for distances larger than about 10  $\mu\text{m}$ .

Here we limit ourselves to more detailed qualitative experimental analysis, aiming at clarifying the main aspects of charge and spin transport.

A key aspect of this investigation is to compare the results with those of a depleted NW, i.e. as seen from section III.5.1, a NW for which the diameter is smaller than  $\sim 180$  nm. The transfer to surface states removes all intrinsic electrons from the NW and therefore decreases the Fermi level position, as shown in Fig. III.8, to a value lower than the lowest fluctuations of the CB position. Because of this depletion, it is expected that photoelectrons occupy the fluctuations of the lowest energy, which should strongly slow down hopping transport in the disordered system.

Spatially-unresolved investigation of NW6, of diameter 90 nm, is shown in Fig. III.20. The PL spectrum is quite similar to that of Fig. III.13. A significant difference is the fact that a negative polarization appears near 1.50 eV. This might be attributed to a residual stress in this thin NW, due to which heavy and light hole states are no longer degenerate. As seen in Fig. III.1, a negative polarization is a signature for recombination with light hole states [189].

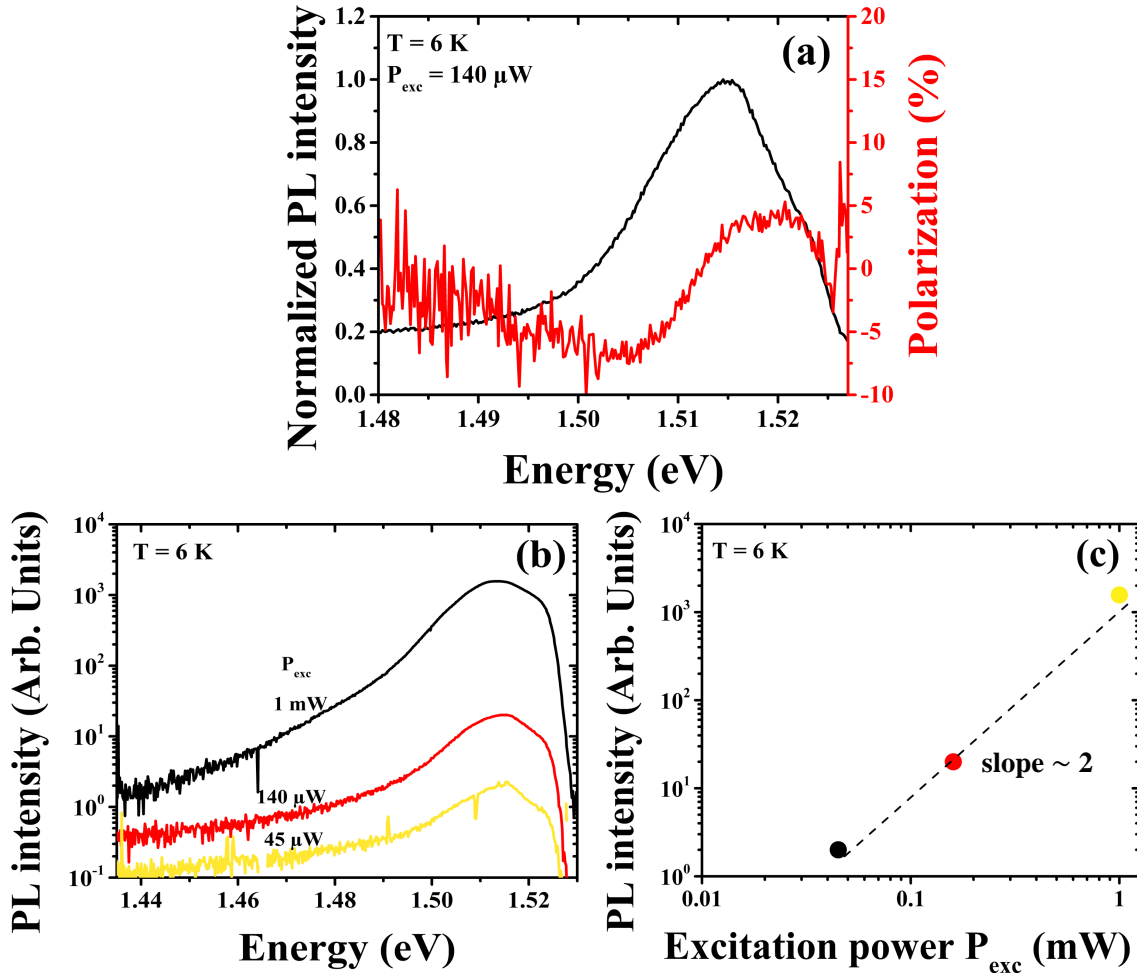


Figure III.20: (a) Luminescence spectrum for the depleted NW6 (diameter  $\sim 90$  nm) in black along with the corresponding degree of polarization in red. Also shown in panel (b) the PL spectrum at different excitation powers taken at  $T = 6$  K on the same NW. The luminescence intensity as function of  $P_{exc}$  is plotted in panel (c). It shows a linear behavior of slope  $\sim 2$  which means that the bimolecular recombination process is effective because of the absence of intrinsic electrons.

The NW depletion is revealed by two distinct features. Firstly, since photocarriers thermalize to the bottom of spatial fluctuations, we observe, as seen in Fig. III.20-b, strongly enhanced PL tails at low energy extending as low as 1.44 eV. Secondly, since there are no carriers in the dark, recombination occurs between photoelectrons and photoholes without participation of intrinsic carriers ( $n_0 \gg N_D$  in III.17) and therefore has a bimolecular character, as shown in Fig. III.20-c which manifests itself by a slope 2.

Figure III.21 shows a comparison of the spatial profiles between NW7 and NW6. The topline

(Panels (a) and (b)) shows the spatial charge profiles at the luminescence peak (1.510 eV), as well as on the high energy side (1.525 eV) and on the low energy side (1.48 eV) of this peak. In the framework where transport occurs by hopping, it is anticipated that PL at higher energy takes place from carriers situated higher in the fluctuations, for which transport by hopping should be easier [190, 191, 192]. The results are in strong contradiction with this picture, since the spatial profiles very weakly depend on energy in the spectrum, nor on diameter.

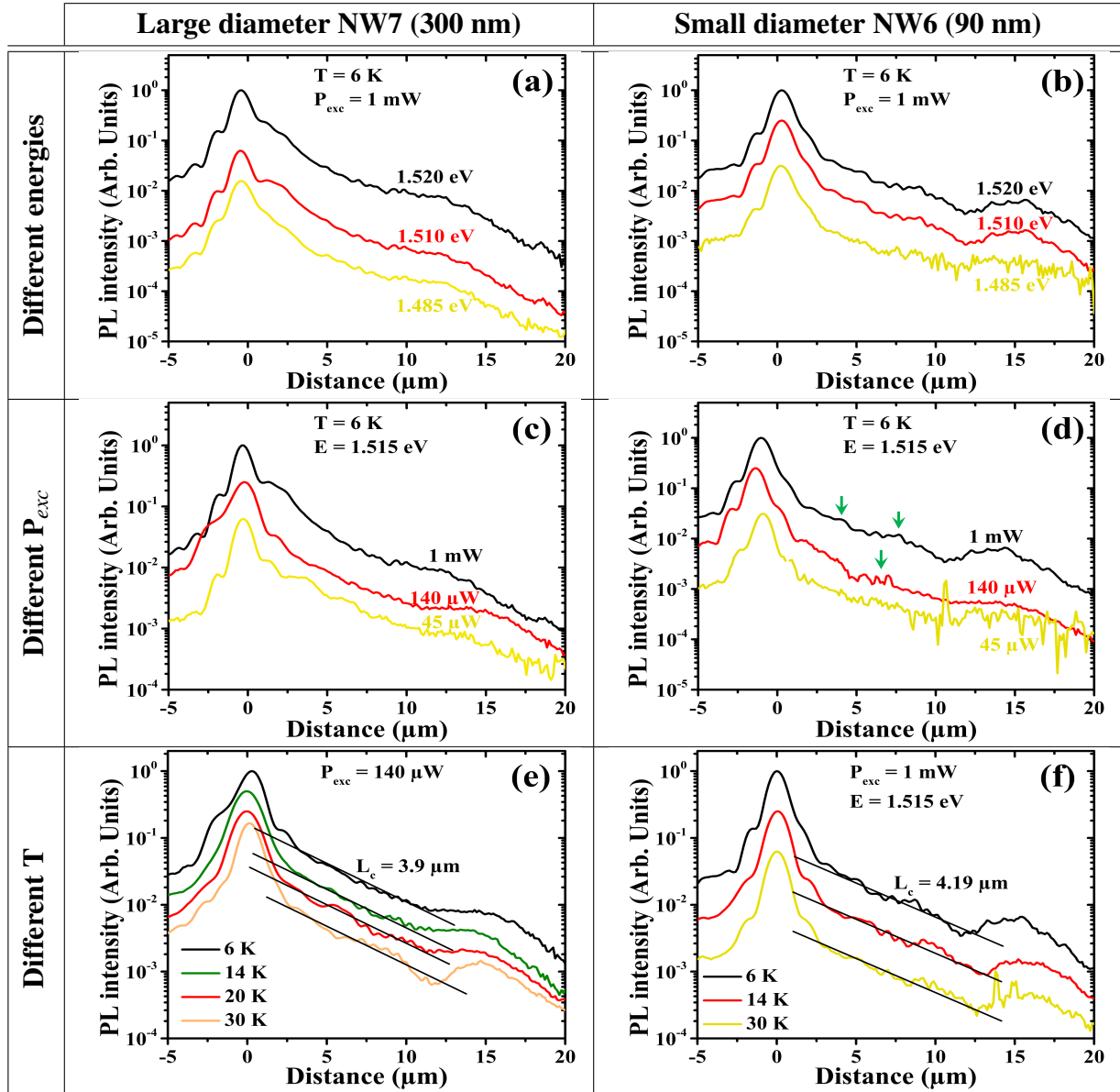


Figure III.21: Spatial profiles for NW7 (left column) and NW6 (right column) at different energies (line 1), excitation powers  $P_{exc}$  (line 2) and temperatures (line 3). Despite the known impact of these parameters on the band filling, the profiles do not show any change. This suggests that the transport at  $2\mu\text{m} < z < 10\mu\text{m}$  is likely to occur by diffusion of hot carriers above the potential spatial fluctuations. At small distance ( $z < 2\mu\text{m}$ ), the rapid decay that appears in the profiles is related to the surface photovoltage effect. This latter leads to an accumulation of carriers at the center which results in an increase of the luminescence intensity.

In the same way, an increase of excitation power should lead to a band filling effect leading to a more efficient transport by hopping. However, as shown by panel (c) and (d) of Fig. III.21, this hypothesis is contradicted by the lack of effect of the increase of excitation power for two NWs. Finally, while a temperature change is known to have a strong effect on the resistivity of disordered systems, again, an increase of  $T$  has little effect on the spatial profiles of the two NWs [175].

These results lead us to the conclusion that the spatial profiles do not reflect transport by hopping or by tunneling across potential barriers. We propose here an explanation according to which the spatial profiles are due to hot electron transport, as illustrated in Fig. III.22. In this picture, diffusive or hopping transport of localized carriers is negligible and they recombine locally. Thus, luminescence at a distance  $z$  originates from hot carriers having diffused and emit light after local thermalization.

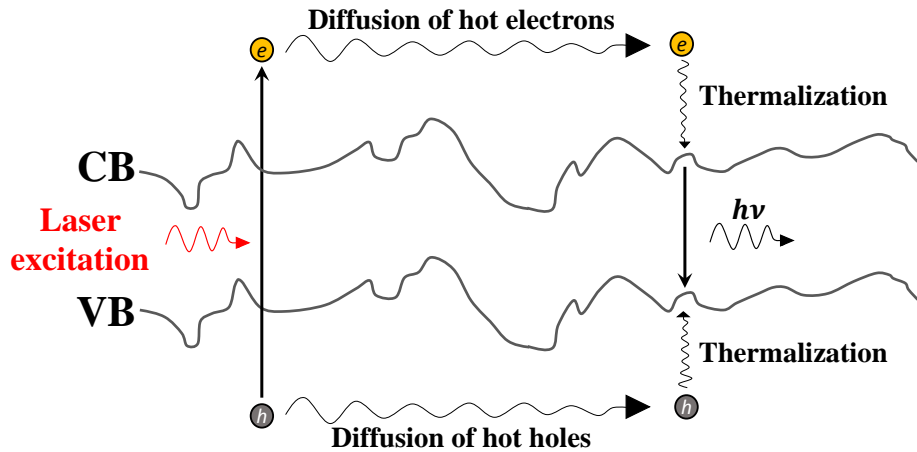


Figure III.22: Schematic representation illustrating the transport mechanism in GaAs NWs grown on Si substrates. After an external laser excitation, hot carriers are created in the VB and the CB. They diffuse above the potential spatial fluctuations until thermalization to the lowest energy states, where a radiative recombination takes place.

We now discuss the possible origin of the rapid decay for distances smaller than  $2 \mu\text{m}$ . Because of the known fast thermalization of photoholes [193], it seems natural that a strong photocarrier trapping occurs at the excitation spot. This results in a space charge, at the NW surface or in the fluctuations which, as shown in Appendix B.3, strongly slows down outward diffusion of minority carriers, provided that the photovoltage magnitude is larger than  $k_B T / |q|$  where  $k_B$  is the Boltzmann constant. Here no strong effect of excitation power is observed. This is also the case in bulk material, where it has been attributed to a change of surface density of states induced by Fermi level unpinning [168].

The second phase of the spatial profiles, between  $2 \mu\text{m}$  and about  $10 \mu\text{m}$ , gives the common ambipolar diffusion length of hot electrons and holes, as shown in Fig. III.22, this length is in all cases of the order of  $4\text{--}6 \mu\text{m}$ . As seen from Eq. III.16, and assuming i) that the carrier concentration is smaller than the doping level and ii) that charge neutrality is present, the ambipolar diffusion constant is independent on concentration and equals to  $\frac{D_h \mu_e}{\mu_e + \mu_h}$ . Thus, Eq. III.14 is still valid, with a modified value of the diffusion length. It may seem surprising to obtain such large diffusion lengths for hot

carriers. Note however that, because of the energy dependence of the relaxation time appearing in the mobility [194, 146], the diffusion constant should strongly increase with kinetic energy. A modeling of this dependence using Ref. [146, 147] suggests that the mobility of hot carriers is about a factor of 5 larger than carriers at the bottom of the CB. Note finally that, in this distance range, all the profiles exhibit fluctuations which may appear as being caused by spurious noise. Examples of such fluctuations are shown by green arrows in panel (d) of Fig. III.21. As judged by comparing these profiles with bulk homogeneous material, we believe that these fluctuations rather reflect spatial inhomogeneities of the radiative recombination time of thermalized carriers, caused by the potential fluctuations.

We have at the present time no detailed interpretation for the feature occurring between 12 and 15  $\mu\text{m}$  in all the profiles shown in Fig. III.21. This feature is also present with a similar shape on the spin spatial profiles. This shows that it cannot be attributed to a type of photon recycling process, for the same reason as III.7.3 (iii) above. It is tempting to think that, at this distance, transport no longer occurs via hot electrons but by hopping. This may explain why i) in panel (e) of this figure the magnitude of this signal increases with temperature for NW7 and ii) it seems to depend on NW diameter, as shown by a comparison of panels (a) and (b) at an energy of 1.52 eV, and (c) and (d) at 1 mW. Note finally that simulations of transport of interacting particles [195, 196] do reveal a change of diffusive regime at some distance.

Accurate quantitative interpretation of these results requires modeling of charge and spin diffusion in disordered systems in which there exists a strong screening of the potential spatial fluctuations by mobile charges. This interpretation requires a self-consistent approach in which particles are no longer independent and for which Fick's law is no longer valid. Such interpretation is beyond the scope of this work.

## III.10 Conclusion

In this chapter, we have investigated the luminescence and polarization spectra, as well as the charge and spin transport properties of NWs mostly grown on Si substrates. The role of NW passivation has been shown, with two complementary techniques, namely hydrazine wet chemical passivation and plasma passivation. While plasma passivation appears to be of better quality, as judged from the PL intensity and the width of the PL lines in the spectra, it induces extra mechanisms of spin relaxation which reduces the spin diffusion length.

All passivated NWs grown on Si substrates exhibit similar charge and spin spatial profiles. These profiles are not observed on NWs grown on GaAs substrates. They are also weakly dependent on the NW diameter, the temperature and the laser excitation power.

This remarkable feature strongly suggests that transport mostly concerns hot electrons, i.e. electrons at an energy larger than the potential fluctuations caused by the spatial fluctuations of donor concentration.

We are therefore led to conclude that, in NWs grown on Si substrates, hot electron charge and spin transport occurs over record lengths as large as  $6 \mu\text{m}$ . Moreover, the absence of intrinsic holes in these n-doped NWs results in a very large spin relaxation time, leading to photoelectron spin polarizations as large as 20 % and to spin diffusion lengths almost as large as the charge diffusion lengths.

This investigation opens the way to three types of perspectives. Firstly it is highly interesting to further decrease the NW diameter, in order to investigate quantum wires, where diffusive transport may be replaced by ballistic transport. Secondly, metallic disordered NWs constitute strongly an attractive system of fundamental interest for which transport should be investigated theoretically (using a self-consistent modeling and the landscape theory [197]), and experimentally, by reducing the laser excitation energy in order to generate all electron-hole pairs in the fluctuations.



# General conclusion

**T**HE particularity of this manuscript is the multidisciplinary aspect of the work presented within. It is composed of three chapters covering surface preparation of Si(111) substrates, growth of GaAs nanowires (NWs) investigated experimentally and theoretically, passivation of the NWs surfaces and study of their transport properties. At the beginning, the main purpose of this work was, firstly, to develop the growth of GaAs NWs on Si(111) substrates by HVPE and, secondly, to passivate their surfaces by plasma in order to enhance the charge and spin transport properties. However, these objectives were considerably extended over time.

**Chapter I** consists of three sections. In the first one we presented the potential of the HVPE technique used in Institut Pascal for the growth of nano-structures, especially GaAs NWs. An overview of the literature related to the growth of such structures by other techniques (MBE and MOVPE) is reported, allowing for a comparison with the unique results demonstrated by our group.

The second part addresses the study of the dewetting of ultra-thin gold films on SiO<sub>2</sub>/Si(111) substrate, which is the first step towards the fabrication of NWs. The aim of this study is to better control the distribution of the gold droplets formed after dewetting, which serve as catalyst for NWs growth. We have studied the impact of different parameters on the size distribution and the density of these droplets, such as the thickness of the SiO<sub>2</sub> layer, the impact of annealing after deposition, the effective thickness of the gold film, etc. We have demonstrated that the presence of the SiO<sub>2</sub> layer is necessary for obtaining regular gold nanodroplets, otherwise silicide clusters of irregular shapes are formed. On the other hand, we have shown that annealing the substrates at high T (> 600 °C) for long time produces the same clusters. This may be due to the decomposition of the oxide layer in presence of Au which has long been demonstrated for other metals as well. To confirm that, in-situ LEEM and LEED experiments were used in collaboration with Pr. Frédéric Leroy from CINaM - Marseille. In this study we have observed that the Au droplets increase in size while diffusing on the surface after annealing at 700 °C, forming behind them bright regions whose LEED pattern is characteristic of the  $\sqrt{3}\times\sqrt{3}$  phase of Si(111) surface. This means that the SiO<sub>2</sub> has been decomposed and Au droplets started to collect some Si atoms from the substrate. Therefore, the main conclusion of this section is that Si atoms are always present in our Au catalyst droplets.

The experimental results obtained for NWs growth using the catalyst droplets studied earlier

are shown in the last section of Chapter I. We have demonstrated that, even though ultra-long and defect-free NWs can be obtained on Si substrates, controlling the growth process in HVPE is far from being optimized compared to MBE. We have seen that the main problem does not come from the vapor phase but other issues are also involved. During the growth, the catalyst droplets diffuse on the surface and deposit the GaAs as a buffer layer until covering the whole surface of the substrate. Once the latter is entirely covered, very tapered structures (scales) start to grow on its top, along with very low density of NWs. So far, we have demonstrated that adding Ga atoms in the catalyst droplet prior to the growth is necessary for increasing the NWs/scales ratio. HRTEM images show that these NWs grow along the  $\langle 111 \rangle_B$  direction and exhibit a pure ZB structure along their entire lengths.

**Chapter II** presents a theoretical study of NWs growth in presence of Si atoms in the catalyst droplets. It consists of two sections. In the first one we have developed a model and presented the supporting experimental data showing that the presence of Si in the Au-Ga-As droplets has a drastic effect on chemical potentials and the nucleation probabilities of VLS GaAs NWs grown on silicon substrates. Most importantly, silicon suppresses nucleation from the gallium-rich droplets as long as a certain critical concentration is not reached, with the most difficult nucleation of GaAs NWs occurring in the gold-free self-assisted VLS growth. Adding Si to the gold-rich droplets only enhances the NW nucleation. We speculate that more silicon should enter the droplets in MOVPE and HVPE due to enhanced silicon etching by chemical precursors. This explains the known issue of gallium-catalyzed growth of GaAs NWs by these techniques. It has been demonstrated that HVPE growth of GaAs NWs always occurs from very gallium-rich droplets due to a high material input of gallium. An oxide layer on Si(111) is then required which blocks out the early silicon diffusion into the droplet and helps to start the NW growth. Overall, our model correlates with prior experimental findings and may be further used to understand and control the VLS growth of other III-V NWs on silicon, silicon doping of III-V NWs, and even hybrid III-V-Si NWs.

In the second section, a thermodynamic study of the Si incorporation in GaAs NWs is reported. We have presented a model correlated to experimental data which allows for better understanding of Si doping of Au-catalyzed and Ga-catalyzed GaAs NWs. It has been shown that Si atoms are preferentially incorporated into As, rather than Ga sites of GaAs NWs due to a much lower As/Ga ratio (prevailing) in the mother phase during the VLS growth compared to VS growth. This explains why most VLS GaAs:Si NWs are p-type, while the standard VS growth leads to n-type doping. However, n-type doping of GaAs NWs with Si is expected at higher As concentrations in the droplet, which occurs for HVPE growth on Si substrates. These results can be used for obtaining n-type or p-type Si doping in GaAs NWs by tuning the growth conditions, or even Si-doped p-n junctions within a single NW.

The last chapter of this manuscript is **Chapter III**, in which we have investigated the charge and spin transport properties, as well as the luminescence and its degree of circular polarization of NWs grown by HVPE. Many types of NWs having different properties were studied. The first main difference between them is the substrate on which they were grown. This is shown to determine the doping level of the grown NWs which strongly affects their properties. We have shown that NWs

grown on GaAs substrate exhibit a p-doping behavior, whereas growing NWs on Si substrate results in n-doping. After estimating the doping levels, which were in the low  $10^{17} \text{ cm}^{-3}$  in both cases, we have demonstrated that the transport and the polarization are remarkably better in the n-doped NWs. Note that at such high n-doping level, NWs grown on Si substrates must be considered as disordered systems where the screened potential by the donors creates fluctuations in the bands.

Another key parameter that has a remarkable influence on the properties of NWs is the surface passivation. Two complementary techniques, namely hydrazine wet chemical passivation and plasma passivation, were used in this work. While plasma passivation appears to be of better quality, as judged from the PL intensity and the width of the PL lines in the spectra, it induces extra mechanisms of spin relaxation which reduces the spin diffusion length.

All passivated NWs grown on Si substrates exhibit similar charge and spin spatial profiles. In addition, these profiles are not observed on NWs grown on GaAs substrates. They are also weakly dependent on NW diameter, on temperature and on laser excitation power. This remarkable feature strongly suggests that transport mostly concerns hot electrons, i.e. electrons at an energy larger than the potential fluctuations of donor concentration. We are therefore led to conclude that, in NWs grown on Si substrates, hot electron charge and spin transport occurs over record lengths as large as  $6 \mu\text{m}$ . Moreover, the absence of intrinsic holes in these n-doped NWs results in a very large spin relaxation time, leading to photoelectron spin polarizations as large as 20 %, and to spin diffusion lengths almost as large as the charge diffusion lengths.

The qualitative interpretations given in this chapter open the way to several types of perspectives. First of all, it is highly interesting to further decrease the NW diameter, in order to investigate quantum wires, where diffusive transport may be replaced by ballistic transport. In addition, metallic disordered NWs constitute an attractive system for which transport should be investigated theoretically (using a self-consistent modeling and the landscape theory), and experimentally, by reducing the laser excitation energy in order to generate all electron-hole pairs in the fluctuations.

Advanced chemical characterizations of the passivated NWs surfaces are currently being performed. This will be a key parameter to understand the difference between the two passivation methods used in this work. It is also planned to investigate charge and spin transport in other GaAs NWs with different doping levels, as well as in other III-V NWs such as InAs and InGaAs.

Cl-VPE and HVPE were the very first epitaxial techniques developed for the growth of III-V semiconductor materials in the 60s. Being less efficient than MBE and MOVPE for the synthesis of low dimensionality III-V heterostructures, HVPE was almost abandoned for three decades, except by some research groups in the world, including the group of Institut Pascal. It turned out that when it came to nanowire growth, HVPE performed differently, generating nanowires with exceptional aspect ratio and crystal phase. To put it in a nutshell, all specificities of the NWs grown by HVPE are related to the use of high concentration of gallium in the catalyst droplets.

We do not know right now if the unusual NWs grown by HVPE will find any reliable application. However, we know that the HVPE experimental conditions - high growth temperature and high

material inputs, allow to elucidate the growth issues of the other techniques, MBE and MOVPE. It was one of the specifics of this thesis, which have highlighted the peculiar role of Si for the nucleation of GaAs NWs and proposed an answer to solve the enigma of the p- or n-type doping of GaAs with Si. From the point of view of the HVPE-grown nanowires themselves, their great length and their crystalline purity allow original physics studies, such as presented in Chapter III. Let us bet that they will give rise to unexpected applications.





## A.1 Calculation of the $f$ function

This section is devoted to the calculation of the  $f$  function given in Eq. II.3 of Chapter II, which is the difference between the chemical potentials of Ga-As pair in solid and liquid phases, with and without the presence of some Si atoms in the catalyst droplet. We assume here that the solid state is a pure GaAs without Si. Therefore, using Eq. II.1, the  $f$  function can be expressed as follows:

$$\begin{aligned}
 f &= \Delta\mu_{Si} - \Delta\mu_0 \\
 &= \Delta\mu_{GaAs}^0 + k_B T \ln(c_{Ga}) + k_B T \ln(c_{As}) + 2k_B T \ln(1 + c_{Si}) + \omega_{GaAs}(c_{Ga}^2 + c_{As}^2)(1 - c_{Si})^2 \\
 &+ (\omega_{GaSi} + \omega_{AsSi})c_{Si}^2 + (\omega_{GaAu} + \omega_{AsAu})[1 - (c_{Ga} + c_{As})(1 - c_{Si}) - c_{Si}]^2 \\
 &+ (\omega_{GaAs} + \omega_{GaAu} - \omega_{AsAu})c_{As}(1 - c_{Si})[1 - (c_{Ga} + c_{As})(1 - c_{Si}) - c_{Si}] \\
 &+ (\omega_{GaAs} + \omega_{AsAu} - \omega_{GaAu})c_{Ga}(1 - c_{Si})[1 - (c_{Ga} + c_{As})(1 - c_{Si}) - c_{Si}] \\
 &+ (\omega_{GaSi} + \omega_{GaAu} - \omega_{AuSi})c_{Si}[1 - (c_{Ga} + c_{As})(1 - c_{Si}) - c_{Si}] + (\omega_{AsSi} + \omega_{AsAu} - \omega_{AuSi})c_{Si} \quad (A.1) \\
 &\cdot [1 - (c_{Ga} + c_{As})(1 - c_{Si}) - c_{Si}] + (\omega_{GaSi} + \omega_{GaAs} - \omega_{AsSi})c_{Si}(1 - c_{Si})c_{As} \\
 &+ (\omega_{AsSi} + \omega_{GaAs} - \omega_{GaSi})c_{Si}(1 - c_{Si})c_{Ga} - \Delta\mu_{GaAs}^0 - k_B T \ln(c_{Ga}) - k_B T \ln(c_{As}) \\
 &- \omega_{GaAs}(c_{Ga}^2 + c_{As}^2) - (\omega_{GaAu} + \omega_{AsAu})(1 - c_{Ga} - c_{As})^2 \\
 &- (\omega_{GaAs} + \omega_{GaAu} - \omega_{AsAu})c_{As}(1 - c_{Ga} - c_{As}) \\
 &- (\omega_{GaAs} + \omega_{AsAu} - \omega_{GaAu})c_{Ga}(1 - c_{Ga} - c_{As})
 \end{aligned}$$

This equation can be simplified easily to:

$$\begin{aligned}
 f &= 2k_B T \ln(1 + c_{Si}) + \omega_{GaAs}(c_{Ga}^2 + c_{As}^2)c_{Si}^2 + (\omega_{GaSi} + \omega_{AsSi})c_{Si}^2 - \omega_{GaAs}(c_{Ga}^2 + c_{As}^2)2c_{Si} \\
 &+ (\omega_{GaAu} + \omega_{AsAu})(1 - c_{Ga} - c_{As})^2(c_{Si}^2 - 2c_{Si}) + (\omega_{GaAs} + \omega_{GaAu} - \omega_{AsAu}) \\
 &\cdot (1 - c_{Ga} - c_{As})c_{As}(c_{Si}^2 - 2c_{Si}) + (\omega_{GaAs} + \omega_{AsAu} - \omega_{GaAu})(1 - c_{Ga} - c_{As})c_{Ga}(c_{Si}^2 - 2c_{Si}) \quad (A.2) \\
 &+ (\omega_{GaSi} + \omega_{GaAu} - 2\omega_{AuSi} + \omega_{AsSi} + \omega_{AsAu})(1 - c_{Ga} - c_{As})(c_{Si} - c_{Si}^2) \\
 &[(\omega_{GaSi} + \omega_{GaAs} - \omega_{AsSi})c_{As} + (\omega_{AsSi} + \omega_{GaAs} - \omega_{GaSi})c_{Ga}](c_{Si} - c_{Si}^2)
 \end{aligned}$$

A simple development of this equation yields the following expression of the  $f$  function:

$$f \cong 2k_B T \ln(1 - c_{Si}) + \eta c_{Si} + \kappa c_{Si}^2 \quad (A.3)$$

where  $\eta$  and  $\kappa$  are the coefficients given by Eq. II.6 in the Chapter II.

## A.2 Estimation of Ga and Si concentrations in the droplet during growth

- **Initial state:** the structure (NW or scale) has a constant diameter which represents the diameter of the droplet during growth (see Fig. A.1). The corresponding droplet volume  $V_i$  can be expressed as:

$$V_i = \frac{\pi R_i^3}{3} f(\beta_i) \quad (\text{A.4})$$

where the geometrical function  $f(\beta)$  for a droplet with a contact angle  $\beta$  with the solid phase is given by [34]:

$$f(\beta) = \frac{(1 - \cos\beta)(2 + \cos\beta)}{(1 + \cos\beta)\sin\beta} \quad (\text{A.5})$$

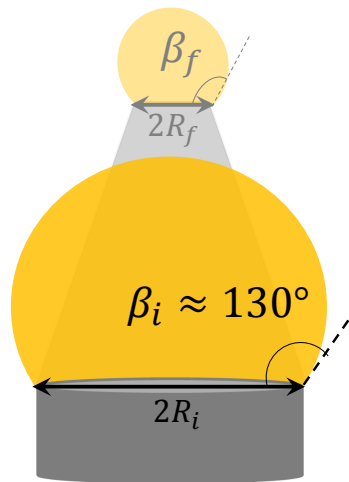


Figure A.1: A schematic representation of the method used to estimate the concentrations of gallium and silicon during growth, with  $\beta_i = 130^\circ$  and  $\beta_f = 95^\circ$  reported in ref [90].

The initial total number  $N_{tot}^i$  of atoms in the catalyst droplet during growth is the sum of different numbers of atoms ( $N_x^i$ ) for all species  $x$  present in this droplet. That is:

$$N_{tot}^i = N_{Au}^i + N_{Ga}^i + N_{As}^i + N_{Si}^i = \frac{V_i}{\Omega_{at}} \quad (\text{A.6})$$

where  $\Omega_{at}$  is the elementary averaged atomic volume estimated to be  $\sim 0.02 \text{ nm}^3$ .

- **Final state:** the diameter of the structure (NW or scale) after growth is measurable on HRTEM images (Table A.2). Similar to A.4, the final droplet volume  $V_f$  is given by:

$$V_f = \frac{\pi R_f^3}{3} f(\beta_f) \quad (\text{A.7})$$

where the final total number of atoms in the droplet after growth  $N_{tot}^f$  is:

$$N_{tot}^f = N_{Au}^f + N_{Ga}^f + N_{As}^f + N_{Si}^f = \frac{V_f}{\Omega_{at}} \quad (\text{A.8})$$

From EDS measurements, we have the concentration of each element  $c_x^f$  after growth. Therefore, we can deduce the number of atoms of specie  $x$  using:

$$N_x^f = c_x^f N_{tot}^f \quad (\text{A.9})$$

If we consider constant numbers of Si and Au atoms during and after growth ( $N_{Au}^i = N_{Au}^f$  and  $N_{Si}^i = N_{Si}^f$ ), and neglect the  $N_{As}$ , we can calculate:

$$c_{Si}^i = N_{Si}^f N_{tot}^i \quad (\text{A.10})$$

and then:

$$N_{Ga}^i = \frac{V_i - V_f}{\Omega_{at}} + N_{Ga}^f \quad (\text{A.11})$$

This allows us to calculate the concentration of Ga in the liquid phase during growth ( $c_{Ga}^i$ ) with the presence of Si in the droplet. In order to get the value without Si (the  $c_{Ga}$  in the text), we should divide  $c_{Ga}^i$  by  $(1 - c_{Si}^i)$ , that is:

$$c_{Ga} = \frac{c_{Ga}^i}{1 - c_{Si}^i} \quad (\text{A.12})$$

From HRTEM images and EDS measurements corresponding to S1, S2 and S3 given in Table A.2, we are able to calculate the  $c_{Ga}^i$  and  $c_{Si}^i$  provided in Table II.2 of Chapter II.

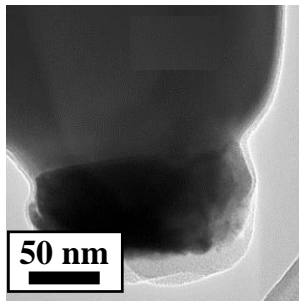
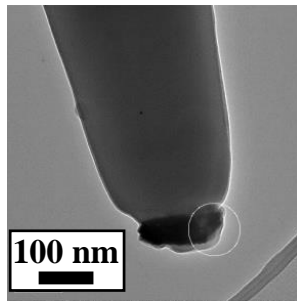
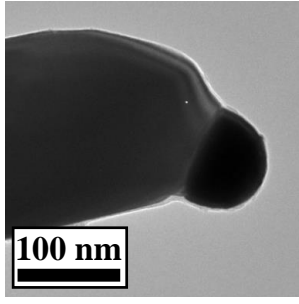
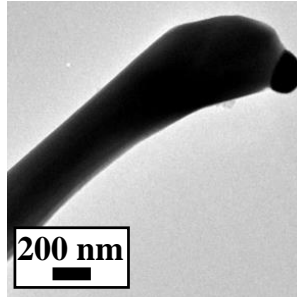
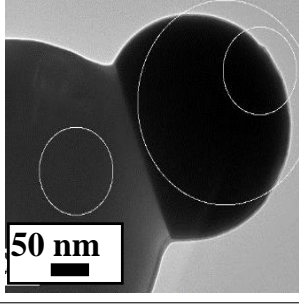
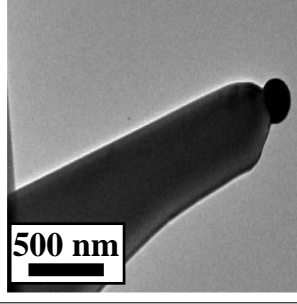
	SEM images		Element $x$	Final concentration $c_x^f$
S1			Au	10.8
			Si	20.5
			Ga	56.9
			As	11.8
S2			Au	73.6
			Si	3.5
			Ga	21.9
			As	1
S3			Au	78
			Si	2
			Ga	19
			As	1

Table A.1: HRTEM images of the gold-catalyzed GaAs structures with droplets on top, grown at 715 °C on different substrates: S1, S2, and S3.

### A.3 DFT input data and relaxed geometry

A cubic cell is defined, with Ga-atoms at the faces. It is initially a perfect zinc-blende crystal, with lattice parameter  $a = 5.65 \text{ \AA}$ . (10.68 Bohr).

Calculations are carried out with the PBE (a Generalised Gradient Approximation, GGA) functional that has previously given reliable properties and optimised geometries in the solid state, including for GaAs with and without exposed surfaces. Soft Troullier-Martins pseudo-potentials (PP) were generated using the Fritz-Haber Institute code, within the PBE framework. It was found that in the case of Ga, the core replaced by the pseudo-potential gave reliable band-structure only when limited to the Argon electron configuration, i.e.  $\text{Ar } 3d^{10} 4s^2 4p^1$  : this implies that the  $3d^{10}$  full sub-shell has to be taken into account explicitly, because the d-orbitals take part in the wave-function, governing interactions [198]. Band structure in agreement with experiment and other ab initio work can then also be generated [199, 200]. It also implies that faster calculations with the  $3d^{10}$  electrons replaced by a pseudo-potential are not accurate enough for this work. On the other hand, for the more electronegative group V elements, As and a fortiori N, the  $3d^{10}$  subshell was included in the As-PP and the valence limited to  $4s^2 4p^3$ . Similarly, for N, where the d-electron problem does not arise, the valence is  $2s^2 2p^3$  and the PP just represents a He core.

These soft PPs require a high kinetic energy cutoff, which we evaluated at 80 Ha. The k-point grid was the smallest that gave better than micro-Hartree accuracy, namely a cubic k-point grid generated by the Monkhorst Pack algorithm, with 12 points on each of the 3 k-axes.

This enabled us to generate a tight plane-wave basis and the PPs used were also generated numerically on the grid. Further input information is that we used the default smearing parameter for band-energy, i.e. 0.04 atomic units. This effectively improves convergence and is not interpreted as corresponding to a physical temperature. It is possible to use a smaller value that is proportional to the experimental temperature of 715 °C, however this is only of interest if attempting dynamics.

The minimal calculation cell comprises 3 of these 8-atom cells along the z-axis and can easily be adapted to slab calculations involving a surface. Periodic boundary conditions are applied in all directions.

The energy reference is obtained from the total internal energy difference with respect to pure GaAs, by comparing with the exchange of isolated neutral atoms. We add the energy of the replaced atom in a large cubic box, itself repeated periodically using the same k-point grid, PP and energy cutoff. Then, the energy of isolated Si determined in the same way is subtracted.

The software used was ABINIT. Version 8.10.

Runs were on 120 cores of the CRRI (Centre Régional de Ressources Informatique) in Aubière, France, for which we thank the President Antoine Mahul for generous time allocations. The code is in Fortran/C, C++, python scripts and requires OpenMPI for parallel runs. The CRRI runs a Slurm OS.

<b>Cartesian coordinates one Si in a tetrahedral interstice (relaxed) [bohr]</b>			
<b>Ga</b>	-6.10729104077150E-03	-1.16232926412785E-01	1.23218504982682E-01
<b>Ga</b>	5.34610729104077E+00	5.45623292641278E+00	1.23218504982682E-01
<b>Ga</b>	-6.10729104077150E-03	5.45623292641278E+00	5.21678149501732E+00
<b>Ga</b>	5.34610729104077E+00	-1.16232926412785E-01	5.21678149501732E+00
<b>Si</b>	2.67000000000000E+00	2.67000000000000E+00	2.67000000000000E+00
<b>As</b>	2.67000000000000E+00	2.67000000000000E+00	8.01000000000000E+00
<b>As</b>	8.01000000000000E+00	8.01000000000000E+00	2.67000000000000E+00
<b>As</b>	8.01000000000000E+00	2.67000000000000E+00	8.01000000000000E+00

Table A.2: Optimised co-ordinates for evaluation of Ga-Si internal energy. Based on GaAs zinc-blende, bulk.

<b>Cartesian coordinates one Si in fcc Ga position, relaxed [bohr]</b>			
<b>Si</b>	7.79391915344754E-03	-1.68083706620244E-02	-7.79391915344754E-03
<b>Ga</b>	5.34100992237488E+00	5.36568177558421E+00	-3.21352316671894E-04
<b>Ga</b>	3.21352316671894E-04	5.36568177558421E+00	5.33899007762512E+00
<b>Ga</b>	.34060638287147E+00	-2.76516160129674E-02	5.33939361712853E+00
<b>As</b>	2.66056037490393E+00	2.66497151042704E+00	2.66442436831957E+00
<b>As</b>	2.66576050139413E+00	2.66828238340000E+00	8.01423949860587E+00
<b>As</b>	8.00837191530504E+00	8.01487103125248E+00	2.67162808469496E+00
<b>As</b>	8.01557563168043E+00	2.66497151042704E+00	8.01943962509607E+00

Table A.3: Optimised co-ordinates for evaluation of As-Si internal energy. Based on GaAs zinc-blende, bulk.

These appendices are devoted to mathematical aspects specific to nanowires.

## B.1 Resolution of the diffusion equation in a NW

In this section, the resolution of the time-independent diffusion equation (Eq. III.10) with the boundary condition III.11 is explained.

This solution is developed on a basis of separable functions of radial ( $r$ ) and axial ( $z$ ) components (see Fig. III.5 of Chapter III), namely:

$$n(r, z) = \sum_{m=0}^{\infty} u_m(r) f_m(z) \quad (\text{B.1})$$

The eigenfunctions  $u_m(r)$  of the radial Laplacian operator  $\frac{1}{r} \frac{\partial}{\partial r} r \frac{\partial}{\partial r}$  are given by:

$$\frac{\partial^2 u_m(r)}{\partial r^2} + \frac{1}{r} \frac{\partial u_m(r)}{\partial r} + k_m^2 u_m(r) = 0 \quad (\text{B.2})$$

where  $k_m^2$  are the eigenvalues of order  $m$  ( $k_m$  has the dimension of an inverse length). If we change the variable  $r$  to  $\frac{t}{k_m}$ , a dimensionless equation in  $t$  can be obtained in the form:

$$\frac{\partial^2 u_m}{\partial t^2} + \frac{1}{t} \frac{\partial u_m}{\partial t} + u_m = 0 \quad (\text{B.3})$$

This is a Bessel equation which has a normalized solution given by:

$$u_m(r) = \frac{J_0(k_m \cdot r)}{[\int_0^{r_0} J_0^2(k_m r) \cdot 2\pi r dr]^{1/2}} = B_m J_0(k_m r) \quad (\text{B.4})$$

As a result, using the known expression of the integral at the denominator, the coefficients  $B_m$  can be expressed as:

$$B_m = \frac{1}{\sqrt{\pi r_0^2 [J_0^2(k_m r) + J_1^2(k_m r)]}} \quad (\text{B.5})$$

Here,  $J_0$  and  $J_1$  are the Bessel functions of order 0 and 1, respectively, and we recall that  $r_0$  is the NW radius. These functions must satisfy:

$$\int_0^{r_0} u_m u_{m'} 2\pi r dr = \delta_{mm'} \quad (\text{B.6})$$

where  $\delta_{mm'}$  is the Kronecker symbol.

The values of  $k_m$  can be obtained graphically using the following boundary condition (see Eq. III.11):

$$\left. \frac{k_m r_0}{J_0(k_m \cdot r_0)} \frac{\partial J_0(t)}{\partial t} \right|_{k_m r_0} = -\frac{S r_0}{D_e} \quad (\text{B.7})$$

where  $S r_0 / D_e$  is a dimensionless measure of surface recombination.

Shown in the top panel of Fig. B.1 is the dependence on  $t$  of  $J_0(t)$ , and of  $\partial J_0(t) / \partial t$ . The bottom panel shows the left term of Eq. B.7. Graphical solution of Eq. B.7 is obtained by intersecting the latter curve by a horizontal straight line of ordinate  $S r_0 / D_e$ . It is seen that for a given value of  $S r_0 / D_e$ , Eq. B.7 has an infinite number of solutions:  $k_m r_0$ .

Fig. B.2 shows the obtained values of  $k_0 r_0$  for several values of  $S r_0 / D_e$ . It is seen that, in the weak recombination regime, defined by  $S r_0 / D_e < 1$ , we have:

$$k_0 r_0 \sim 1.2 \sqrt{\frac{S}{D_e r_0}} \quad (\text{B.8})$$

As seen in Fig. B.1, the higher order modes have  $k_m r_0$  that nearly corresponds to the distance at which  $\partial J_0(t) / \partial t \sim 0$  weakly depend on  $S / D_e r_0$  in this regime. Thus we have within 10 %:  $k_1 r_0 \sim 3.7$ ,  $k_2 r_0 \sim 6.9$  and  $k_3 r_0 \sim 10.1$ .

Let us now find the solution of the axial Laplacian. This can be done by replacing Eq. B.1 in the Helmholtz equation, multiplying by  $u_m(r)$ , integrating over  $r$  and using Eq. B.6. The obtained expression is then:

$$L_c^2 \frac{\partial^2 f_m(z)}{\partial z^2} - (1 + k_m^2 L_c^2) f_m(z) + \tau_c \int_0^{r_0} g(r, z) u_m(r) 2\pi r dr = 0. \quad (\text{B.9})$$

A solution of this equation is given by the following expression:

$$f_m(z) = \int_0^\infty e^{-\frac{z_0}{L_m}} \left[ \int_0^{r_0} g(r, z - z_0) u_m(r) 2\pi r dr \right] dz \quad (\text{B.10})$$

where  $L_m$  are the diffusion lengths of modes of order  $m$ , given by:

$$L_m = \frac{L_c}{\sqrt{r_0^2 + (k_m r_0)^2 L_c^2}} \quad (\text{B.11})$$

with  $L_c$  is the diffusion length in the bulk, which is not well-known at LT. It is probably of the order of several microns at RT [201] and is believed to slightly decrease upon temperature decrease [145]. Here for specificity, we shall take  $L_c \sim 6 \mu\text{m}$ .

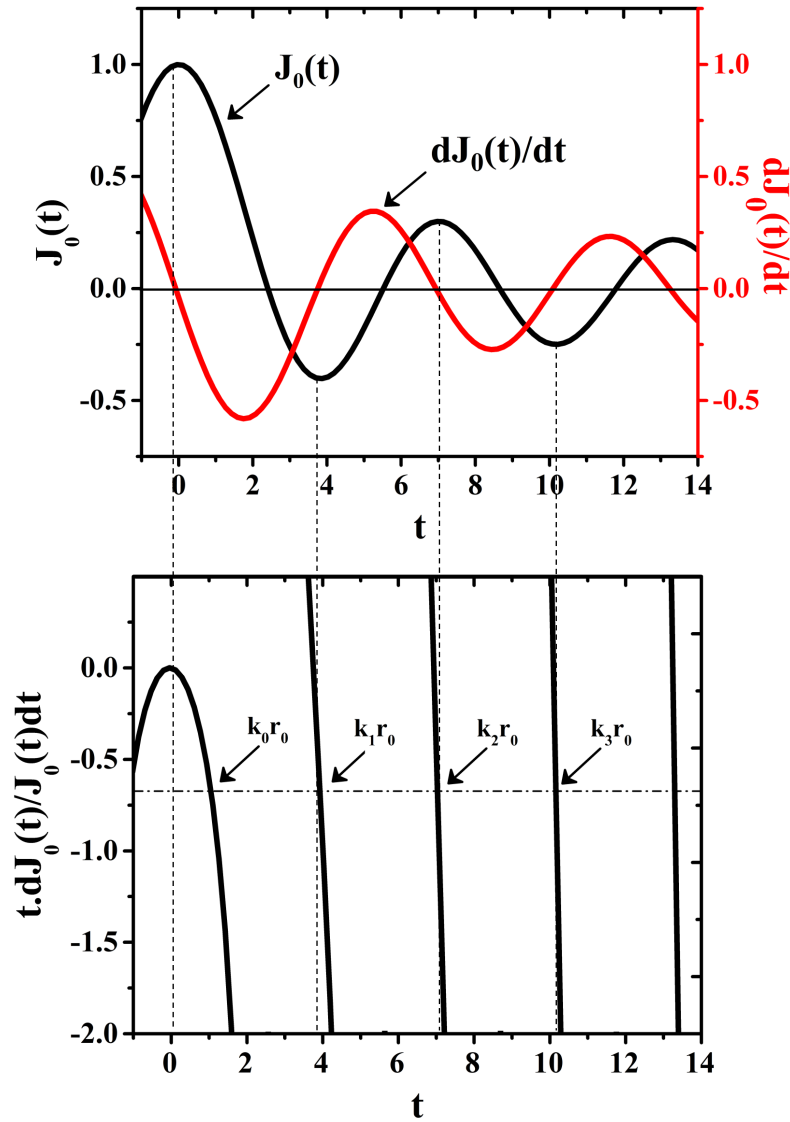


Figure B.1: Graphical resolution of Eq. B.7. (a) The Bessel function  $J_0(k_m r)$  in red and its derivative with respect to  $r$  in black. (b) The left term of Eq. B.7. Also shown is a horizontal straight line of ordinate  $-S/D_e r_0$ . Shown by arrows are the successive values of  $k_m r_0$ .

As mentioned before, the generation term can be considered as constant throughout the radial direction since the absorption depth is larger than the NW diameter and therefore can be excluded from the integration over  $r$ . That is:

$$\int_0^{r_0} g(r, z - z_0) u_m(r) 2\pi r dr = g(z - z_0) \int_0^{r_0} u_m(r) 2\pi r dr \quad (\text{B.12})$$

where  $g(z) = \exp\left(-\frac{z^2}{\omega^2}\right)$ . This gives an expression of  $f_m(z)$  as:

$$f_m(z) = \int_0^{r_0} u_m(r) 2\pi r dr \int_0^\infty g(z - z_0) e^{-\frac{z_0}{L_m}} dz \quad (\text{B.13})$$

where the radial integral is given by:

$$\int_0^{r_0} u_m(r) 2\pi r dr = B_m \int_0^{r_0} J_0(k_m r) 2\pi r dr \quad (\text{B.14})$$

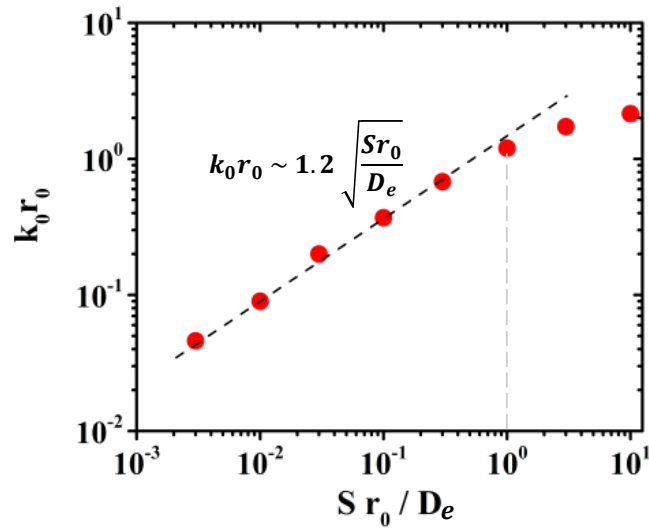


Figure B.2: The left panel is table that summarizes the values of  $t = k_m r_0$  obtained graphically for all modes. The right panel shows the change of regime at  $S r_0 / D_e = 1$  for the lowest order mode.

Using the known value of the integral at the right hand of this equation, we obtain:

$$\int_0^{r_0} u_m(r) 2\pi r dr = B_m \frac{2\pi r_0}{k_m} J_1^2(k_m r_0) \quad (\text{B.15})$$

The carrier concentration can then be calculated using B.1, which gives:

$$\begin{aligned} n(r, z) &= \sum_{m=0}^{\infty} u_m(r) f_m(z) \\ &= \sum_{m=0}^{\infty} \left[ B_m \frac{2\pi r_0}{k_m} J_1^2(k_m r_0) \right] u_m(r) \int_0^{\infty} g(z - z_0) e^{-\frac{z_0}{L_m}} dz \end{aligned} \quad (\text{B.16})$$

Similarly, an analogous equation can be written for spin with  $L_s = \sqrt{D_e \cdot \tau_s}$  as diffusion length instead of  $L_c$ . Here,  $\tau_s$  is the spin life time.

The final radial solution consists of a combination of modes at given  $z$ , which gives the following expression at  $z = 0$ :

$$\begin{aligned} n(r, 0) &= \sum_{m=0}^{\infty} \left[ \int_0^{r_0} u_m(r) 2\pi r dr \right] u_m(r) \\ &\propto u_0(r) + \sum_{n=m+1}^{\infty} C_n u_n(r) \end{aligned} \quad (\text{B.17})$$

with  $C_n$  are the normalized coefficients with respect to the order zero. The resulting radial profiles are given in Fig. B.3-(R-1), (R-2) and (R-3) for different diameters and surface recombination velocities. Note that, for the chosen NW radius  $r_0$  and reduced surface recombination, the concentration  $n$  does not exhibit any oscillating character but, as expected physically, mostly decreases from the center to the edge of the NW. It is concluded from Fig. B.3-(R-2) and B.3-(R-3) that the amplitude of radial profiles of  $n$  (shown in red) at the center are slightly affected by the surface recombination. However,

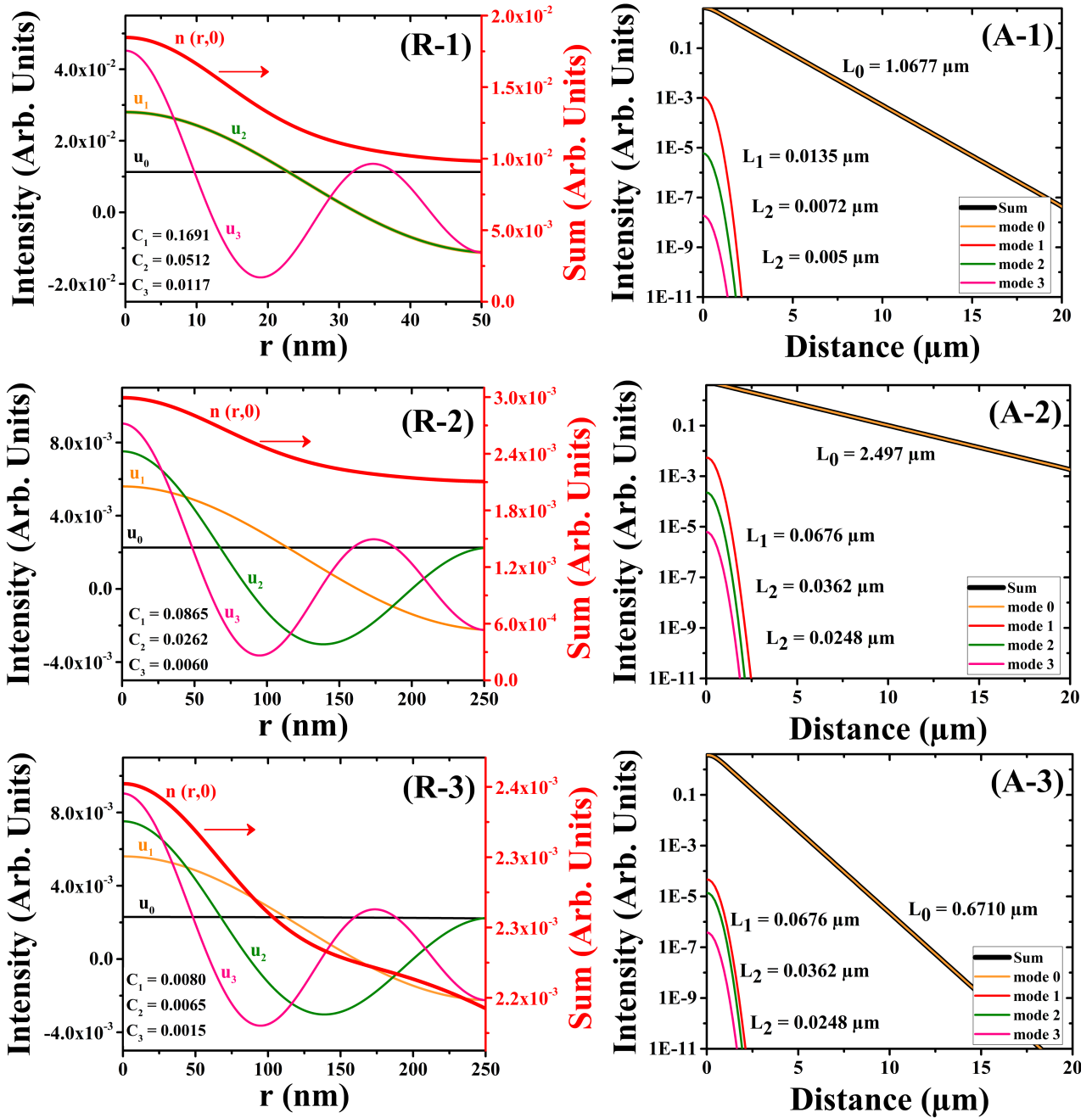


Figure B.3: Radial profiles of  $u_m$  and of the density of photoelectrons (left panels: at  $z = 0$  according to Eq. B.17) and axial profiles of the luminescence intensity (right panels: according to Eq. B.18) of the various spatial modes. Numbers 1, 2 and 3 represents NWs with the respective following characteristics: (1)  $r_0 = 50$  nm and  $Sr_0/D_e = 0.003$ , (2)  $r_0 = 250$  nm and  $Sr_0/D_e = 0.01$ , and (3)  $r_0 = 250$  nm and  $Sr_0/D_e = 0.1$ . The transition from (1) to (2) corresponds to an increase in  $r_0$  with  $S$  nearly constant. The transition from (2) to (3) implies an increase of  $S$  with  $r_0$  constant. The radial profiles of the various modes ( $u_0, u_1, u_2, \dots$ ) are combined to form the profile of the photoelectron density  $n$ . The axial profiles reveal that in all cases, the fundamental, zero-order, mode is dominant over the higher order modes.

for a fixed surface recombination (Fig. B.3-(R-1) and B.3-(R-2)), increasing the radius of the NW results in a decrease of amplitudes of the profiles.

We finally consider the PL axial profiles as a function of  $z$ , that give the diffusion lengths. These profiles give the spatial profiles measured in the present work. The PL intensity can be obtained by integration of  $n(r, z)$  over the section of the NW at constant  $z$ . Using B.15 we have:

$$I_{PL}(z) = \sum_{m=0}^{\infty} A_m \int_0^{\infty} e^{-\frac{z}{L_m}} \times g(z - z_0) dz \quad (\text{B.18})$$

with

$$A_m = \frac{4\pi}{k_m^2} \frac{J_1^4(k_m r_0)}{J_0^2(k_m r_0) + J_1^2(k_m r_0)} \quad (\text{B.19})$$

So the PL axial profiles are the sum of several spatial modes.

As seen in Fig. B.3-(A-1), (A-2) and (A-3), the order 0 mode is the predominant one in all NWs, while higher order modes contributions are smaller. So we can safely consider only this latter to describe our system and neglect all the others. Panel (A-1) shows the case of thin NW of  $r_0 = 50$  nm, while (A-2) and (A-3) represent a larger NW which has a radius  $r_0 = 250$  nm. The surface recombination  $S$  is almost the same for (A-1) and (A-2), which is about  $\sim 0.4-0.6 \cdot 10^{-4} D$ , however the diameter of the NW represented in (A-2) is 5 times larger than that in (A-1). As expected, we can conclude from these figures that increasing the NW radius increases the diffusion length. This is due to the reduced surface-to-volume ratio. Thus in this case the non-radiative surface recombination is less effective. On the other hand, a comparison between (A-2) and (A-3) allows us to emphasize the impact of  $S$  for a fixed NW radius. It is clearly seen that, when  $S$  is increased to  $4 \cdot 10^{-4} D_e$  corresponding to  $Sr_0/D_e \sim 0.1$ , the diffusion length is decreased dramatically by a factor  $\sim 4$ , to a value much lower than the experimental results.

As seen from these results, the only possibility to have  $L_0$  larger than  $1 \mu\text{m}$  with a starting value  $L_c \sim \text{several } \mu\text{m}$  is to have  $Sr_0/D_e \ll 1$ . In this case, only the fundamental spatial mode is dominant in Eq. B.18. It exhibits an exponential decay convoluted with the generation function  $g$  defined by Eq. B.12, for which the characteristic length depends on  $Sr_0/D_e$  according to Eq. III.14.

## B.2 Poisson's equation in NWs

The subsurface depletion region is induced by the transfer of holes (in n-type NW) from bulk to surface due to the presence of localized surface states. Assuming a homogeneous doping concentration  $N_D$  and an axial symmetry in the NW, we can consider a surface charge region (SCR) of constant width ( $w_{SCR}$ ) surrounding an non-depleted core. Due to the specific geometry of NWs, the Poisson equation must be solved in cylindrical coordinates. The electric field present in the SCR region can lead to a separation of carriers that can significantly reduce the recombination efficiency [170]. Since the NW can be considered quasi infinite along the  $z$ -axis, components of the electric field not parallel to the NW radius can be neglected. In order to calculate the surface potential and estimate  $w_{SCR}$ , the radial Poisson's equation in the SCR must be written for a NW of radius  $r_0$  as:

$$\frac{1}{r} \frac{\partial}{\partial r} r \frac{\partial}{\partial r} \varphi(r) = -\frac{qN_D}{\epsilon_r \epsilon_0} \quad (\text{B.20})$$

Here,  $\varphi(r)$  is the surface potential in the SCR, where  $r$  is the distance from the NW center.  $\epsilon_0$  denotes the vacuum permittivity,  $\epsilon_r$  is the dielectric constant. Fig. B.4 is a schematic representation of the NW in the radial direction.

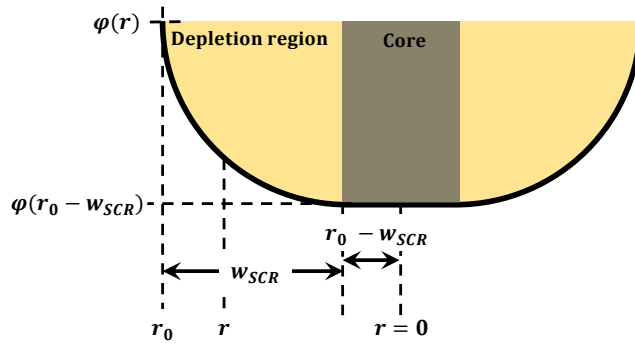


Figure B.4: Schematic representation of the Fermi level pinning near the surface of the NW.  $\varphi(r)$  is the electric potential induced by the transfer of carriers toward the surface due to the presence of localized surface states.  $\varphi(r_0 - w_{SCR})$  is the electric potential at the onset of the depletion region. The center of the NW is considered as the origin of the  $r$  axis,  $r_0$  is the radius of the NW and  $r$  is the distance from the center.

The potential  $\varphi(r) - \varphi(r_0 - w_{SCR})$  at a given distance from the center is obtained by a double integration of Eq. B.20 between  $r_0 - w_{SCR}$  and  $r$  [170]. This gives:

$$\varphi(r) - \varphi(r_0 - w_{SCR}) = -\frac{qN_D}{\epsilon\epsilon_0} \frac{r^2}{4} + \frac{qN_D}{\epsilon\epsilon_0} \frac{(r_0 - w_{SCR})^2}{4} + \frac{qN_D}{\epsilon\epsilon_0} \frac{(r_0 - w_{SCR})^2}{2} \ln\left(\frac{r_0}{r_0 - w_{SCR}}\right) \quad (\text{B.21})$$

We obtain for  $r = r_0$ :

$$w_{2D}^2 = -(r_0 - w_{SCR})^2 \ln\left(\frac{r_0}{r_0 - w_{SCR}}\right) + r_0 w_{SCR} - \frac{w_{SCR}^2}{2} \quad (\text{B.22})$$

where  $w_{2D}$  is given by

$$w_{2D} = \sqrt{\frac{2\epsilon\epsilon_0\phi_b}{qN_D}} \quad (\text{B.23})$$

is the width of the SCR for a planar system of identical doping and  $\phi_b$  is the barrier height.

In the case of a NW with a large radius, such that  $w_{SCR} \ll r_0$ , we have:

$$w_{SCR} = w_{2D} \quad (\text{B.24})$$

For the limit of full depletion of the NW  $w_{SCR} \approx r_0$ , we have:

$$w_{SCR} = \sqrt{2}w_{2D} \quad (\text{B.25})$$

### B.3 Surface photovoltage

In the dark, the potential barrier  $\varphi_0$  at the semiconductor surface is defined by the energy difference between the bottom of the CB at the surface and the Fermi energy level in the bulk. Under light excitation as shown in Fig. B.5, because of minority carrier injection, there occurs a shift  $\Delta\varphi$  of the quasi Fermi level  $E_{F_n}$  with respect to midgap, and a difference between  $E_{F_n}$  and  $E_F$  called the photovoltage  $qV_s$ . The potential barrier  $\varphi_0$  becomes [167]:

$$\varphi_b = \varphi_0 + \Delta\varphi - qV_s \quad (\text{B.26})$$

Due to the presence of photovoltage, the surface is now under effective bias in a radial direction. This induces a current, called the Schottky current, of the majority carriers, for which the expression is:

$$J_s = A^{**}T^2 \exp\left(-\frac{\varphi_0 + \Delta\varphi}{k_B T}\right) \left[ \exp\left(\frac{qV_s}{k_B T}\right) - 1 \right] \quad (\text{B.27})$$

with  $A^{**}$  is the effective Richardson constant and  $T$  is the temperature.

Under light excitation, photocreated holes migrate towards the surface and are injected into the BB region defined in Appendix B.2. This photo-injected current is denoted  $J_p$  and can be written as  $qp_0S$ , where  $p_0$  is the hole density at the edge of the SCR and  $S$  is the surface recombination velocity. At equilibrium, we have :

$$qp_0S = A^{**}T^2 \exp\left(-\frac{\varphi_0 + \Delta\varphi}{k_B T}\right) \left[ \exp\left(\frac{qV_s}{k_B T}\right) - 1 \right] \quad (\text{B.28})$$

Under focused light excitation, the hole concentration is axially (along  $z$ ) inhomogeneous. This induces at the place of excitation a local increase of the surface photovoltage, which creates an electric field  $E^{pv}$  in the axial direction ( $z$ ) of the NW and therefore a drift current parallel to the surface given by:

$$J_h^{pv} = q\mu_h p_0 E^{pv} = qp_0\mu_h \frac{\partial V_s(z)}{\partial z} = qp_0\mu_h \frac{\partial V_s(z)}{\partial p_0} \vec{\nabla}_z p_0 \quad (\text{B.29})$$

where  $\mu_h$  is the hole mobility and  $p_0$  is the photoholes concentration at the onset of the depletion region. This is typically a diffusion equation whose effective diffusion constant is  $D_h^* = p_0\mu_h \partial V_s(z) / \partial p_0$ .

Note that the reduction of the band bending can occur either on the surface or at the onset of the SCR. In the first case,  $J_h^{pv}$  will be screened by the current of photoholes present in the SCR of concentration  $p_s$ , whereas in the second case it will be screened by the holes of the bulk. Since the ratio  $p_s/p_0$  is very large, we can assume that the screening on the surface is much more efficient at the surface than in bulk. Consequently, the band bending is most likely to be reduced in the bulk [168].

The quantity  $\partial V_s(z) / \partial p_0$  of Eq. B.29 can be calculated if we consider the equilibrium between  $J_p$  and the Schottky current  $J_s$  for all values of  $r$  (Eq. B.28). In the case where  $qV_s \gg T$  and using  $S = S_0 \exp(-\frac{\Delta\varphi}{k_B T})$  [168], this gives:

$$\frac{\partial V_s}{\partial p_0} = \frac{1}{p_0} \frac{k_B T}{q} \quad (\text{B.30})$$

Using Eq. B.26 and Einstein's relation, the back-diffusion of holes induced by the photovoltage can be written as:

$$J_h^{pv} = qD_h \vec{\nabla}_z p_0 \quad (\text{B.31})$$

where  $D_h$  is the usual hole diffusion constant. Near  $z = 0$ , this current compensates exactly the current of holes diffusing out of the excitation zone, thus blocking this diffusion.

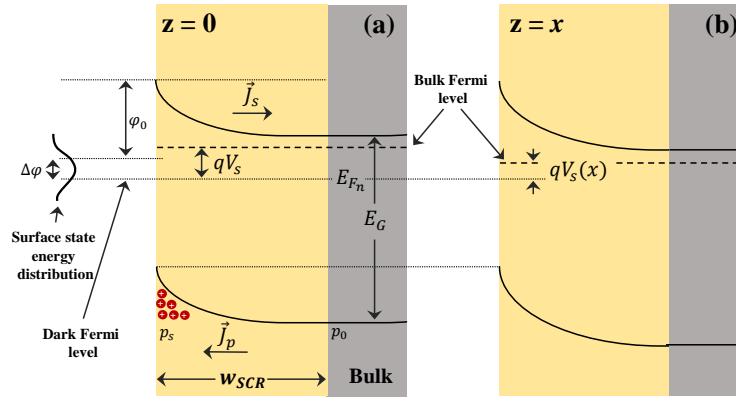


Figure B.5: Schematic representations of the band structure of the photo-excited GaAs NW. Panel (a) corresponds to the place of light excitation and shows the surface electron quasi Fermi level  $E_{Fn}$ , shifted from its position in the dark by  $\Delta\phi$ , and the photovoltage value  $qV_s$ . In comparison, panel (b), showing the band structure at distance  $x$  from the laser spot, shows a smaller photovoltage  $qV_s(x)$ . Because of the screening by the large subsurface photohole concentration  $p_s$ , the positions of the conduction and valence band at the surface do not depend on  $x$ , so that the photovoltage spatial dependence only concerns the band energy in the bulk region near the onset of the depletion region. The resulting electric field in the surface plane blocks the diffusion of photoholes in the plane parallel to the surface. Also shown are the photocurrent  $J_p$ , the Schottky current  $J_s$  and the width of the depletion zone  $w_{SCR}$ .

## Bibliography

- [1] P. Krogstrup, H. I. Jørgensen, M. Heiss, O. Demichel, J. V. Holm, M. Aagesen, J. Nygard, and A. Fontcuberta i Morral, “Single-nanowire solar cells beyond the Shockley–Queisser limit,” *Nature Photonics*, vol. 7, pp. 306–310, 2013.
- [2] H. A. Atwater and A. Polman, “Plasmonics for improved photovoltaic devices,” *Nature Materials*, vol. 9, p. 865, 2010.
- [3] N. Guan, X. Dai, A. Babichev, F. Julien, and M. Tchernycheva, “Flexible inorganic light emitting diodes based on semiconductor nanowires,” *Chemical Science*, vol. 8, pp. 7904–7911, 2017.
- [4] M. R. Ramdani, “Croissance sélective HVPE et VLS-HVPE d’objets et de structures GaAs à morphologie contrôlée à l’échelle sub-micrométrique et nanométrique,” 2012.
- [5] M. R. Ramdani, E. Gil, C. Leroux, Y. André, A. Trassoudaine, D. Castelluci, L. Bideux, G. Monier, C. Robert-Goumet, and R. Kupka, “Fast growth synthesis of GaAs nanowires with exceptional length,” *Nano Letters*, vol. 10, no. 5, pp. 1836–1841, 2010.
- [6] E. Gil, V. G. Dubrovskii, G. Avit, Y. André, C. Leroux, K. Lekhal, J. Grecenkov, A. Trassoudaine, D. Castelluci, G. Monier, R. M. Ramdani, C. Robert-Goumet, L. Bideux, J. C. Harmand, and F. Glas, “Record pure zincblende phase in GaAs nanowires down to 5 nm in radius,” *Nano Letters*, vol. 14, no. 7, pp. 3938–3944, 2014.
- [7] G. Avit, *Micro-et nanofils de Ga (In) N et GaAs par épitaxie en phase vapeur par la méthode aux hydrures (HVPE)*. Phd thesis, Université Blaise Pascal - Clermont II, 2015.
- [8] G. Monier, *Nanostructuration de surfaces de GaAs : oxydation et nitruration*. PhD thesis, Université Blaise Pascal - Clermont II, 2012.
- [9] H. Mehdi, *Etude de la passivation du GaAs ( 100 ) par nitruration par plasma N2 sous ultra-vide*. PhD thesis, Université Clermont Auvergne, 2018.
- [10] R. S. Wagner and W. C. Ellis, “Vaporliquid-solid mechanism of single crystal growth,” *Applied Physics Letters*, vol. 4, no. 5, pp. 89–90, 1964.
- [11] T. Bryllert, L. E. Wernersson, T. Löwgren, and L. Samuelson, “Vertical wrap-gated nanowire transistors,” *Nanotechnology*, vol. 17, no. 11, 2006.
- [12] C. P. Svensson, T. Mårtensson, J. Trägårdh, C. Larsson, M. Rask, D. Hessman, L. Samuelson, and J. Ohlsson, “Monolithic GaAs / InGaP nanowire light emitting diodes on silicon .,” *Nanotechnology*, vol. 19, no. 30, p. 305201, 2008.
- [13] E. Dimakis, M. Ramsteiner, A. Tahraoui, H. Riechert, and L. Geelhaar, “Shell-doping of GaAs nanowires with Si for n-Type conductivity,” *Nano Res.*, vol. 5, no. 11, pp. 796–804, 2012.

- [14] M. S. Gudiksen, L. J. Lauhon, J. Wang, D. C. Smith, and C. M. Lieber, "Growth of nanowire superlattice structures for nanoscale photonics and electronics," *Nature*, vol. 415, p. 617, 2002.
- [15] J. Wallentin, N. Anttu, D. Asoli, M. Huffman, I. Åberg, M. H. Magnusson, G. Siefert, P. Fusskailuweit, F. Dimroth, B. Witzigmann, H. Q. Xu, L. Samuelson, K. Deppert, and T. Magnus, "InP nanowire array solar cells achieving 13.8% efficiency by exceeding the ray optics limit," *Scienceexpress*, vol. 339(6123), pp. 1057–60, 2013.
- [16] P. Yang, R. Yan, and M. Fardy, "Semiconductor nanowire: Whats next?," *Nano Letters*, vol. 10, no. 5, pp. 1529–1536, 2010.
- [17] V. T. Duoc, D. T. Le, N. D. Hoa, N. Van Duy, C. M. Hung, H. Nguyen, and N. Van Hieu, "New design of ZnO nanorod- and nanowire-based NO<sub>2</sub> room-temperature sensors prepared by hydrothermal method," *Journal of Nanomaterials*, vol. 2019, pp. 1–9, 2019.
- [18] M. Mongillo, P. Spathis, G. Katsaros, P. Gentile, and S. De Franceschi, "Multifunctional devices and logic gates with undoped silicon nanowires," *Nano Letters*, pp. 3074–3079, 2012.
- [19] Y. Cui, Z. Zhong, D. Wang, W. U. Wang, and C. M. Lieber, "High performance silicon nanowire field effect transistors," *Nano Letters*, vol. 3, no. 2, pp. 149–152, 2003.
- [20] E. Roche, Y. André, G. Avit, C. Bougerol, D. Castelluci, F. Réveret, E. Gil, F. Médard, J. Leymarie, T. Jean, V. G. Dubrovskii, and A. Trassoudaine, "Circumventing the miscibility gap in InGaN nanowires emitting from blue to red," *Nanotechnology*, vol. 29, p. 465602, 2018.
- [21] V. G. Dubrovskii, G. E. Cirlin, I. P. Soshnikov, A. A. Tonkikh, N. V. Sibirev, and V. M. Ustinov, "Diffusion-induced growth of GaAs nanowiskers during molecular beam epitaxy: Theory and experiment," *Physical Review B*, vol. 71, no. 205325, pp. 5–7, 2005.
- [22] J. C. Harmand, G. Patriarche, N. Péré-Laperne, M.-N. Mérat-Combes, L. Travers, and F. Glas, "Analysis of vapor-liquid-solid mechanism in Au-assisted GaAs nanowire growth," *Applied Physics Letters*, vol. 87, p. 203101, 2005.
- [23] J. C. Harmand, M. Tchernycheva, G. Patriarche, L. Travers, F. Glas, and G. Cirlin, "GaAs nanowires formed by Au-assisted molecular beam epitaxy : Effect of growth temperature," *Journal of Crystal Growth*, vol. 301-302, pp. 853–856, 2007.
- [24] H. Hijazi, V. G. Dubrovskii, G. Monier, E. Gil, C. Leroux, G. Avit, A. Trassoudaine, C. Bougerol, D. Castellucci, C. Robert-Goumet, and Y. André, "Influence of silicon on the nucleation rate of GaAs nanowires on silicon substrates," *Journal of Physical Chemistry C*, vol. 122, no. 33, pp. 19230–19235, 2018.
- [25] H. Hijazi, G. Monier, E. Gil, A. Trassoudaine, C. Bougerol, C. Leroux, D. Castelluci, C. Robert-Goumet, P. Hoggan, Y. André, N. Isik Goktas, R. R. LaPierre, and V. G. Dubrovskii, "Si doping of vapor-liquid-solid GaAs nanowires: n-type or p-type?," *Nano Letters*, vol. 19, pp. 4498–4504, 2019.

- [26] C. Y. Yeh, Z. W. Lu, S. Froyen, and A. Zunger, “Zinc-blendewurtzite polytypism in semiconductors,” *Physical Review B*, vol. 46, no. 16, pp. 10086–10097, 1992.
- [27] M. I. McMahon and R. J. Nelmes, “Observation of a wurtzite form of gallium arsenide,” *Physical Review Letters*, vol. 95, no. 21, pp. 18–21, 2005.
- [28] F. Glas, J. C. Harmand, and G. Patriarche, “Why does wurtzite form in nanowires of III-V zinc blende semiconductors?,” *Physical Review Letters*, vol. 99, no. 14, pp. 3–6, 2007.
- [29] V. G. Dubrovskii, N. V. Sibirev, J. C. Harmand, and F. Glas, “Growth kinetics and crystal structure of semiconductor nanowires,” *Physical Review B - Condensed Matter and Materials Physics*, vol. 78, no. 23, 2008.
- [30] J. C. Harmand, G. Patriarche, F. Glas, F. Panciera, I. Florea, J. L. Maurice, L. Travers, and Y. Ollivier, “Atomic step flow on a nanofacet,” *Physical Review Letters*, vol. 121, no. 16, p. 166101, 2018.
- [31] C. Colombo, D. Spirkoska, M. Frimmer, G. Abstreiter, and A. Fontcuberta i Morral, “Ga-assisted catalyst-free growth mechanism of GaAs nanowires by molecular beam epitaxy,” *Physical Review B*, vol. 77, p. 155326, 2008.
- [32] F. Jabeen, V. Grillo, S. Rubini, and F. Martelli, “Self-catalyzed growth of {GaAs} nanowires on cleaved Si by molecular beam epitaxy,” *Nanotechnology*, vol. 19, no. 27, p. 275711, 2008.
- [33] F. Glas, M. R. Ramdani, G. Patriarche, and J.-C. Harmand, “Predictive modeling of self-catalyzed III-V nanowire growth,” *Physical Review B*, vol. 88, p. 195304, 2013.
- [34] V. G. Dubrovskii, *Nucleation theory and growth of nanostructures*. Nanoscience and Technology, springer ed., 2014.
- [35] K. Hiruma, T. Katsuyama, K. Ogawa, M. Koguchi, H. Kakibayashi, and G. P. Morgan, “Quantum size microcrystals grown using organometallic vapor phase epitaxy,” *Applied Physics Letters*, vol. 59, no. 4, pp. 431–433, 1991.
- [36] T. Hamano, H. Hirayama, and Y. Aoyagi, “New technique for fabrication of two-dimensional photonic bandgap crystals by selective epitaxy,” *Japanese Journal of Applied Physics, Part 2: Letters*, vol. 36, no. 3 A, pp. 286–288, 1997.
- [37] H. Paetzelt, V. Gottschalch, J. Bauer, G. Benndorf, and G. Wagner, “Selective-area growth of GaAs and InAs nanowires-homo- and heteroepitaxy using SiNx templates,” *Journal of Crystal Growth*, vol. 310, no. 23, pp. 5093–5097, 2008.
- [38] J. Bauer, H. Paetzelt, V. Gottschalch, and G. Wagner, “GaAs nanowires grown by MOVPE,” *Physica Status Solidi (B) Basic Research*, vol. 247, no. 6, pp. 1294–1309, 2010.

- [39] K. Hiruma, M. Yazawa, T. Katsuyama, K. Ogawa, K. Haraguchi, M. Koguchi, and H. Kakibayashi, "Growth and optical properties of nanometer-scale GaAs and InAs whiskers," *Journal of Applied Physics*, vol. 77, no. 2, pp. 447–462, 1995.
- [40] P. Paiano, P. Prete, E. Speiser, N. Lovergine, W. Richter, L. Tapfer, and A. M. Mancini, "GaAs nanowires grown by Au-catalyst-assisted MOVPE using tertiarybutylarsine as group-V precursor," *Journal of Crystal Growth*, vol. 298, pp. 620–624, 2007.
- [41] S. Ermez, E. J. Jones, S. C. Crawford, and S. Gradečak, "Self-seeded growth of GaAs nanowires by metal-organic chemical vapor deposition," *Crystal Growth and Design*, vol. 15, no. 6, pp. 2768–2774, 2015.
- [42] E. Gil, Y. André, R. Cadoret, and A. Trassoudaine, "Hydride Vapor Phase Epitaxy for current III–V and nitride semiconductor compound issues," in *Handbook of Crystal Growth*, ch. 2, pp. 51–93, Elsevier, 2015.
- [43] R. Chau, S. Datta, M. Doczy, B. Doyle, B. Jin, J. Kavalieros, A. Majumdar, M. Metz, and M. Radosavljevic, "Benchmarking nanotechnology for high-performance and low-power logic transistor applications," *IEEE Transactions on Nanotechnology*, vol. 4, no. 2, p. 153, 2005.
- [44] K. Volz, W. Stolz, A. Dadgar, and A. Krost, *Growth of III/Vs on Silicon*, pp. 1249–1300. 2015.
- [45] M. Kaya and Y. Atici, "Studies of lattice mismatch and threading dislocations in GaAs/Si grown by MBE," *Superlattices and Microstructures*, vol. 35, no. 1-2, pp. 35–44, 2004.
- [46] Y. B. Bolkhovityanov and O. P. Pchelyakov, "GaAs epitaxy on Si substrates: modern status of research and engineering," *Physics -Uspekhi*, vol. 51, no. 5, pp. 473–456, 2008.
- [47] S. Breuer, F. Karouta, H. H. Tan, and C. Jagadish, "MOCVD growth of GaAs nanowires using Ga droplets," in *IEEE*, pp. 39–40, 2012.
- [48] Z. Dong, Y. André, V. G. Dubrovskii, C. Bougerol, C. Leroux, M. Ramdani, G. Monier, A. Trassoudaine, D. Castelluci, and E. Gil, "Self-catalyzed GaAs nanowires on silicon by hydride vapor phase epitaxy," *Nanotechnology*, vol. 28, no. 12, 2017.
- [49] M. Harrous, L. Chaput, A. Bendraoui, M. Cadoret, C. Pariset, and R. Cadoret, "Phosphine and arsine decomposition in CVD reactors for InP and InGaAs growth," *Journal of Crystal Growth*, vol. 92, no. 3-4, pp. 423–431, 1988.
- [50] E. Gil-Lafon, J. Napierala, A. Pimpinelli, R. Cadoret, A. Trassoudaine, and D. Castelluci, "Direct condensation modelling for a two-particle growth system: application to GaAs grown by hydride vapour phase epitaxy," *Journal of Crystal Growth*, vol. 258, no. 1-2, pp. 14–25, 2003.

- [51] A. Pimpinelli, R. Cadoret, E. Gil-Lafon, J. Napierala, and A. Trassoudaine, "Two-particle surface diffusion-reaction models of vapour-phase epitaxial growth on vicinal surfaces," *Journal of Crystal Growth*, vol. 258, no. 1, pp. 1–13, 2003.
- [52] G. B. Stringfellow, "Fundamental aspects of vapor growth and epitaxy," *Journal of Crystal Growth*, vol. 115, no. 1, pp. 1–11, 1991.
- [53] R. Cadoret and E. Gil-Lafon, "Mécanismes de croissance des faces 001 exactes et désorientées de GaAs par la méthode aux chlorures sous H<sub>2</sub> : diffusion superficielle, croissance par spirale, mécanismes de désorption HCl et GaCl<sub>3</sub>," *Journal de Physique I*, vol. 7, no. 7, pp. 889–907, 1997.
- [54] T. J. Wang, C. W. Tu, and F. K. Liu, "Integrated-optic surface-plasmon-resonance biosensor using gold nanoparticles by bipolarization detection," *IEEE Journal on Selected Topics in Quantum Electronics*, vol. 11, no. 2, pp. 493–499, 2005.
- [55] J. Richard, "Étude des propriétés optiques anormales de certains métaux pris en couches minces," *Journal de Physique*, vol. 25, no. 1-2, pp. 99–104, 1964.
- [56] J. G. Skofronick and W. B. Phillips, "Morphological changes in discontinuous gold films following deposition," *Journal of Applied Physics*, vol. 38, no. 12, pp. 4791–4796, 1967.
- [57] T. Liu, J. Tang, and L. Jiang, "The enhancement effect of gold nanoparticles as a surface modifier on DNA sensor sensitivity," *Biochemical and Biophysical Research Communications*, vol. 313, no. 1, pp. 3–7, 2004.
- [58] Y. T. Tseng, Y. J. Chuang, Y. C. Wu, C. S. Yang, M. C. Wang, and F. G. Tseng, "A gold-nanoparticle-enhanced immune sensor based on fiber optic interferometry," *Nanotechnology*, vol. 19, no. 34, 2008.
- [59] S. G. Ihn and J. I. Song, "InAs nanowires on Si substrates grown by solid source molecular beam epitaxy," *Nanotechnology*, vol. 18, no. 35, pp. 7–10, 2007.
- [60] S. Sharma, T. I. Kamins, and R. S. Williams, "Synthesis of thin silicon nanowires using gold-catalyzed chemical vapor deposition," *Applied Physics A: Materials Science and Processing*, vol. 80, no. 6, pp. 1225–1229, 2005.
- [61] M. Orvatinia and R. Imani, "Effect of catalyst layer on morphology and optical properties of zinc-oxide nanostructures fabricated by carbothermal evaporation method," *Micro & Nano Letters*, vol. 6, no. 8, p. 650, 2011.
- [62] R. Dowdy, D. A. Walko, S. A. Fortuna, and X. Li, "Realization of unidirectional planar GaAs," *IEEE Electron Device Letters*, vol. 33, no. 4, pp. 522–524, 2012.
- [63] I. Aharonovich, Y. Lifshitz, and S. Tamir, "Growth mechanisms of amorphous SiO<sub>x</sub> nanowires," *Applied Physics Letters*, vol. 90, no. 26, pp. 2005–2008, 2007.

- [64] Y. M. Shao, T. X. Nie, Z. M. Jiang, and J. Zou, "Behavior of Au-Si droplets in Si(001) at high temperatures," *Applied Physics Letters*, vol. 101, no. 5, pp. 2012–2015, 2012.
- [65] H. J. Joyce, Q. Gao, H. H. Tan, C. Jagadish, Y. Kim, M. A. Fickenscher, S. Perera, T. B. Hoang, L. M. Smith, H. E. Jackson, J. M. Yarrison-Rice, X. Zhang, and J. Zou, "Unexpected benefits of rapid growth rate for III-V nanowires," *Nano Letters*, vol. 9, no. 2, pp. 695–701, 2009.
- [66] K. Lekhal, G. Avit, Y. André, A. Trassoudaine, E. Gil, C. Varenne, C. Bougerol, G. Monier, and D. Castelluci, "Catalyst-assisted hydride vapor phase epitaxy of GaN nanowires: Exceptional length and constant rod-like shape capability," *Nanotechnology*, vol. 23, no. 40, 2012.
- [67] F. Ruffino, A. Canino, M. G. Grimaldi, F. Giannazzo, F. Roccaforte, and V. Raineri, "Kinetic mechanism of the thermal-induced self-organization of Au/Si nanodroplets on Si(100): Size and roughness evolution," *Journal of Applied Physics*, vol. 104, no. 2, 2008.
- [68] F. Ruffino and M. G. Grimaldi, "Atomic force microscopy study of the growth mechanisms of nanostructured sputtered Au film on Si(111): Evolution with film thickness and annealing time," *Journal of Applied Physics*, vol. 107, no. 10, 2010.
- [69] E. Jiran and C. V. Thompson, "Capillary instabilities in thin films," *Journal of Electronic Materials*, vol. 19, no. 11, pp. 1153–1160, 1990.
- [70] M. A. Mahjoub, G. Monier, C. Robert-Goumet, L. Bideux, and B. Gruzza, "XPS combined with MM-EPES technique for in situ study of ultra thin film deposition: Application to an Au/SiO<sub>2</sub>/Si structure," *Applied Surface Science*, vol. 357, pp. 1268–1273, 2015.
- [71] G. Le Lay and J. P. Faurie, "AES study of the very first stages of condensation of gold films on silicon (111) surfaces," *Surface Science*, vol. 69, no. 1, pp. 295–300, 1977.
- [72] J. R. Levine, J. B. Cohen, and Y. W. Chung, "Thin film island growth kinetics: a grazing incidence small angle X-ray scattering study of gold on glass," *Surface Science*, vol. 248, no. 1-2, pp. 215–224, 1991.
- [73] Z. Shi, S. Shao, and Y. Wang, "Improved the surface roughness of silicon nanophotonic devices by thermal oxidation method," *Journal of Physics: Conference Series*, vol. 276, no. 1, 2011.
- [74] O. Stein, J. Ankri, and M. Asscher, "Surface diffusion of gold nanoclusters on Ru(0001): Effects of cluster size, surface defects and adsorbed oxygen atoms," *Physical Chemistry Chemical Physics*, vol. 15, no. 32, pp. 13506–13512, 2013.
- [75] G. Le Lay, G. Quentel, J. P. Faurie, and A. Masson, "Epitaxy of noble metals and (111) surface superstructures of silicon and germanium part I: Study at room temperature," *Thin solid films*, vol. 35, pp. 273–287, 1976.
- [76] F. A. Otter, H. C. Abbink, and O. L. De Lange, "Possibility of a surface-stabilized compound of Au and Si on surfaces," *Surface Science*, vol. 27, pp. 273–278, 1971.

- [77] G. Le Lay, G. Quentel, J. P. Faurie, and A. Masson, "Epitaxy of noble metals and (111) surface superstructures of silicon and germanium part II: Study After Annealing," *Thin solid films*, vol. 35, pp. 289–303, 1976.
- [78] F. W. Smith and G. Ghidini, "Reaction of Oxygen with Si(111) and (100): Critical Conditions for the Growth of SiO<sub>2</sub>," *J. Electrochem. Soc.*, vol. 129, no. 6, pp. 1300–1306, 1982.
- [79] H. Dallaporta, M. Liehr, and J. E. Lewis, "Silicon dioxide defects induced by metal impurities," *Physical Review B*, vol. 41, no. 8, pp. 5075–5083, 1990.
- [80] A. Rath, J. K. Dash, R. R. Juluri, A. Rosenauer, M. Schoewalter, and P. V. Satyam, "Growth of oriented Au nanostructures : Role of oxide at the interface," *Journal of Applied Physics*, vol. 111, p. 064322, 2012.
- [81] A. Hiraki, E. Lugujo, and J. W. Mayer, "Formation of silicon oxide over gold layers on silicon substrates," *Journal of Applied Physics*, vol. 43, p. 3643, 1972.
- [82] F. Cheynis, F. Leroy, A. Ranguis, B. Demailleur, P. Bindzi, C. Veit, W. Bon, and P. Müller, "Combining low-energy electron microscopy and scanning probe microscopy techniques for surface science: Development of a novel sample-holder," *Review of Scientific Instruments*, vol. 85, no. 4, 2014.
- [83] V. G. Dubrovskii, "Refinement of nucleation theory for vapor–liquid–solid nanowires," *Crystal Growth & Design*, vol. 17, pp. 2589–2593, may 2017.
- [84] S. Breuer, M. Hilse, A. Trampert, L. Geelhaar, and H. Riechert, "Vapor-liquid-solid nucleation of GaAs on Si(111): Growth evolution from traces to nanowires," *Physical Review B*, vol. 82, p. 75406, aug 2010.
- [85] Y. André, K. Lekhal, P. Hoggan, G. Avit, F. Cadiz, A. Rowe, D. Paget, C. Leroux, A. Trassoudaine, M. R. Ramdani, G. Monier, D. Colas, R. Ajib, D. Castelluci, and E. Gil, "Vapor Liquid Solid-Hydride vapor phase epitaxy (VLS-HVPE) Growth of Ultra-Long Defect-Free GaAs Nanowires: Ab initio Simulations Supporting Center Nucleation," *The Journal of Chemical Physics*, vol. 140, p. 194706, 2014.
- [86] A. Ali, Y. Chen, V. Vasiraju, and S. Vaddiraju, "Nanowire-based thermoelectrics," *Nanotechnology*, vol. 28, p. 282001, 2017.
- [87] F. Leroy, T. Passanante, F. Cheynis, S. Curiotto, E. B. Bussmann, and P. Müller, "Catalytically enhanced thermal decomposition of chemically grown silicon oxide layers on Si(001)," *Applied Physics Letters*, vol. 108, p. 111601, 2016.
- [88] F. Matteini, V. G. Dubrovskii, D. Ruffer, Y. Fontana, and A. Fontcuberta i Morral, "Tailoring the diameter and density of self-catalyzed GaAs nanowires on silicon," *Nanotechnology*, vol. 26, p. 105603, 2015.

- [89] V. G. Dubrovskii, T. Xu, S. R. Plissard, F. Glas, and B. Grandidier, “Self-equilibration of the diameter of Ga-catalyzed GaAs nanowires,” *Nano Letters*, vol. 15, pp. 5580–5584, 2015.
- [90] K. Wonjong, V. G. Dubrovskii, J. Vukajlovic-plestina, L. Francaviglia, L. Gu, H. Potts, M. Friedl, J. Leran, and A. Fontcuberta i Morral, “Bistability of contact angle and its role in achieving quantum-thin self-assisted GaAs nanowires,” *Nano Letters*, vol. 18, pp. 49–57, 2018.
- [91] T. Tauchnitz, T. Nurmamyrov, R. Hu, M. Engler, S. Facsko, H. Schneider, M. Helm, and E. Dimakis, “Decoupling the two roles of Ga droplets in the self-catalyzed growth of GaAs nanowires on SiO<sub>x</sub>/Si(111) substrates,” *Crystal Growth & Design*, vol. 17, pp. 5276–5282, 2017.
- [92] J. Dufouleur, C. Colombo, T. Garma, B. Ketterer, E. Uccelli, M. Nicotra, and A. Fontcuberta i Morral, “P-Doping mechanisms in catalyst-free gallium arsenide nanowires,” *Nano Letters*, vol. 10, no. 5, pp. 1734–1740, 2010.
- [93] F. Glas, “Chemical potentials for Au-assisted vapor-liquid-solid growth of III-V Nanowires,” *Journal of Applied Physics*, vol. 108, p. 073506, 2010.
- [94] V. G. Dubrovskii, “Refinement of nucleation theory for vapor-liquid-solid nanowires,” *Crystal Growth & Design*, vol. 17, pp. 2589–2593, 2017.
- [95] V. G. Dubrovskii, A. A. Koryakin, and N. V. Sibirev, “Understanding the composition of ternary III-V nanowires and axial nanowire heterostructures in nucleation-limited regime,” *Materials & Design*, vol. 132, pp. 400–408, 2017.
- [96] E. D. Leshchenko, M. Ghasemi, V. G. Dubrovskii, and J. Johansson, “Nucleation-limited composition of ternary III–V nanowires forming from quaternary gold based liquid alloys,” *CrystEngComm*, vol. 20, pp. 1649–1655, 2018.
- [97] A. Mostafa and M. Medraj, “Binary phase diagrams and thermodynamic properties of silicon and essential doping elements,” *Materials*, vol. 10, p. 676, 2017.
- [98] D. T. J. Hurle, “A comprehensive thermodynamic analysis of native point defect and dopant solubilities in gallium arsenide,” *Journal of Applied Physics*, vol. 85, no. 10, pp. 6957–7022, 1999.
- [99] P. Chevalier, “A Thermodynamic Evaluation of the Au-Ge and Au-Si Systems,” *Thermochimica Acta*, vol. 141, pp. 217–226, 1989.
- [100] G. B. Stringfellow, “Calculation of ternary phase diagrams for III-V systems,” *Journal of Physics and Chemistry of Solids*, vol. 33, pp. 665–677, 1972.

- [101] V. G. Dubrovskii and J. Grecenkov, “Zeldovich nucleation rate, self-consistency renormalization, and crystal phase of Au-catalyzed GaAs nanowires,” *Crystal Growth & Design*, vol. 15, pp. 340–347, 2015.
- [102] V. G. Dubrovskii, *Theory of VLS growth of compound semiconductors*, vol. 93. Elsevier Inc., 1 ed., 2015.
- [103] H. Okamoto and B. Massalski, “The Au-Si (gold-silicon) system,” *Calphad*, vol. 4, no. 2, pp. 190–198, 1983.
- [104] R. W. Olesinski, N. Kanani, and G. J. Abbaschian, “The Ga-Si (gallium-silicon) system,” *Bulletin of Alloy Phase Diagrams*, vol. 6, no. 4, pp. 362–364, 1985.
- [105] V. G. Dubrovskii, “Mono- and polynucleation, atomistic growth, and crystal phase of III-V nanowires under varying group V flow,” *The Journal of Chemical Physics*, vol. 142, p. 204702, 2015.
- [106] A. Dadgar, M. Poschenrieder, J. Bläsing, O. Contreras, F. Bertram, T. Riemann, A. Reiher, M. Kunze, I. Daumiller, A. Krtuschil, A. Diez, A. Kaluza, A. Modlich, M. Kamp, J. Christen, F. Ponce, E. Kohn, and A. Krost, “MOVPE growth of GaN on Si(111) substrates,” *Journal of Crystal Growth*, vol. 248, pp. 556–562, 2003.
- [107] K. Werner, A. Beyer, J. O. Oelerich, S. D. Baranovskii, W. Stolz, and K. Volz, “Structural characteristics of gallium metal deposited on Si (001) by MOCVD,” *Journal of Crystal Growth*, vol. 405, pp. 102–109, 2014.
- [108] V. Khorenko, I. Regolin, S. Neumann, W. Prost, F. Tegude, H. Wiggers, V. Khorenko, I. Regolin, S. Neumann, W. Prost, and F. Tegude, “Photoluminescence of GaAs nanowhiskers grown on Si substrate,” *Applied Physics Letters*, vol. 85, no. 2004, pp. 6047–6048, 2004.
- [109] L. C. Chuang, M. Moewe, C. Chase, N. P. Kobayashi, C. Chang-hasnain, L. C. Chuang, M. Moewe, C. Chase, and S. Crankshaw, “Critical diameter for III-V nanowires grown on lattice-mismatched substrates,” *Applied Physics Letters*, vol. 90, p. 043115, 2007.
- [110] E. Dimakis, U. Jahn, M. Ramsteiner, A. Tahraoui, J. Grandal, X. Kong, O. Marquardt, A. Trampert, H. Riechert, and L. Geelhaar, “Coaxial multishell (In, Ga)As / GaAs nanowires for near-infrared emission on Si substrates,” *Nano Letters*, vol. 14, pp. 2604–2609, 2014.
- [111] M. D. Thompson, A. Alhodaib, A. P. Craig, A. Robson, A. Aziz, A. Krier, J. Svensson, L. E. Wernersson, A. M. Sanchez, and A. R. J. Marshall, “Low leakage-current InAsSb nanowire photodetectors on silicon,” *Nano Letters*, vol. 16, no. 1, pp. 182–187, 2016.
- [112] S. A. Dayeh, R. Chen, Y. G. Ro, and J. Sim, “Progress in doping semiconductor nanowires during growth,” *Materials Science in Semiconductor Processing*, vol. 62, no. May, pp. 135–155, 2017.

- [113] E. F. Schubert, *Doping in III–V Semiconductors*. Cambridge University Press, 1993.
- [114] C. Y. Wang, Y. C. Hong, Z. J. Ko, Y. W. Su, and J. H. Huang, “Electrical and optical properties of Au-catalyzed GaAs nanowires grown on Si (111) substrate by molecular beam epitaxy,” *Nanoscale Research Letters*, vol. 12, p. 290, 2017.
- [115] M. Piccin, G. Bais, V. Grillo, F. Jabeen, S. De Franceschi, E. Carlino, M. Lazzarino, F. Romanato, L. Businaro, S. Rubini, F. Martelli, and A. Franciosi, “Growth by molecular beam epitaxy and electrical characterization of GaAs nanowires,” *Physica E: Low-Dimensional Systems and Nanostructures*, vol. 37, no. 1-2, pp. 134–137, 2007.
- [116] M. Hilse, M. Ramsteiner, S. Breuer, L. Geelhaar, and H. Riechert, “Incorporation of the dopants Si and Be into GaAs nanowires,” *Applied Physics Letters*, vol. 96, no. 19, pp. 1–4, 2010.
- [117] B. Ketterer, E. Mikheev, E. Uccelli, and A. Fontcuberta i Morral, “Compensation mechanism in silicon-doped gallium arsenide nanowires,” *Applied Physics Letters*, vol. 97, p. 223103, 2010.
- [118] C. Gutsche, A. Lysov, I. Regolin, K. Blekker, W. Prost, and F. Tegude, “n-Type doping of vapor-liquid-solid grown GaAs nanowires,” *Nanoscale Research Letters*, vol. 6, pp. 1–6, 2011.
- [119] R. Sun, D. Jacobsson, I. J. Chen, M. Nilsson, C. Thelander, S. Lehmann, and K. A. Dick, “Sn-seeded GaAs nanowires as self-assembled radial p-n junctions,” *Nano Letters*, vol. 15, no. 6, pp. 3757–3762, 2015.
- [120] S. Suomalainen, T. V. Hakkarainen, T. Salminen, R. Koskinen, M. Honkanen, E. Luna, and M. Guina, “Te-doping of self-catalyzed GaAs nanowires,” *Applied Physics Letters*, vol. 107, no. 1, pp. 1–5, 2015.
- [121] N. I. Goktas, E. M. Fiordaliso, and R. R. Lapierre, “Doping assessment in GaAs nanowires,” *Nanotechnology*, vol. 29, no. 23, p. 234001, 2018.
- [122] M. Orrù, E. Repiso, S. Carapezzi, A. Henning, S. Roddaro, A. Franciosi, Y. Rosenwaks, A. Cavallini, F. Martelli, and S. Rubini, “A roadmap for controlled and efficient n-Type doping of self-assisted GaAs nanowires grown by molecular beam epitaxy,” *Advanced Functional Materials*, vol. 26, no. 17, pp. 2836–2845, 2016.
- [123] S. Arab, M. Yao, C. Zhou, P. D. Daniel, and S. B. Cronin, “Doping concentration dependence of the photoluminescence spectra of n-type GaAs nanowires,” *Applied Physics Letters*, vol. 108, p. 182106, 2016.
- [124] W. Seifert, M. Borgstro, K. Deppert, K. A. Dick, J. Johansson, M. W. Larsson, T. Martensson, N. Skold, C. P. T. Svensson, B. A. Wacaser, L. R. Wallenberg, and L. Samuelson, “Growth of one-dimensional nanostructures in MOVPE,” *Journal of Crystal Growth*, vol. 272, pp. 211–220, 2004.

- [125] S. J. Moss and A. Ledwith, "The chemistry of the semiconductor industry," *Chapman and Hall*, 1997.
- [126] F. Fischer, D. Schuh, M. Bichler, G. Abstreiter, M. Grayson, and K. Neumaier, "Modulating the growth conditions: Si as an acceptor in (110) GaAs for high mobility p-type heterostructures," *Applied Physics Letters*, vol. 86, no. 19, pp. 1–3, 2005.
- [127] N. Ghaderi, M. Peressi, N. Binggeli, and H. Akbarzadeh, "Structural properties and energetics of intrinsic and Si-doped GaAs nanowires: First-principles pseudopotential calculations," *Physical Review B - Condensed Matter and Materials Physics*, vol. 81, no. 155311, pp. 1–9, 2010.
- [128] F. Glas, "Comparison of modeling strategies for the growth of heterostructures in III-V nanowires," *Crystal Growth and Design*, vol. 17, no. 9, pp. 4785–4794, 2017.
- [129] N. Hannay, "Solid-state chemistry," 1976.
- [130] J. Murota, E. Arai, and K. Kudo, "Arsenic doping of chemical vapor deposited polycrystalline silicon using SiH<sub>4</sub>-H-AsH<sub>3</sub> gas system," *J. Electrochem. Soc.: Solid-State Science and Technology*, vol. 31, pp. 1188–1192, 1980.
- [131] J. Ushio, K. Nakagawa, M. Miyao, and T. Maruizumi, "Surface Segregation Behavior of B, Ga, and Sb during Si MBE : Calculations using a First-Principles Method," *Physical Review B*, vol. 58, no. 7, pp. 3932–3936, 1998.
- [132] J. P. Perdew, K. Burke, and M. Ernzerhof, "Generalized gradient approximation made simple," *Physical Review Letters*, vol. 77, no. 18, pp. 3865–3868, 1996.
- [133] K. Doblhoff-Dier, J. Meyer, P. E. Hoggan, and G. J. Kroes, "Quantum monte carlo calculations on a benchmark molecule-metal surface reaction: H<sub>2</sub> + Cu(111)," *Journal of Chemical Theory and Computation*, vol. 13, no. 7, pp. 3208–3219, 2017.
- [134] A. Y. Cho and J. R. Arthur, "Molecular Beam Epitaxy," *Progress in Solid State Chemistry*, vol. 10, pp. 157–191, 1980.
- [135] J. De-Sheng, Y. Makita, K. Ploog, and H. J. Queisser, "Electrical properties of doped GaAs nanowire grown by molecular beam epitaxy," *Journal of Applied Physics*, vol. 53, no. 999, p. 1982, 1982.
- [136] G. Borghs, K. Bhattacharyya, K. Deneffe, P. Vanmieghem, and R. Mertens, "Band-gap narrowing in highly doped n- and p-type GaAs studied by photoluminescence spectroscopy," *Journal of Applied Physics*, vol. 66, p. 4381, 1989.
- [137] E. Burstein, "Anomalous Optical Absorption Limit in InSb," *Physical Review*, vol. 93, pp. 632–633, feb 1954.

- [138] T. S. Moss, “The interpretation of the properties of indium antimonide,” *Proceedings of the Physical Society B*, vol. 67, pp. 775–782, 1954.
- [139] N. Y. Lee, K. J. Lee, C. Lee, J. E. Kim, H. Y. Park, D. H. Kwak, H. C. Lee, and H. Lim, “Determination of conduction band tail and Fermi energy of heavily Si-doped GaAs by room-temperature photoluminescence,” *Journal of Applied Physics*, vol. 78, no. 5, pp. 3367–3370, 1995.
- [140] J. Johansson and M. Ghasemi, “Kinetically limited composition of ternary III-V nanowires,” *Physical Review Materials*, vol. 1, no. 040401, pp. 1–5, 2017.
- [141] V. G. Dubrovskii, “Fully analytical description for the composition of ternary vapor-liquid-solid nanowires,” *Crystal Growth and Design*, vol. 15, no. 12, pp. 5738–5743, 2015.
- [142] V. G. Dubrovskii, “Understanding the vapor-liquid-solid growth and composition of ternary III-V nanowires and nanowire heterostructures,” *Journal of Physics D*, vol. 50, no. 45, 2017.
- [143] M. I. Dyakonov and V. I. Perel, “Current induced spin orientation of electrons in semiconductors,” *Physics Letters*, vol. 35A, no. 6, pp. 459–460, 1971.
- [144] F. Dirnberger, M. Kammermeier, J. König, M. Forsch, P. Junior, T. Campos, J. Fabian, J. Schliemann, C. Schüller, T. Korn, P. Wenk, and D. Bougeard, “Ultralong spin lifetimes in one-dimensional semiconductor nanowires,” *Applied Physics Letters*, vol. 114, p. 202101, 2019.
- [145] F. Cadiz, P. Barate, D. Paget, D. Grebenkov, J. P. Korb, A. C. H. Rowe, T. Amand, S. Arscott, and E. Peytavit, “All optical method for investigation of spin and charge transport in semiconductors : Combination of spatially and time-resolved luminescence,” *Journal of Applied Physics*, vol. 116, p. 023711, 2014.
- [146] R. A. Smith, *Semiconductors*. Cambridge University Press, Cambridge, 1978.
- [147] F. Cadiz, D. Paget, A. C. H. Rowe, and S. Arscott, “Ambipolar spin-spin coupling in p+ GaAs,” *Physical Review B*, vol. 92, p. 121203(R), 2015.
- [148] J. Lu, M. J. R. Hoch, P. L. Kuhns, W. G. Moulton, Z. Gan, and A. P. Reyes, “Nuclear spin-lattice relaxation in n-type insulating and metallic GaAs single crystals,” *Physical Review B*, vol. 74, no. 12, p. 125208, 2006.
- [149] J. M. Kikkawa and D. D. Awschalom, “Lateral drag of spin coherence in gallium arsenide,” *Letters to nature*, vol. 1893, no. October 1998, pp. 1998–2000, 1999.
- [150] T. Henn, T. Kiessling, W. Ossau, L. W. Molenkamp, K. Biermann, P. V. Santos, T. Henn, T. Kiessling, W. Ossau, L. W. Molenkamp, K. Biermann, and P. V. Santos, “Ultrafast supercontinuum fiber-laser based pump-probe scanning magneto-optical Kerr effect microscope for the investigation of electron spin dynamics in semiconductors at cryogenic temperatures with

- picosecond time and micrometer spatial resolution,” *Review of Scientific Instruments*, vol. 84, p. 123903, 2013.
- [151] A. R. Cameron, P. Riblet, and A. Miller, “Spin gratings and the measurement of electron drift mobility in multiple quantum well memiconductors,” *Physical Review Letters*, vol. 76, no. 25, pp. 4793–4796, 1996.
- [152] G. Wang, B. L. Liu, A. Balocchi, P. Renucci, C. R. Zhu, T. Amand, C. Fontaine, and X. Marie, “Gate control of the electron spin-diffusion length in semiconductor quantum wells,” *Nature Communications*, vol. 4, pp. 1–5, 2013.
- [153] C. Gutsche, R. Niepelt, M. Gnauk, A. Lysov, W. Prost, C. Ronning, and F. Tegude, “Direct determination of minority carrier diffusion lengths at axial GaAs nanowire p-n junctions,” *Nano Letters*, vol. 12, pp. 1453–1458, 2012.
- [154] G. Gilliland and M. Petrovic, “Time-dependent heterointerfacial band bending and quasi-two-dimensional excitonic transport in GaAs structures,” *Physical Review B - Condensed Matter and Materials Physics*, vol. 58, no. 8, pp. 4728–4732, 1998.
- [155] D. Paget, F. Cadiz, A. C. H. Rowe, F. Moreau, S. Arscott, and E. Peytavit, “Imaging ambipolar diffusion of photocarriers in GaAs thin films,” *Journal of Applied Physics*, vol. 111, p. 123720, 2012.
- [156] H. Ohno, “Making nonmagnetic semiconductors ferromagnetic,” *Science*, vol. 281, no. 5379, pp. 951–956, 1998.
- [157] S. Bieker, T. Henn, T. Kiessling, W. Ossau, and L. W. Molenkamp, “Spatially resolved thermodynamics of the partially ionized exciton gas in GaAs,” *Physical Review Letters*, vol. 114, no. 22, pp. 1–5, 2015.
- [158] Y. Nagamune, H. Watabe, F. Sogawa, Y. Arakawa, Y. Nagamune, H. Watabe, F. Sogawa, and Y. Arakawa, “Onedimensional exciton diffusion in GaAs quantum wires,” *Appl. Phys. Lett.*, vol. 67, no. 11, pp. 1535–1537, 1995.
- [159] J. Bolinsson, K. Mergenthaler, L. Samuelson, and A. Gustafsson, “Diffusion length measurements in axial and radial heterostructured nanowires using cathodoluminescence,” *Journal of Crystal Growth*, vol. 315, no. 1, pp. 138–142, 2011.
- [160] A. Darbandi, S. P. Watkins, and S. P. Watkins, “Measurement of minority carrier diffusion lengths in GaAs nanowires by a nanoprobe technique,” *Journal of Applied Physics*, vol. 120, p. 014301, 2016.
- [161] A. Gustafsson, J. Bolinsson, N. Sköld, and L. Samuelson, “Determination of diffusion lengths in nanowires using cathodoluminescence,” *Applied Physics Letters*, vol. 97, p. 072114, 2010.

- [162] D. Spirkoska, J. Arbiol, A. Gustafsson, S. Conesa-Boj, F. Glas, I. Zardo, M. Heigoldt, M. H. Gass, A. L. Bleloch, S. Estrade, M. Kaniber, J. Rossler, F. Peiro, J. R. Morante, G. Abstreiter, L. Samuelson, and A. Fontcuberta i Morral, “Structural and optical properties of high quality zinc-blende/wurtzite GaAs nanowire heterostructures,” *Physical Review B*, vol. 80, p. 245325, 2009.
- [163] G. Lampel, “Nuclear dynamic polarization by optical electronic saturation and optical pumping in semiconductors,” *Physical Review Letters*, vol. 20, p. 491, 1968.
- [164] I. Favorskiy, D. Vu, E. Peytavit, S. Arscott, D. Paget, and A. C. H. Rowe, “Circularly polarized luminescence microscopy for the imaging of charge and spin diffusion in semiconductors,” *Review of Scientific Instruments*, vol. 81, p. 103902, 2010.
- [165] S. Fang, R. Zhu, and T. Lai, “Spin relaxation dynamics of holes in intrinsic GaAs quantum wells studied by transient circular dichromatic absorption spectroscopy at room temperature,” *Scientific Reports*, vol. 7, no. 287, pp. 1–7, 2017.
- [166] L. H. Teng, P. Zhang, T. S. Lai, and M. W. Wu, “Density dependence of spin relaxation in GaAs quantum well at room temperature,” *EPL (Europhysics letters)*, vol. 84, no. 2, pp. 1–4, 2018.
- [167] D. Vu, S. Arscott, R. Ramdani, E. Gil, Y. André, S. Bansropun, B. Gérard, A. C. H. Rowe, and D. Paget, “Photoassisted tunneling from free-standing GaAs thin films into metallic surfaces,” *Physical Review B*, vol. 82, p. 115331, 2010.
- [168] S. Park, D. Paget, V. L. Berkovits, V. P. Ulin, P. A. Alekseev, N. A. Kaliuzhnyi, S. A. Mintairov, and F. Cadiz, “Photovoltage-induced blockade of charge and spin diffusion in semiconducting thin films,” *Journal of Applied Physics*, vol. 126, 2019.
- [169] O. Demichel, M. Heiss, J. Bleuze, H. Mariette, and A. Fontcuberta i Morral, “Impact of surfaces on the optical properties of GaAs nanowires,” *Applied Physics Letters*, vol. 97, p. 201907, 2010.
- [170] M. Heiss, C. Colombo, and A. Fontcuberta i Morral, “Nanowire based heterostructures: fundamental properties and applications,” *Nanoepitaxy: Materials and Devices III*, vol. 8106, p. 810603, 2011.
- [171] J. C. Shin, K. H. Kim, K. J. Yu, H. Hu, L. Yin, C. Z. Ning, J. A. Rogers, J. M. Zuo, and X. Li, “In<sub>x</sub>Ga<sub>1-x</sub> as nanowires on silicon: One-dimensional heterogeneous epitaxy, bandgap engineering, and photovoltaics,” *Nano Letters*, vol. 11, no. 11, pp. 4831–4838, 2011.
- [172] J. C. Shin, A. Lee, M. P. Katal, D. Y. Kim, L. Yu, J. H. Kim, H. J. Kim, W. J. Choi, D. Wasserman, K. J. Choi, and X. Li, “Wafer-scale production of uniform InAs<sub>y</sub>P<sub>1-y</sub> nanowire array on silicon for heterogeneous integration,” *ACS Nano*, vol. 7, no. 6, pp. 5463–5471, 2013.

- [173] J. W. Hwang, B. K. Kim, S. J. Lee, M. H. Bae, and J. C. Shin, “Catalyst-free heteroepitaxial growth of very long InAs nanowires on Si,” *Current Applied Physics*, vol. 15, pp. S35–S39, 2015.
- [174] J. Shah, R. F. Leheny, and W. Wiegmann, “Low-temperature absorption spectrum in GaAs in the presence of optical pumping,” *Physical Review B*, vol. 16, no. 4, pp. 1577–1580, 1977.
- [175] M. Benzaquen, D. Walsh, and K. Mazuruk, “Conductivity of n-type GaAs near the Mott transition,” *Physical Review B*, vol. 36, no. 9, pp. 4748–4753, 1987.
- [176] A. L. Efros, Y. S. Halpren, and B. I. Shklovskii, “Low temperature conductivity of strongly compensated semiconductors,” in *Proceedings of the International Conference on Physics of semiconductors*, (Warsaw), Polish Scientific publishers, Warsaw, 1972.
- [177] B. I. Shklovskii and A. L. Efros, *Electronic properties of doped semiconductors*. Moscow: Nauka, 1984.
- [178] R. I. Dzhiyev, K. V. Kavokin, V. L. Korenev, M. V. Lazarev, B. Y. Meltser, M. N. Stepanova, B. P. Zakharchenya, D. Gammon, and D. S. Katzer, “Low temperature spin relaxation in n-type GaAs,” *Physical Review B*, vol. 66, p. 245204, 2002.
- [179] B. J. Skromme and G. E. Stillman, “Excited-state-donor-to-acceptor transitions in the photoluminescence spectrum of GaAs and InP,” *Physical Review B*, vol. 29, no. 4, pp. 1982–1992, 1984.
- [180] D. W. Kisker, H. Tews, and W. Rehm, “Luminescence study of C, Zn, Si, and Ge acceptors in GaAs,” *Journal of Applied Physics*, vol. 54, no. 3, pp. 1332–1336, 1983.
- [181] G. L. Bir, A. G. Aronov, and G. E. Pikus, “Spin relaxation of electrons due to scattering by holes,” *Sov. Phys. JETP*, vol. 42, no. 4, pp. 705–712, 1975.
- [182] V. L. Berkovits, D. Paget, A. N. Karpenko, V. P. Ulin, and O. E. Tereshchenko, “Soft nitridation of GaAs(100) by hydrazine sulfide solutions: Effect on surface recombination and surface barrier,” *Applied Physics Letters*, vol. 90, no. 2, p. 22104, 2007.
- [183] V. L. Berkovits, V. P. Ulin, M. Losurdo, P. Capezzuto, G. Bruno, G. Perna, and V. Capozzi, “Wet chemical nitridation of GaAs (100) by hydrazine solution for surface passivation,” *Applied Physics Letters*, vol. 80, no. 20, pp. 3739–3741, 2002.
- [184] V. L. Berkovits, V. P. Ulin, O. E. Tereshchenko, D. Paget, A. C. H. Rowe, P. Chiaradia, B. P. Doyle, and S. Nannarone, “GaAs(111) A and B surfaces in hydrazine sulfide solutions: Extreme polarity dependence of surface adsorption processes,” *Phys. Rev. B*, vol. 80, p. 233303, dec 2009.

- [185] V. L. Berkovits, L. Masson, I. V. Makarenko, and V. P. Ulin, “Structural properties of GaAs surfaces nitrated in hydrazine-sulfide solutions,” *Applied Surface Science*, vol. 254, no. 24, pp. 8023–8028, 2008.
- [186] P. A. Alekseev, M. S. Dunaevskiy, V. P. Ulin, T. V. Lvova, D. O. Filatov, A. V. Nezhdanov, A. I. Mashin, and V. L. Berkovits, “Nitride Surface Passivation of GaAs Nanowires: Impact on Surface State Density,” *Nano Letters*, vol. 15, pp. 63–68, 2014.
- [187] V. Badescu and P. T. Landsberg, “Theory of some effects of photon recycling in semiconductors,” *Semiconductor Science and Technology*, vol. 8, no. 7, pp. 1267–1276, 1993.
- [188] O. Tereshchenko, S. I. Chikichev, and A. Terekhov, “Atomic structure and electronic properties of HCl–isopropanol treated and vacuum annealed GaAs(100) surface,” *Applied Surface Science*, vol. 142, pp. 75–80, 1999.
- [189] C. Weisbuch, R. C. Miller, R. Dingle, A. C. Gossarg, and W. Wiegmann, “Intrinsic Radiative Recombination from Quantum States in GaAsAl<sub>x</sub> Ga<sub>1-x</sub> As Multi-Quantum Well Structures,” *Solid State Communications*, vol. 373, pp. 219–222, 1981.
- [190] H. Böttger and V. V. Bryksin, “Hopping conductivity in ordered and disordered solids (II),” *Physica Status Solidi (b)*, vol. 78, no. 2, pp. 415–451, 1976.
- [191] B. G. Arnaudov, D. S. Domanevskii, and I. Y. Yanchev, “Hopping conductivity in heavily doped strongly compensated GaAs,” *Physica Status Solidi (b)*, vol. 91, no. 1, pp. 311–318, 1979.
- [192] D. Lemoine, C. Pelletier, S. Rolland, and R. Granger, “Hopping conduction in epitaxial n-GaAs layers,” *Physics Letters A*, vol. 56, no. 6, pp. 493–495, 1976.
- [193] D. Bimberg, H. Munzel, A. Steckenborn, and J. Christen, “Kinetics of relaxation and recombination of nonequilibrium carriers in GaAs : carrier capture by impurities,” *Phys. Rev. B*, vol. 31, p. 7788, 1985.
- [194] Y. Qi, Z. G. Yu, and M. E. Flatté, “Spin gunn effect,” *Physical Review Letters*, vol. 96, p. 26602, 2006.
- [195] T. Paul, P. Leboeuf, N. Pavloff, K. Richter, and P. Schlagheck, “Nonlinear transport of Bose-Einstein condensates through waveguides with disorder,” *Physical Review A - Atomic, Molecular, and Optical Physics*, vol. 72, no. 6, pp. 1–14, 2005.
- [196] B. Santos, L. P. Viana, M. L. Lyra, and F. A. de Moura, “Diffusive, super-diffusive and ballistic transport in the long-range correlated 1D Anderson model,” *Solid State Communications*, vol. 138, no. 12, pp. 585–589, 2006.

- 
- [197] D. N. Arnold, G. David, D. Jerison, S. Mayboroda, and M. Filoche, “Effective Confining Potential of Quantum States in Disordered Media,” *Physical Review Letters*, vol. 116, no. 5, 2016.
- [198] H. Mehdi, G. Monier, P. E. Hoggan, L. Bideux, C. Robert-Goumet, and V. G. Dubrovskii, “Combined angle-resolved X-ray photoelectron spectroscopy, density functional theory and kinetic study of nitridation of gallium arsenide,” *Applied Surface Science*, vol. 427, pp. 662–669, 2017.
- [199] C. Stampfl and C. G. de Walle, “Density-functional calculations for III-V nitrides using the local-density approximation and the generalized gradient approximation,” *Physical Review B*, vol. 59, no. 8, pp. 5521–5535, 1999.
- [200] M. Fuchs, J. Da Silva, C. Stampfl, and M. Scheffler, “Cohesive properties of group-III nitrides: A comparative study of all-electron and pseudopotential calculations using the generalized gradient approximation,” *Physical Review B*, vol. 65, no. 24, pp. 245212–1 – 245212–13, 2002.
- [201] D. B. Wittry and D. F. Kyser, “Measurement of diffusion lengths in direct-gap semiconductors by electron-beam excitation,” *Journal of Applied Physics*, vol. 38, no. 1, pp. 375–382, 1967.